Error estimates for ab initio predictions of surface energy and work function

Sam De Waele

Supervisors: Prof. dr. Stefaan Cottenier, Prof. dr. ir. Veronique Van Speybroeck
Counsellors: Dr. ir. Kurt Lejaeghere, Ir. Michael Sluydts

Master's dissertation submitted in order to obtain the academic degree of
Master of Science in Engineering Physics

Department of Materials Science and Engineering
Chairman: Prof. dr. ir. Joris Degrieck

Department of Applied Physics
Chairman: Prof. dr. ir. Christophe Leys

Faculty of Engineering and Architecture
Academic year 2014-2015

UNIVERSITEIT
GENT

This research was conducted at the Center for Molecular Modeling.

Preface

Like a lot of engineering students who opt for engineering physics, I was ever captivated by the beauty of describing a physical problem from simple and concise theoretical principles. There is no greater joy than being able to understand and explain natural phenomena with a general quantitative model. As course texts flowed by and knowledge deepened, interests became more specific. It was during the elective course of Professor Stefaan Cottenier when I first became acquainted with ab initio modeling and Density-functional theory. Being almost instantly won over by this link from quantum theory to life-sized physical systems, it was inevitable I would choose to make my master thesis with Stefaan at the Center for Molecular Modeling .

My choice of subject fell on a benchmark study of Density-functional theory for surface properties. Both Stefaan's enthusiasm and the benchmarking work performed by Kurt conveyed me to this ambitious stroll around the periodic table; I can honestly say I have not regretted it a single moment. Although at times I have felt more like an accountant than a physicist or engineer, the never-faltering aid and advice of Michael and Kurt were always there to thrive me onwards. I sincerely thank them for not resorting to barring their doors to keep me out of their offices.

It must be said the warm welcome offered by the CMM to their thesis students is very much appreciated. I would like to thank Professor Veronique Van Speybroeck for placing the facilities - of which the existence is largely thanks to her - at our disposal. The advice and interest shown from all other members of the CMM is very much appreciated as well. Even though they were not official counselors, no one ever hesitated to offer their time and knowledge. My fellow thesis students - we were a numerous and merry bunch - deserve gratitude as well, especially for their indulgence of my silly jokes or the slinging of profanities at my laptop screen.Thank you Arthur and Michiel for the great friendship these last few years. Thank you Jelle for this pleasant year together at the CMM. Although he only joined halfway through the thesis year, thank you Bavo for all those lighthearted moments in our office.A formal thanks goes out to Ghent University, for offering such a wonderful education opportunity and to the people of the High Performance Cluster - though I disagree with my priority in their queuing system.

My family and friends are to be congratulated on suffering my mood swings throughout the thesis process. If they were not having to hear me drone on insufferably about a subject they know or care little about, they were facing my complaints on how long my calculations were queued on the hpc. Both my parents deserve a very special thanks, not just in regards to the past year. Their trust in my decisions and patience with my flaws are commendable.

A person who is no longer alive but to whom I owe an enormous gratitude is Ayn Rand. Had it not been for the reading of "The Fountainhead" and "Atlas Shrugged", I would have never resumed my engineering studies. I would like to conclude with one of her quotes, which profoundly expresses the spirit of scientific research:

> When I disagree with a rational man, I let reality be our final arbiter; if I am right, he will learn; if I am wrong, I will; one of us will win,but both will profit
>
> Ayn Rand

Sam De Waele
Ghent, May 22nd 2015

Error estimates for ab initio predictions of surface energy and work function

by

Sam De Waele

Supervisors: Prof. dr. Stefaan Cottenier, Prof. dr. ir. Veronique Van Speybroeck,
Counsellors: Dr. ir. Kurt Lejaeghere, ir. Michael Sluydts

Master's dissertation submitted in order to obtain the academic degree of
Master of Science in Engineering Physics

Department of Applied Physics
Chairman: prof. dr. ir. Christophe Leys
Department of Materials Science and Engineering
Chairman: prof. dr. ir. Joris Degrieck
Faculty of Engineering and Architecture
Academic year 2014-2015

Overview

The surface properties of a material are important for many practical applications. The measurements of these properties are often difficult and subject to large errors. Because of this, theoretical predictions can present a significant contribution to surface science. In the last two decades, Density-Functional Theory has become a popular tool for the ab initio modeling of surfaces. This study aims to asses the accuracy of DFT for two important surface properties: work function and surface energy. The goal is to chart the general trend for all material types, by defining the entire periodic table as test set and performing a rigorous statistical analysis. It was found both the LDA and PBE functional produce work functions with an accuracy that rivals the accuracy typically found for an experimental work function. Surface energies suffer from larger inaccuracies with respect to experiment. It was concluded LDA is a better functional for predicting accurate surface energies. This study provides a straightforward protocol which can be used by other researchers – both theoretical and experimental – to derive expected experimental values from DFT-predicted surface properties.

Keywords

surface energy, work function, density-functional theory, error estimates, benchmarking

Error estimates for ab initio predictions of surface energy and work function

Sam De Waele

Supervisor(s): Prof. dr. Stefaan Cottenier, Prof. dr. ir. Veronique Van Speybroeck
Counsellor(s): Dr. ir. Kurt Lejaeghere, Ir. Michael Sluydts

Abstract—**The surface properties of a material are important for many practical applications. The measurements of these properties are often difficult and subject to large errors. Because of this, theoretical predictions can present a significant contribution to surface science. In the last two decades, Density-Functional Theory has become a popular tool for the ab initio modeling of surfaces. This study aims to asses the accuracy of DFT for two important surface properties: work function and surface energy. The goal is to chart the general trend for all material types, by defining the entire periodic table as test set and performing a rigorous statistical analysis. This result can subsequently be used by other researchers – both theoretical and experimental – to interpret DFT-predicted surface properties.**

Keywords—**surface energy, work function, density-functional theory, error estimates, benchmarking**

I. Introduction

As Moore's law still holds true, the capabilities of computational physics continue to increase rapidly. Methods that solve the Schrödinger equation to improve the understanding of physical systems gain ever more prominence as their reach in system size expands. One of these *ab initio* methods is Density-functional theory (DFT). Within this framework, electron-electron interaction that is not included in the electrostatic repulsion is approximated by a functional of the electron density.[1], [2]

Nowadays DFT can be used to model surfaces of most crystalline materials and calculate the relevant properties such as surface energy and work function. Moreover, by calculating the forces on the ions the optimized surface structure can be obtained.

There have been a number of studies attempting to asses the accuracy of DFT-predicted surface properties[3], [4], [5], [6]. Most of these studies only consider a limited test set of materials and present only a qualitative comparison of DFT with experiment. The present work aims to avoid both of these pitfalls by including the entire periodic table in the test set and performing a rigorous statistical analysis on the comparison between ab initio results and experiment. This approach mimics the one taken by Lejaeghere et al.[7] in estimating the error of DFT predictions for bulk properties. The surface properties chosen as benchmark quantities are the work function and surface energy. For these two properties, experimental data is most abundant and they can be derived from DFT calculations in a straightforward fashion.

S. De Waele conducted this work at the Center for Molecular Modeling, Ghent University (UGent), Ghent, Belgium. E-mail: sdwaele.DeWaele@ugent.be .

II. Methodology

A. DFT calculations for surfaces.

To model the surface of a material in a 3D periodic code, a a slab model is constructed from the bulk geometry by creating a supercell of N bulk atoms along a specific orientation and inserting vacuum into this structure.

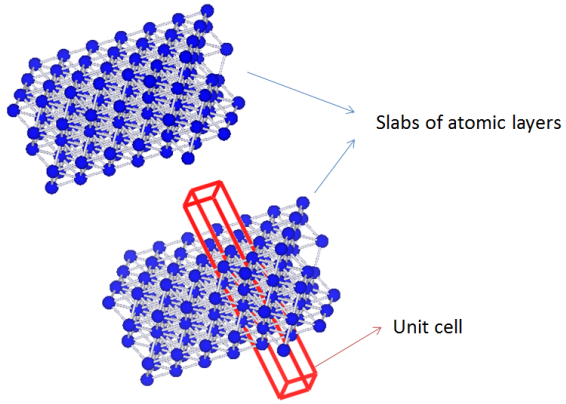

Fig. 1: Slabs of atomic layers for modeling a <100> surface for a face-centered cubic (fcc) material.

This creates periodically repeated slabs of atomic layers that each have two surfaces of a given crystallographic orientation. To derive the surface energy σ, the bulk energy E_{bulk} is subtracted N times from the total slab energy E_{slab} and the result is divided by two to account for there being a surface at each side of the slab:

$$\sigma = \frac{1}{2}(E_{slab} - N \times E_{bulk}) \tag{1}$$

This corresponds to the energy required to create a surface with area corresponding to the lateral size of the supercell. This area must be taken into account to transform σ into a value comparable to other calculations and experiment. To differentiate the normalized surface energy from σ, it is usually indicated by γ and expressed in $\frac{J}{m^2}$.

Whereas the ab initio surface energy is derived from the comparison of two calculations (Eq. 1), the work function is can be directly obtained from the slab calculation. By solving the Kohn-Sham equations, the Fermi energy E_F and the local electrostatic potential energy $V(\vec{r})$ are obtained. The work function is then:

$$\Phi = V_{vac} - E_F \tag{2}$$

where V_{vac} is at a location in the vacuum where $V(\vec{r})$ becomes constant.

Ab initio calculations were performed for all elements from Group 1 through Group 14 for all elements lighter than Bi, except for H, B, Ga, In, Hg and Mn. For the cubic crystal structures the $\{100\}$, $\{110\}$ and $\{111\}$ surfaces were taken into account. For the hcp structures the $\{0001\}$, $\{10\bar{1}0\}$ and $\{12\bar{3}0\}$ surfaces were simulated. The $(2 \times 1)\{111\}$ and the $(2 \times 1)\{100\}$ surface reconstructions for C, Si, Ge and Sn in the diamond lattice were included. Sn was also considered in its tetragonal structure and C (graphite) is also included. Spin-polarized calculations were needed for the magnetic elements Fe, Co, Ni and Cr, where the latter was also calculated in a non-magnetic state. Convergence tests were performed for the meshing in reciprocal space, cut-off energy, slab thicknesses and layers allowed to relax. The imprecisions associated with these settings were never larger than $60meV$ for work functions and never larger than 5% for surface energies. The thickness of the vacuum in between slabs was always chosen to be near $20\mathring{A}$. Structure optimization was performed with Methfessel-Paxton smearing[8], but all other calculations used the Tetrahedron method with Blöchl corrections[9]. The Vienna Ab Initio Package (VASP) software [10], [11], [12], [13] with frozen-core PAW potentials[14] was used for all calculations. For all surfaces both the LDA[15] and PBE[16] exchange-correlation functional were used to examine the impact of a different level of theory.

B. Comparison with experiment

Measuring the surface energy of a solid is extremely difficult and prone to large errors. Because of this, the most reliable source for experimental data is a semi-empirical derivation of the solid surface energies from the liquid surface tensions by Tyson and Miller [17]. This derivation was applied for all elements in the periodic table for which reliable liquid surface tensions could be obtained. The size of the data set and the transparency of the method make it possible to estimate a consistent error for the obtained surface energies. The surface energies presented by Tyson and Miller have no anisotropic information, they are surface energies for a surface of "general orientation". This hampers the comparison with the DFT results, as these are intrinsically anisotropic. One can, however, derive the average surface energy by assuming the transformation from one surface into another to consist only of adding ledges to a flat surface, or removing them. This reasoning stems from the TLK model for surfaces[18]. It enables the deduction of, for example, the general surface energy $\gamma(\theta)$ in between the calculated surface energies γ_{100} and γ_{110}. In this manner it is possible to construct a surface energy in a general direction from the ab initio calculations fit for comparison with experimental data.

Work function measurements are decidedly more precise than surface energy measurements. The source of inaccuracies lies in the presence of surface defects. Adsorbed impurities or structural surface defects can dramatically alter the measured work function. A thorough review of available work function data was recently made by Kawano[19]. Not all elements are included in this review. Nevertheless, it provides a wealth of information on the discrepancy between different experiments measuring the work function for the same element and surface. By analyzing this large data set, it is possible to determine accurate errors for the elements reviewed by Kawano. From this analysis a general accuracy of work function measurements can be estimated. This is a useful tool for evaluating the well-known source of work function data compiled by Michaelson[20], which lacks rigorous discussion of experimental errors but provides data for more elements than Kawano. For many elements there is only a polycrystalline work function available, which corresponds to a surface with facets of different crystallographic orientation. It is the surface calculation yielding the lowest anisotropic work function that corresponds best with the one that is measured for a polycrystalline surface[21].

C. Statistical analysis

A theoretically expansive description of the methods used in this section can be found in[22], but the emphasis here lies on the interpretation of the statistical concepts for DFT error analysis. As done previously in the work by Lejaeghere et al., a linear regression using a standard least-squares fit was made between the experimental data Y and DFT data X. The objective was to characterize the DFT result as a *prediction* for experiment, taking into account the fact it contains a size-dependent error β_1 and a constant error β_2:

$$Y = \beta_1 X + \beta_2 \tag{3}$$

Given a population of DFT and experimental data (size N), the maximum-likelihood estimates for β_1 and β_2 are found by minimizing the penalty function of the regression:

$$P = \sum_i^N (\beta_1 X_i + \beta_2 - Y_i)^2 \tag{4}$$

This penalty function is a measure for the residual error of the data compared to the linear regression. An unbiased estimator for this standard error on the regression (SER) is :

$$SER = \sqrt{\frac{\sum_i^N (\beta_1 X_i + \beta_2 - Y_i)^2}{N-2}} \tag{5}$$

The SER of a linear regression on a data set of DFT and experimental values is thus the expected residual error made by the DFT prediction. If it were zero, DFT would model the actual physical result perfectly but for a constant offset and a relative error. These errors are obtained with respect to the entire data set and thus are material independent.

The analysis becomes somewhat more intricate if there is an imprecision on the experimental data. In this case, one cannot simply punish each quadratic error equally harsh in the penalty function. Instead, a weighted least-squares fit can be used which normalizes the difference between the linear fit and the data point to the standard deviation:

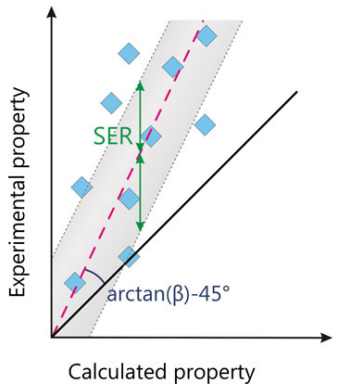

Fig. 2: An illustration of the meaning of the SER. It is a variable, residual error on top of a systematic deviation. Image by Lejaeghere et al.[7]

$$P_{weight} = \sum_i^N \frac{1}{\sigma_i^2}(\beta_1 X_i + \beta_2 - Y_i)^2 \tag{6}$$

The weights σ^2 are determined by the experimental errors. The SER is deduced in the same way from P_{weight} as it is from P for the normal regression. Its interpretation is somewhat different however, as it now becomes a dimensionless number due to the normalization on the standard deviation. A perfect prediction will no longer produce an SER equal to zero, but equal to one. The residual error relative to the weighted regression can never be smaller than the error on the experimental data.

III. Results

The weighted linear regression explained in section II-C is applied to the data for surface energies and work functions. Both for LDA and PBE, the predicted quantities are compared with experiment in Figures 3 to 6. Be Cr are considered as strong outliers with respect to the general trend. The bad performance for both work function and surface energy of the former is suspected to be caused by highly inaccurate experimental data. Cr, on the other hand, has a strong magnetism at the surface which might be the cause of the faulty surface energy. Both these elements were omitted from the linear regression. They are however indicated in the figures to highlight their outlying position.

The results from the fitting procedures on the four comparisons with experiment are shown in table I. The nature of the errors is different for work function and surface energy. Whereas surface energy has no constant error for both LDA and PBE, the difference between PBE and experimental work functions is almost constant. The trend of the LDA work functions is a mixture of a constant and a size-dependent discrepancy with respect to experiment. From the SER values it is clear LDA is a better functional for obtaining surface energies. When the overestimating trend is corrected for, i.e. one would scale the LDA result with 0.866, the residual error is significantly lower compared to the one for PBE. The choice of functional is somewhat more difficult when accurate work functions are desired. LDA might have

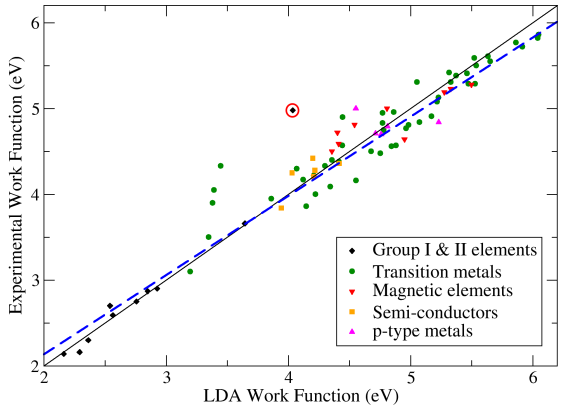

Fig. 3: Comparison of experimental to LDA work function, with the weighted linear regression (blue line). The outlier Be is highlighted with a red circle.

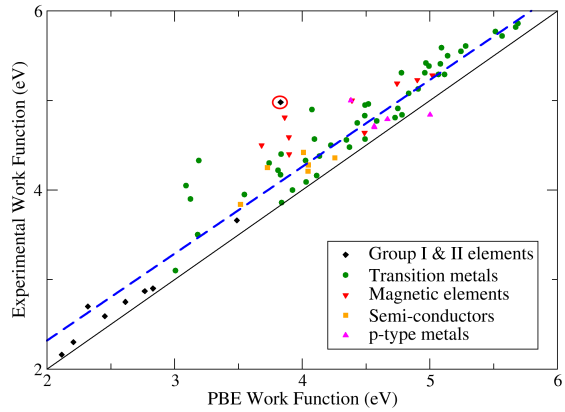

Fig. 4: Comparison of experimental to PBE work function, with the weighted linear regression (blue line). The outlier Be is highlighted with a red circle.

a slightly lower SER, but the fact that PBE has a very small size-dependent error might be more interesting. The general trend between LDA and PBE is almost perfectly linear, with a correlation coefficient of $r = 0.99$ for both work function and surface energy.

Φ	Slope	% error	Offset (eV)	SER
LDA	0.924	8%	0.284	1.406
PBE	0.97	3%	0.378	1.536
γ	Slope	% error	Offset (J/m^2)	SER
LDA	0.866	15 %	0.003	1.651
PBE	1.046	-4%	0.024	1.95

TABLE I: The parameters of the weighted linear fits for work function and surface energy for LDA and PBE without Cr and Be.

One must be careful when singling out individual elements from the test set for comparison with experiment. The significance of a difference between DFT and experiment should always be weighed with respect to the experimental error. Nevertheless, some periodic trends can clearly be observed in the results:

- The Ti group has work functions that are too low for both LDA and PBE, although it should be noted the work function

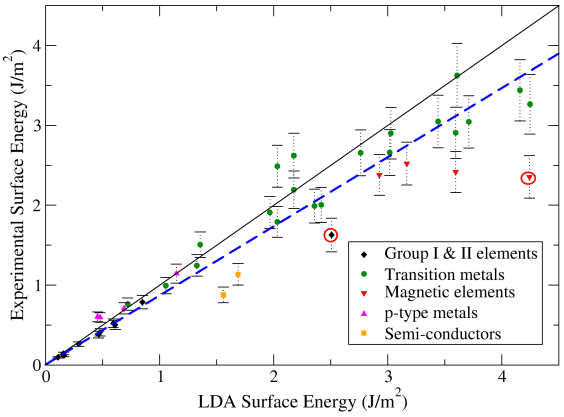

Fig. 5: Comparison of experimental to LDA surface energy, with the weighted linear regression (blue line). The errors bars are derived from the Tyson and Miller method. The outliers Be and Cr are highlighted with a red circle

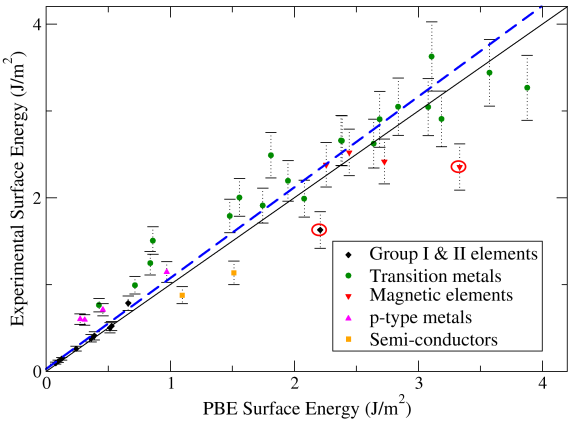

Fig. 6: Comparison of experimental to PBE surface energy, with the weighted linear regression (blue line). The errors bars are derived from the Tyson and Miller method. The outliers Be and Cr are highlighted with a red circle

for Zr is deemed to be unreliable.

- The surface energy for Fe and Cr is significantly overestimated for both LDA and PBE and their work function is underestimated for PBE.
- Elements with almost-full or full d-shells have a surface energy below the regression line, especially the heavier elements. The underestimation is worse for PBE than for LDA.
- The p-type metals show surface energies well below the general trend.
- Ge and Si display elevated surface energies, with Ge also showing a work function significantly below the regression line.
- The heavy elements (bottom row) tend to have less accurate property predictions, especially for LDA. However these deviations are not dramatic, as they are always contained within two standard deviations.

The small SER for work functions for both LDA and PBE suggests DFT-predicted work functions are as reliable as experiment, although the nature of the inaccuracies is completely different for both methods. The prediction of surface energies shows a larger SER. Comparison between the SER for work functions and surface energies depends on the correct assessment of the variance of the experimental data, but since those for surface energies were taken rather large and those for work functions are believed to be exact, the fact that the SER for the latter were lower than for the former indicate DFT-predicted surface energies are less reliable than work functions.

Another line of research, besides the direct comparison between DFT and experiment, is to look for correlations with other material properties. In a further step, the correlation between (absolute or relative) errors made for a particular property can be researched. A strong correlation between errors shed light on the source of the error. DFT-calculated bulk properties and the comparison with experiment were taken from the work by Lejaeghere et al.[7].

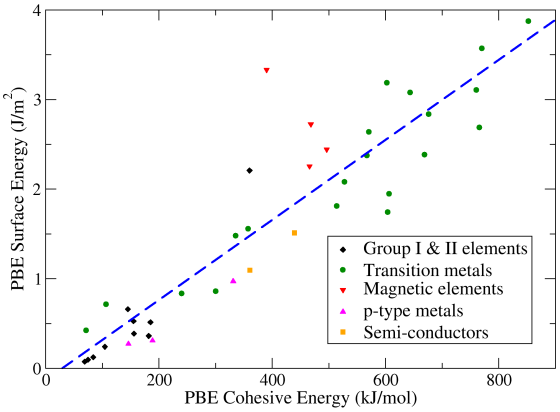

Fig. 7: The surface energy and cohesive energy are strongly correlated. The regression line is shown in blue.

An obvious question is whether the work function and surface energy – both surface properties – are correlated. The correlation coefficient r equals 0.53 for experiment and 0.57 for DFT. The relation between cohesion energy and both surface properties explains the moderate correlation.

Surface energy is very strongly correlated with the cohesive energy. This can be understood from a broken bond model for surface energy, where the energy associated to the removal of a neighboring atom is equal to the bond strength. Stronger initial bonding thus results in a higher surface energy (Figure 7).

One would expect stronger bonding also entails more strongly bound electrons and a higher work function. This is somewhat confirmed by $r = 0.55$ for DFT but not at all for experimental values where $r = 0.33$. The absolute error on cohesive energy is moderately (negatively) correlated ($r = 0. - 48$) with the absolute error on work functions. The same can be said for relative errors on the cohesive energies and surface energies ($r = 0.59$). Both correlations show the importance of cohesive energy for work function and surface energy, but the errors can only partly be correlated.

Within DFT, volume per atom (V_0) is negatively correlated in a strong way with work functions ($r = -0.76$) (Figure 8), which can also be observed in the experimental data ($r = -0.83$). The errors on V_0 are however not correlated at all with errors on the work function. On the other hand, they are moderately negatively correlated with errors on the surface energy ($r = 0.59$). This is because surface energy is expressed in energy per surface; when the size of the surface is overestimated, the surface energy will be underestimated.

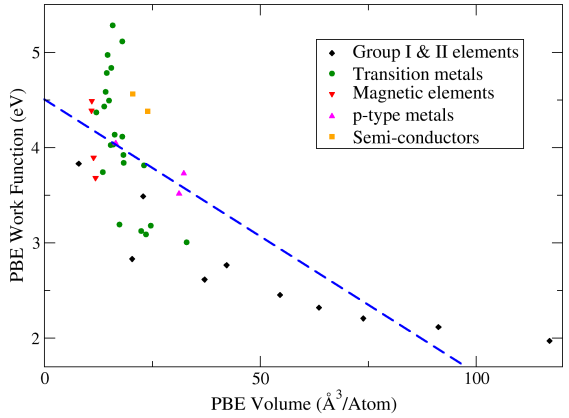

Fig. 8: The work function and volume per atom are negatively correlated. The regression line is shown in blue.

IV. Conclusion and Outlook

The goal of this work was to calculate work functions and surface energies for the entire periodic table with DFT-PBE and DFT-LDA and compare them to experiment. Such a large and representative test set enables a rigorous statistical approach to assess the accuracy of DFT-predicted surface properties. An expansive undertaking of this kind would moreover produce a guideline for how these ab initio results should be quantitatively interpreted. It is believed the present study succeeds in making a well-substantiated comparison between ab initio results and experiment.

Although for some elements there are no experimental data and for other elements no calculations were performed, a representative test set was obtained for the elemental metals. It was concluded both LDA and PBE predict work functions very well for most elements. The most notable exceptions were Ti, Zr, Hf and Ge. Predicting accurate surface energies proved a more difficult matter. These were too low for Pt, Ag, Au, Tl, Sn and Pb. The magnetic elements Fe and Cr were among the worst performers for surface energy as well, especially for PBE.

A very strong correlation was found between cohesive energy and surface energy. Work functions clearly correlated negatively with volume per atom. The error on the volume and the error on the cohesive energy that DFT makes with respect to experiment are good predictors for the error it makes on surface energies. No such clear markers were found for work function errors however.

A first step to improving the current study would be to include those elements for which experimental data are available but no calculations were performed. Surface properties for Mn, Hg, B, Ga, In, As, Sb, Bi, Se and Te would greatly enrich the test set. Simulating a greater variety of surface orientations would provide a better surface energy for experimental comparison, especialy for the hexagonally close-packed elements.

This study limited itself to the use of VASP for performing the calculations. Comparing with a different software could provide a good estimate of the numerical precision of a general DFT calculation. Moreover, using a code that utilizes an all-electron LAPW method would be an interesting benchmarking study for the surface properties obtained with VASP.

Acknowledgments

This work was carried out using the Stevin Supercomputer Infrastructure at Ghent University, funded by Ghent University, the Hercules Foundation and the Flemish Government, department EWI. The author would also like to thank the CMM research group for the opportunity to perform this research as well as their knowledge and guidance.

References

[1] P. Hohenberg and W. Kohn, "Inhomogeneous Electron Gas," *Physical Review*, vol. 136, no. 3B, pp. B864–B871, Nov. 1964.

[2] W. Kohn and Lj Sham, "Self-Consistent Equations Including Exchange and Correlation Effects," *Physical Review*, vol. 140, no. 4A, pp. 1133–&, 1965, WOS:A19657000000015.

[3] L. Vitos, A. V. Ruban, H. L. Skriver, and J. Kollr, "The surface energy of metals," *Surface Science*, vol. 411, no. 12, pp. 186–202, Aug. 1998.

[4] Juarez L. F. Da Silva, Catherine Stampfl, and Matthias Scheffler, "Converged properties of clean metal surfaces by all-electron first-principles calculations," *Surface Science*, vol. 600, no. 3, pp. 703–715, Feb. 2006.

[5] Nicholas E. Singh-Miller and Nicola Marzari, "Surface energies, work functions, and surface relaxations of low-index metallic surfaces from first principles," *Physical Review B*, vol. 80, no. 23, pp. 235407, Dec. 2009.

[6] Jian Wang and Shao-Qing Wang, "Surface energy and work function of fcc and bcc crystals: Density functional study," *Surface Science*, vol. 630, pp. 216–224, Dec. 2014.

[7] K. Lejaeghere, V. Van Speybroeck, G. Van Oost, and S. Cottenier, "Error Estimates for Solid-State Density-Functional Theory Predictions: An Overview by Means of the Ground-State Elemental Crystals," *Critical Reviews in Solid State and Materials Sciences*, vol. 39, no. 1, pp. 1–24, Oct. 2013.

[8] M. Methfessel and A. T. Paxton, "High-precision sampling for Brillouin-zone integration in metals," *Physical Review B*, vol. 40, no. 6, pp. 3616–3621, Aug. 1989.

[9] Peter E. Blöchl, O. Jepsen, and O. K. Andersen, "Improved tetrahedron method for Brillouin-zone integrations," *Physical Review B*, vol. 49, no. 23, pp. 16223–16233, June 1994.

[10] G. Kresse and J. Hafner, "Ab initio molecular dynamics for liquid metals," *Physical Review B*, vol. 47, no. 1, pp. 558–561, Jan. 1993.

[11] G. Kresse and J. Hafner, "Ab initio molecular-dynamics simulation of the liquid-metal/amorphous-semiconductor transition in germanium," *Physical Review B*, vol. 49, no. 20, pp. 14251–14269, May 1994.

[12] G. Kresse and J. Furthmüller, "Efficiency of ab-initio total energy calculations for metals and semiconductors using a plane-wave basis set," *Computational Materials Science*, vol. 6, no. 1, pp. 15–50, July 1996.

[13] G. Kresse and J. Furthmüller, "Efficient iterative schemes for *ab initio* total-energy calculations using a plane-wave basis set," *Physical Review B*, vol. 54, no. 16, pp. 11169–11186, Oct. 1996.

[14] P. E. Blöchl, "Projector augmented-wave method," *Physical Review B*, vol. 50, no. 24, pp. 17953–17979, Dec. 1994.

[15] J. P. Perdew and Alex Zunger, "Self-interaction correction to density-functional approximations for many-electron systems," *Physical Review B*, vol. 23, no. 10, pp. 5048–5079, May 1981.

[16] John P. Perdew, Kieron Burke, and Matthias Ernzerhof, "Generalized Gradient Approximation Made Simple," *Physical Review Letters*, vol. 77, no. 18, pp. 3865–3868, Oct. 1996.

[17] W. R. Tyson and W. A. Miller, "Surface free energies of solid metals: Estimation from liquid surface tension measurements," *Surface Science*, vol. 62, no. 1, pp. 267–276, Jan. 1977.

[18] J. F. Nicholas, "2.1.1.5.1 The terrace-ledge-kink (TLK) model," in *Structure*, G. Chiarotti, Ed., vol. 24a, pp. 37–39. Springer-Verlag, Berlin/Heidelberg, 1993.

[19] Hiroyuki Kawano, "Effective work functions for ionic and electronic emissions from mono- and polycrystalline surfaces," *Progress in Surface Science*, vol. 83, no. 12, pp. 1–165, Feb. 2008.

[20] Herbert B. Michaelson, "The work function of the elements and its periodicity," *Journal of Applied Physics*, vol. 48, no. 11, pp. 4729–4733, Nov. 1977.

[21] M. G. Helander, M. T. Greiner, Z. B. Wang, and Z. H. Lu, "Pitfalls in measuring work function using photoelectron spectroscopy," *Applied Surface Science*, vol. 256, no. 8, pp. 2602–2605, Feb. 2010.

[22] Larry Wasserman, *All of Nonparametric Statistics*, Springer, New York, May 2007.

Contents

List of Figures

List of Tables

List of abbreviations

DFT	Density-Functional Theory
TLK	Terrace Ledge Kink
FERP	Field Emission Retarding Potential
CPD	Contact Potential Difference
scf	self-consistent field
LDA	Local-Density Approximation
GGA	Generalized Gradient Approximation
B88	Becke 88
LYP	Lee-Yang-Parr
P86	Perdew 1986
PW91	Perdew 1991
PBE	Perdew-Burke-Ernzerhof
LCAO	Linear Combination of Atomic Orbitals
BZ	Brillouin Zone
PP	Pseudopotential
PAW	Projector Augmented-Wave
VASP	Vienne Ab initio Simulation Package
fcc	face-centered cubic
bcc	body-centered cubic
hcp	hexagonal close-packed
TDDFT	Time-Dependent Density-Functional Theory
QSE	Quantum Size Effects
SDW	Spin-Density Wave
SER	Standard Error of the Regression
FLAPW	Full-potential Linearized Augmented Plane Wave
LEED	Low-Energy Electron Diffraction

List of symbols

γ	Surface Energy ($\frac{J}{m^2}$)
σ	Surface Energy ($\frac{eV}{atom}$), smearing parameter
α	$\frac{\gamma_{SL}}{\gamma_{SV}}$
T	Temperature, kinetic energy
T_{DB}	Debye temperature
T_m	Melting temperature
S	Entropy (in this work specifically surface entropy)
b	Ledge energy
a	Lattice parameter
Φ	Work Function
Ψ	Many-body wave function
$\hbar$	Planck's constant
M	Nucleus mass
Z	Atomic number
m_e	Electron mass
e	elementary charge
ϵ_0	Permittivity of the vacuum
$\delta(\vec{r})$	Dirac distribution
ρ	Electron density
E	Energy
V	Potential energy, local potential
F_{HK}	Hohenberg-Kohn density functional
V_{ext}	Exterior potential
$E_{xc}[\rho]$	Exchange-correlation functional
$\epsilon_{XC}(\rho(\vec{r}))$	Exchange-correlation function
V_{vac}	Local potential in the vacuum

E_{coh}	Cohesive energy
$\hat{H}$	Hamiltonian
ϕ	Eigenfunction of the Kohn-Sham single-particle eigenequation
ϵ	Eigenvalue (energy) of the Kohn-Sham single-particle eigenequation
μ_B	Bohr magneton
ϵ_F	Fermi energy
Θ	Fermi-Dirac distribution
Ω_{BZ}	Volume of the Brillouin zone
$\vec{k}$	Reciprocal wave vector
$\vec{K}$	Reciprocal lattice vector
E_{cut}	Cut-off energy
$\tilde{\phi}$	Pseudo-wave function
$\mathcal{T}_R$	Operator defining the transformation between $\tilde{\phi}$ and ϕ
β_1	Slope of the linear regression
β_2	Intercept of the linear regression
P	Penalty function for the linear regression
P_{weight}	Penalty function for the weighted linear regression
B_0	Bulk modulus
V_0	Equilibrium volume

Chapter 1

Introduction

Performing ab initio calculations entails starting from an unbiased theoretical principle in order to obtain an observable quantity. When this starting point is the Schrödinger equation, *every* observable quantity can be derived from the ab initio calculation. The – ambitious – goal is to solve a system *entirely*. Because of the conscious choice to steer clear of any empirical input, the computations are not bound by the experimental limitations. The feasibility or precision of the practical set-up is no longer a concern. Conversely, the validity of the result largely depends on the ability to model the system at hand.

Because solving the Schrödinger equation is such a demanding task, being able to scale an atomic-size calculation to real-world dimensions is the present challenge for ab initio material science. The unit cell of a crystalline solid, most often of atomic size, represents an infinite translational symmetry. The innate beauty of this symmetry is the wealth of macroscopic properties contained in such a small subspace of the entire solid.

In reality, the translational symmetry in the crystalline solid is not infinite. At some point the crystal is terminated or deformed. This is where surfaces, grain boundaries and impurities enter the problem. The famous quote by Enrico Fermi *"If God created the bulk, the Devil created the surface"* highlights these annoying breaks in the translation symmetry. Unfortunately, many material properties are especially governed by the characteristics of this termination of the bulk and its interaction with the environment – adsorption, electric contacts and topology of grain boundaries just to name a few.

As is the case for Newtonian mechanics, there is – in general – no analytic solution for the three-body problem in quantum mechanics. Even the helium atom cannot be solved exactly. If one is to tackle the Schrödinger equation for an entire unit cell – which may contain hundreds of interacting particles – a sound numerical method is required. One of these which has become prominent over the past twenty years is Density-Functional Theory (DFT), which will be explained in Chapter 3. Already in 1970 – 1971 it was Walter Kohn himself, in collaboration with Lang, who proposed utilizing DFT for calculating work functions and surface energies for simple metal surfaces[1,2].Nowadays, DFT can be found in a variety of ab initio surface studies.[3] Despite this widespread application, there has not been a rigorous quantitative study on the general accuracy of DFT for predicting these surface properties. The purpose of this thesis is to fill this void. The test set consists of all elements in the entire periodic table, at least those which are experimentally relevant. Benchmark properties will be the work function and surface energy. Not only can they be derived fairly easily and unambiguously from a DFT calculation, but experimental values for both material properties

are also consistently available for the entire test set. When eventually a quantitative relation is established between DFT and experiment, this can help other researchers, both experimental theoretical, to interpret the DFT-predicted surface energies and work functions.

It is not a specific objective to discuss the accuracy for any individual material, but some interesting cases will be examinedin detail. The emphasis lies on comparing two sets of data – theoretical and experimental – which are each intrinsically consistent. This highlights the importance of a uniform experimental data set and a consistent computational approach to obtain the ab initio data. Primarily focusing on a quantitative comparison for an entire (large) test set is in stark contrast to previous comparisons of DFT surface calculations with experiment. Usually, the goal is to highlight specific shortcomings and adaptations of the theory to improve correspondence with experiment. By evaluating a large and varied test set to establish a general relation with ab initio prediction and experiment, the current work can serve as a guideline for correctly assessing DFT-predicted surface properties. This thesis can be seen as an expansion on the recent work by Lejaeghere et al.[4], who quantified the accuracy of DFT for bulk properties. The manner in which DFT results are compared to experimental data in this thesis is similar to the approach taken by Lejaeghere.

As comparison with experiment is in this case not a trivial matter – it never is – the next chapter will discuss the available experimental data. The specifics of these data have a major impact on how the ab initio results need to be evaluated. As already mentioned, chapter three will briefly explain DFT along with the technical details of how a surface is exactly modeled within this framework. The aim of this chapter is to inform the reader about DFT inasmuch as it is necessary to comprehend the calculations carried out within this work – thus creating a document which is self-sufficient and accessible to anyone with a background in physics. Chapter three is concluded with a short overview of DFT benchmarking. A number of interesting studies comparing DFT surface calculatinos with experiment are summarized.

In chapter 4, the details of all simulations will be discussed. This chapter largely follows the workflow of the thesis project itself, touching on a variety of problems as they were encountered during the process. Some case studies are introduced in this chapter, serving the specific purpose of discussing these problems. In chapter 5 all results will be bundled and compared statistically to experimental data. The details of the statistical methods involved will be presented there as well.

Chapter 2

Experimental Data

Before discussing any aspect of the ab initio calculations, an evaluation of the available experimental data is in order. The surface energy and work function were selected as benchmark properties because these are the most commonly available surface properties. If one wishes to scan a large part of the periodic system in a consistent manner, reliable experimental data for comparison are needed – preferably with precision errors – for all elements.

2.1 Surface Energy

The surface energy of a solid is the minimum work required to create a surface. Measuring this energy is not a straightforward task. Because of this inherent difficulty, a myriad of methods have been put forward to try and obtain the surface free energy of solids. Almost all – reliable – methods are based on analyzing the geometry of a structure in thermodynamic equilibrium, which is determined by the minimization of the interface energies. A basic example set-up is shown in Figure 2.1 where a liquid drop is placed on a solid. The solid and liquid can be of the same material, but this is not a necessity. The surface energies determine the contact angle θ through Young's equation[1], minimizing the surface free energy of the droplet:

$$\gamma_{SV} = \gamma_{SL} + \gamma_{LV}\cos(\theta) \tag{2.1}$$

The surface energy of the liquid γ_{LV} can be measured separately – by measuring the bubble size of an inert gas in the liquid for example – and the contact angle θ between the liquid and solid can be observed in the set-up. The difficulty consists in determining the solid-liquid interaction γ_{SL}. Most attempts to cope with this problem involve assuming a general relation between γ_{SL} and the separate solid and liquid properties. A short and clear overview of the most frequently used approximations was recently made by Ozcan and Hasirci[7] in 2008. Although their research was limited to measuring – using several of those approximations – the surface free energy of polymeric films, the conclusion was a common one for all solids: *direct measurement of surface free energy is unacceptably imprecise with the range of results often as large as the results themselves.*

[1] This equation has been around for moren than 200 years, but the correct general proof is not straightforward at all[5].

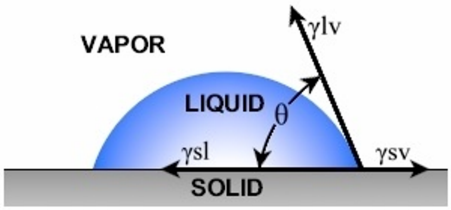

Figure 2.1: Schematic drawing of a surface energy experiment.[6]

The most common reference for surface energies of solids is the work by Tyson and Miller (1977)[8]. Because of the large inaccuracies involved in experimental measurements, they constructed a model to extrapolate γ_{SV} from γ_{LV} – which can be measured a lot more accurately – at the melting temperature T_m.

At the melting temperature it is assumed the solid-liquid-vapor interface of a material obeys $\gamma_{SV} = \gamma_{SL}+\gamma_{LV}$. This assumption follows from observing how solid metals cannot be heated above their melting temperature T_m, which implies there is no nucleation barrier for surface melting: $\gamma_{SV} \geq \gamma_{SL} + \gamma_{LV}$. If this inequality is combined with the assumption that the surface does not melt below the melting temperature of the bulk (which means $\gamma_{SV} \leq \gamma_{SL}+\gamma_{LV}$), one indeed concludes $\gamma_{SV} = \gamma_{SL}+\gamma_{LV}$. This ignores any possible anisotropy of γ_{SL} and only constitutes an average for the surface energy of the solid.

The problem is now reduced to determining the ratio γ_{SV}/γ_{LV}. This ratio can be rewritten:

$$\gamma_{SV}/\gamma_{LV} = \alpha/(1-\alpha) \tag{2.2}$$

with $\alpha = \gamma_{SL}/\gamma_{SV}$.

The parameter α is a material – and orientation-dependent – constant and can be deduced by determining γ_{SL}/γ_{gb} and γ_{gb}/γ_{SV} from experimental data – with γ_{gb} the interface energy of an *average high-angle grain boundary*.

γ_{SL}/γ_{gb} was determined for Zn and Al by Miller and Chadwick (1967)[9]. The dihedral angle ϕ of a solid precipitate at a grain boundary, as shown in Figure 2.2, is determined by the relative magnitudes of γ_{SL} and γ_{gb}. The values for Zn and Al were used for all metals. The other ratio needed to obtain the parameter α is derived in a similar way. At the triple junction of a surface and a grain boundary of a polycrystalline film, the angle of the groove is determined by γ_{gb}/γ_{SV} (Figure 2.3). Experimental data for this ratio are available for a number of materials and were summarized by Tyson and Miller[8], yielding interesting information on the material dependency. The ratio varies from 0.24 to 0.38 yet the authors chose to apply an average value of 0.33.

Tyson and Miller claimed (their arguments are omitted here) the parameter $\alpha = 0.15 \pm 0.03$ to be largely material independent – quite convenient as the ratio γ_{SL}/γ_{gb} is derived solely from Zn and Al data. This entails the material dependency of the surface free energy γ_{SV} is only present in the experimentally mea-

sured surface tension γ_{LV} [2] and no anisotropic information is available. From the derivation of the factor α, the ratio $\frac{\gamma_S V}{\gamma_S L}$ equals 1.18 ± 0.03. Tyson and Miller were not the first authors to try and evaluate this ratio, other values in literature range from 1.09 to 1.33. When using their experimental data for comparison with ab initio data, the large spread on this conversion factor according to different authors will be taken as the standard error of the conversion.

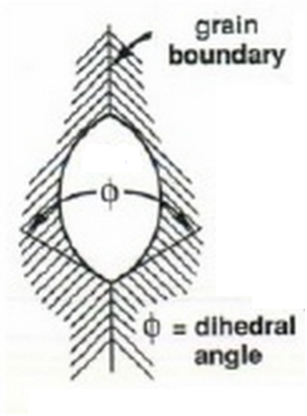

Figure 2.2: The dihedral angle of a liquid precipitate at a grain broundary[11]

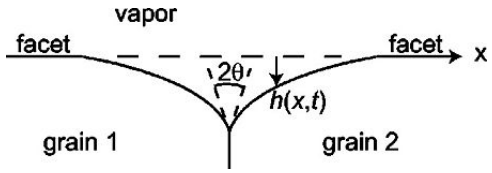

Figure 2.3: Cross-section of a triple junction of a polycrystalline material near the surface.[12]

The above derivation only yields the surface energy of the solid at melting temperature, in a next step one would wish to formulate the temperature dependence in a quantitative way. To extrapolate the surface energies to $0K$, an estimation of the contributions to the surface entropy has to be made.[3]

This entropy consists of a configuration and vibration contribution:

$$\frac{\mathrm{d}\gamma_{SV}}{\mathrm{dT}} = S = S_{vib} + S_{conf} \tag{2.3}$$

S_{vib} originates in the altered vibrational modes of surface atoms compared to atoms in the bulk. Tyson[8,13] used a Debye model to estimate $(S_{vib})_{max} \approx 0.8R$ per mole at the Debye temperature T_{DB}, with R the ideal gas constant. When applying the Debye model to a variety of crystals, S_{vib}/R does vary over a large range (0.2 to 1.1). The vibrational modes associated with the entropy are activated with increasing temperature, illustrated by the first slope in Figure 2.4 from $0K$ to $T = T_{DB}$. At $0K$ they are all frozen. A linear increase is then assumed up to the Debye temperature, which is taken at $T_{DB} = 0.2T_m$. Typical Debye temperatures for metals range from $0.1T_m$ to $0.3T_m$[13].

Starting from about $T = 0.5T_m$, surfaces undergo a roughing[4] transition. As structural defects become en-

[2]There has been some (heated) discussion[10] on the relationship between surface tension of a solid and its surface free energy – the Shuttleworth equation. In this work *surface tension* is always used for liquids – which will not be often – and *surface (free) energy* for a solid. What the impact of this recent discussion might be on the surface energies published by Tyson and Miller is beyond the scope of this work and most likely not quantitatively meaningful.

[3]This ignores two other possible contributions. An electronic contribution from electrons occupying higher levels at increased temperature and the energy of the phonons besides their entropy.

[4]*roughing* or *roughening* are both used in this meaning.

ergetically favourable, the surface becomes increasingly vicinal[5]. A linear evolution of S_{conf} is assumed between $T = 0.5T_m$ and $T = T_m$ with $S_{conf}(T_m) = R$. Again, this is a quite crude approximation. The evolution of the total entropy as a function of temperature is displayed in Figure 2.4.

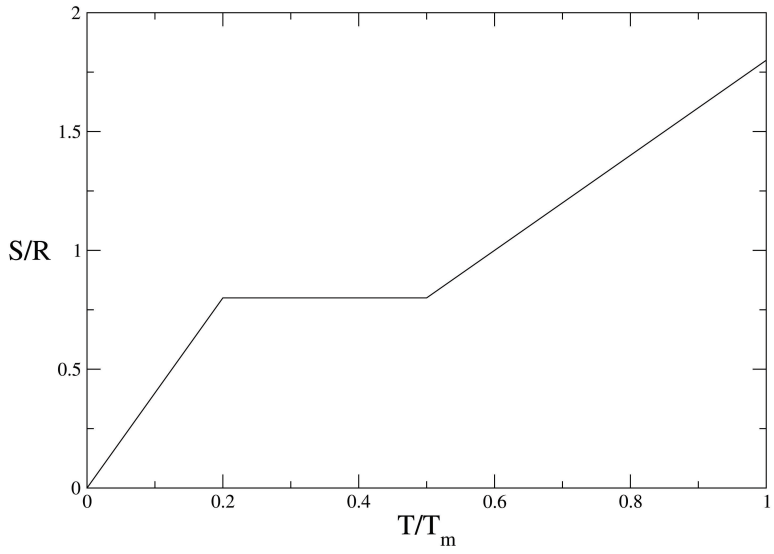

Figure 2.4: The surface entropy S as a function of temperature in the simplified model of Tyson and Miller

There is now a function $S(T)$ which can be used for the entropy of the surface. However, this is the entropy per mole and it does not take into account the surface area A of one mole of material. Tyson[13] made an estimate of this for every element based on the molar volume. Note how this is an area where the crystallographic orientation of the surface might be inserted into the entropy. However, as all anisotropic characteristics were hitherto ignored, the most consistent approach is to derive the planar molar density from the three-dimensional molar density. Eventually the following applies:

$$\gamma_{SV}(T) - \gamma_{SV}(T_m) = \int_{T}^{T_m} \frac{S(T')}{A} \mathrm{d}T' \tag{2.4}$$

Figure 2.5: Summary of the process to obtain the surface free energy at $0K$.

In Figure 2.5 the basic steps in the scheme are shown. Reliable data for γ_{LV} are available only for 49 elements in the periodic table, of which 47 are highlighted in Figure 2.6. Tyson and Miller give experimental

[5] A term frequently used to describe real surfaces. It is most meaningful as an aberration from an ideal terrace-like surface.

values for uranium and neodymium as well, but these heavy elements will not be considered in this work.

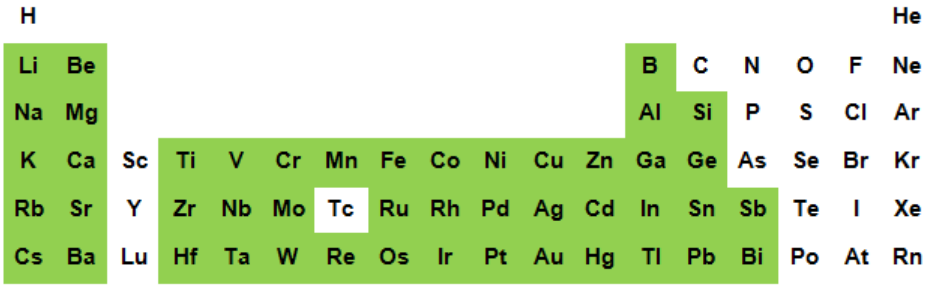

Figure 2.6: Elements for which a reliable surface energy can be derived are highlighted in green.

In the introduction to this paragraph, it was already mentioned that ab initio *anisotropic* surface energies need to be compared with experimental ones that are of *average orientation*. It is a consistent problem in publications comparing DFT surface energies to experiment that the Tyson and Miller results are put in juxtaposition to the ab initio data without an effort to make them coherent. For some elements – most prominently the alkaline metals – there is hardly any anisotropy of the surface energy. Other elements can show a variation of up to 20% in their surface energy depending on the orientation. How can the single *average* surface energy [6] be derived from three (in the cubic crystal case) or more calculated ones from differently oriented surfaces?

Let us phrase the question in another way: what is the relation between the surface energy of the low-index (simple) surfaces that can be simulated[7] and a general surface energy? If an analytic expression could be constructed for a random direction, deriving an average surface energy would be straightforward. The Terrace ledges kink (TLK) model[14] allows us to construct such a general surface energy. The starting point is the terrace, the simple surface without any defects. When the orientation is slightly changed, ledges are *added* to the surface. Let us demonstrate this with the {100} surface of a crystal with cubic symmetry. Suppose this simple surface has a free energy contribution of γ_0, expressed in energy per surface area. If one now wishes to obtain the surface energy of a {510} surface, all it takes is to add a ledge – or step – every 5 unit cells, as illustrated in Figure 2.7. Adding such a ledge comes at an energetic cost, which can be expressed as a line defect in $\frac{J}{m}$. Extending this idea of *constructing* random surface orientations using ledges to general directions, the following expression applies: [8].

$$\gamma(\theta) = \gamma_0 \cos(\theta) + \frac{b}{a} \sin(\theta) \tag{2.5}$$

By using the calculated surface energies for some low-index directions the ratio $\frac{b}{a}$ can be fitted; the physical meanings of b (the ledge energy) and a (the lattice parameter) are thus only of underlying theoretical importance for the model. For a cubic sample for example, one then obtains a general expression for $\gamma(\theta)$ for surfaces with their normal in the {110} planes and the {100} planes, of which there are six and three respectively. Such a function $\gamma(\theta)$ for a surface energy in a general direction is called a Wulff plot.

[6] One could argue the Tyson and Miller surface energies are not exactly linked to *average* directions, as grain boundaries and surface orientations are typically thermodynamically favored orientations.

[7] In theory, all surface orientations can be simulated. The computational cost increases dramatically for higher-index planes.

[8] Strictly speaking, equation 2.5 is only valid for low angles θ, where there is no interaction between the ledges.

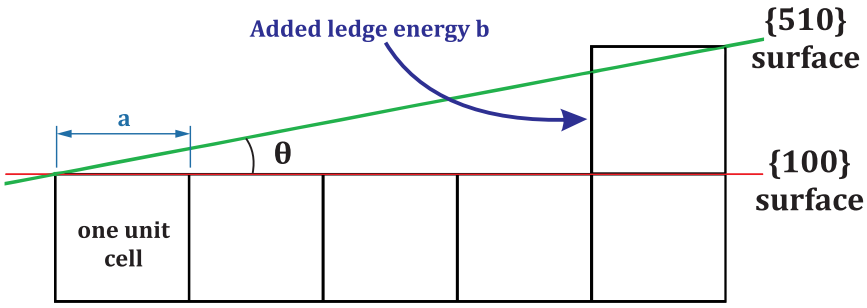

Figure 2.7: Illustration of the construction of a higher-index surface. Adding a ledge increases both the surface free energy and the surface itself.

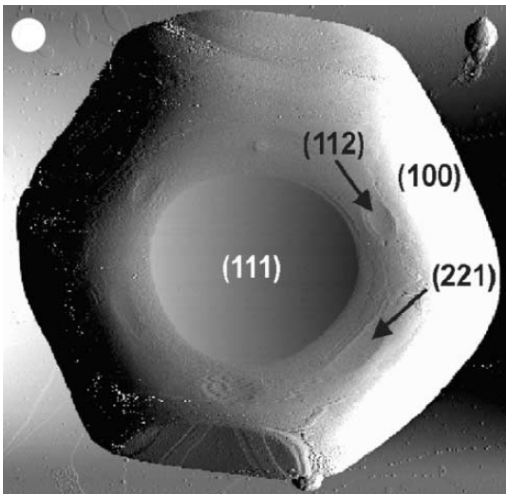

Figure 2.8: A photograph of a (truncated) crystallite[15], showing the differently oriented surfaces.

Whether or not the simple TLK model describes $\gamma(\theta)$ accurately across a large range of θ is a valid point of criticism. This is a good moment to utilize the experimental results regarding equilibrium shapes of crystallites; such a crystallite is shown in Figure 2.8. These experimental data[15–20] are very useful for evaluating the anisotropy of the surface free energy, which determines the equilibrium shape [9]. The equilibrium shape is determined by the Wulff construction, which can be derived from the Wulff plot. Starting from an experimental shape, one can trace back to the Wulff plot. Sadly, such experiments are extremely material dependent – as the crystallites are grown on a substrate – and there is no self-consistent data set available for all the elements.

It is possible however, to use the results of Bombis[15] for Pb to evaluate whether Equation 2.5 renders satisfactory results. In Figures 2.9 and 2.10, a very similar behavior is observed. The biggest discrepancies are caused by the differences in the energies for the low-index directions, i.e. the accuracy of the DFT result[10]. This comparison is a convincing argument in favor of using the TLK model to obtain $\gamma(\theta)$.

[9] Quite recently – in 2002 and 2004 – there has even been an attempt[15] [16] to determine the absolute surface free energy of the researched metals, although this was only moderately successful.

[10] It must be emphasized this is for a crystallite at $296K - 473K$. As the planar density of the atoms at a surface is dependent on the surface orientation, the free energy contribution from the entropy is dependent on this orientation. This is yet another reason why quantitatively comparing the crystallite data with DFT calculations is troublesome.

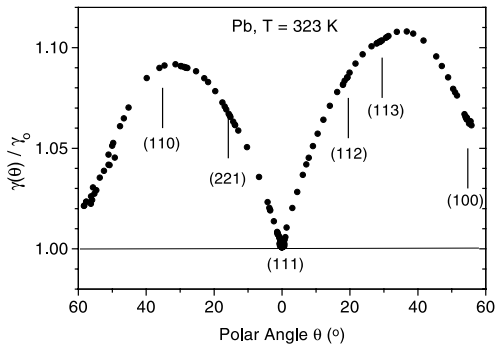

Figure 2.9: The results presented by Bombis[15] for $\gamma(\theta)$ of Pb in the {110} plane.

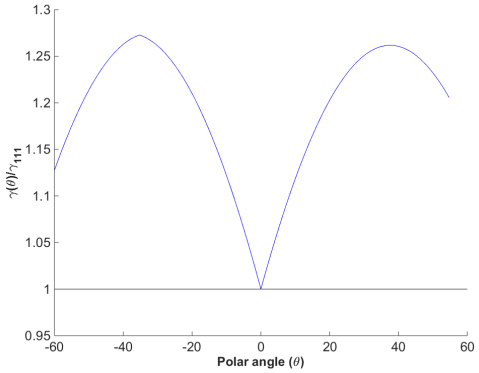

Figure 2.10: Calculated $\gamma(\theta)$ in the {110} plane based on ab initio simulations in this work.

When evaluating the above derivation from γ_{LV} at T_m to γ_{SV} at $0K$ there are a couple of sources of errors. Using the same ratio $\alpha = \gamma_{SL}/\gamma_{SV}$ for all materials ignores the material dependence. This simplification results in a $\pm 10\%$ error for $\gamma_{SV}(T_m)$, an error estimate derived from the spread in the ratio $\frac{\gamma_S V}{\gamma_S L}$ put forward by different authors. When extrapolating to $0K$, both the magnitude and the ranges for the contributions to the entropy were chosen independently of the material. The estimates used entail a possible error of up to $\pm 50\%$ on the thermal correction term. It must be emphasized that the choices made in the derivation to simplify the process were perceived to be good averages across all materials. Hence one would expect the method to be overall quite accurate, although material dependent variations are described with limited precision ($\pm 10\%$). The absence of large systematic deviations is of the utmost importance for statistical comparison with ab initio data. Although the assumption is made that Tyson and Miller are correct *on average* and the Wulff plots that are make describe their results, it should not be forgotten these might be sources of systematic deviation.

2.2 Work Function

The Work Function is the difference in energy between the Fermi level of the solid and a point outside the solid, sufficiently far removed from its surface so that no interaction with the surface is present. In contrast to measuring surface free energies, a variety of reliable methods exist to measure the work function Φ of a surface. In essence all experiments consist of extracting electrons from a surface – either by thermal excitation (thermionic emission), photoexcitation (photoelectric effect) or an electric field (FERP, CPD) – and measuring the resulting electron flux. However, the presence of defects and adsorbed impurities is the main source of inaccuracy, not the specifics of the experimental set-up. Therefore it is not necessary to make a distinction as to how the work function is obtained, since all methods yield – roughly – equivalent precision.

The work by Michaelson[21], published in 1977, still stands as the most prevalent reference for work functions. The author reviewed available experimental data and selected preferred values for a large number of elements at low-index orientations or polycrystalline samples. The experimental data that was selected has in most cases survived the test of time, but little can be said about their precision in general. It is certainly not the purpose to try and improve upon the choices of a seasoned experimentalist who is familiar with the methods of work function measurement and sample preparation difficulties. It is important however, to

have some knowledge of the size and nature of the errors involved, if a sound statistical comparison is to be performed with calculated work functions. According to Michaelson, a general error estimate of the error is $0.1eV$ to $0.2eV$. Further on it will be clear that this is an optimistic estimate for a lot of materials. The elements for which experimental data are available are represented in Figure 2.11.

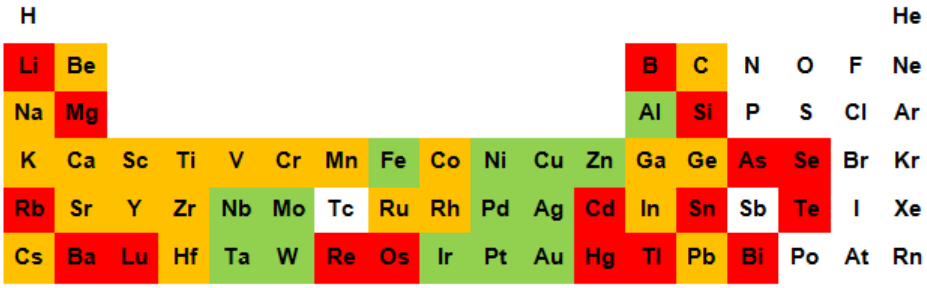

Figure 2.11: Elements for which a work function has been determined according to Michaelson. Color code: green elements have anisotropic data, yellow is for polycrystalline samples and an element in red has only unreliable data

A much more expansive effort was made by Kawano[22] in 2008 to evaluate the plethora of experimental data. Like Michaelson, he eventually selected a preferred value, but in the process he also made a full compendium of the work functions he used from literature. When scanning this large data set it becomes apparent just how large the spread can be on the work function of a – simple – surface. For most materials evaluated by Kawano, the experimental data spreads across an interval of $0.3eV$ to $0.6eV$. This large variation indicates a substantially lower precision compared to the $0.2eV$ according to Michaelson. On the other hand, for some surfaces the deviations are markedly smaller, which means comparing the experimental data should be done in a weighted manner. The specifics of this weighted comparison will be explained in section 5.1. Unfortunately only a select few elements have a large number of reliable work function data, which limits the number of materials Kawano has covered in his review compared to Michaelson's. Although it does add to the Michaelson data set due to the more recent date of publication, its main contribution lies in the quantitative information on the work function errors. In the review by Kawano, temperature dependence of the work function was also researched. The temperature coefficient for the work function was always small (10^{-6} to $10^{-4}\frac{eV}{K}$). Because the temperature dependence is multiple orders of magnitude smaller than the typical experimental precision, it was not taken into account in this work.

Many elements only have a work function for polycrystalline samples. Just as was the case for the surface energy comparison, a transformation from the anisotropic work function calculations will be needed to match the isotropic data. What is obtained exactly when the work function of a polycrystalline sample is measured? Without delving too deeply into the specifics of the different experimental methods, a short explanation of the set-up is in order. The well-known photoelectric experiment can serve as an illustrative representation of a typical experiment (Figure 2.12). Most often the frequency of the incident light on the surface of which one wishes to obtain the work function is tuned to be near the threshold. This means the facets of the sample which have a higher work function will not contribute, as the photon energy is insufficient to excite the electrons from these surfaces. As most experimental methods scan a sizable area of the sample – multiple grains with different orientations – they actually measure the facets with the lowest work function (or other facets with a work function very near to this lower bound). This conclusion is not only plausible, it was actually confirmed in a review by Helandar[23].

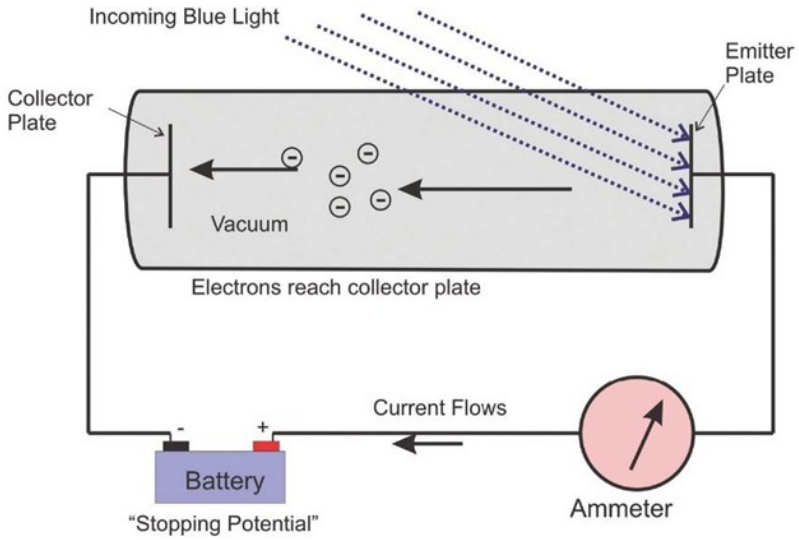

Figure 2.12: The schematics of a photoelectric experiment[24]. The stopping potential is determined by the frequency of the light and the work function of the emitter plate material.

The question now remaining is: what does the surface topology of the experimental samples look like? Which surface orientations are present, are there any structural defects – often lowering the measured work function – or adsorbed impurities – most likely rendering a higher value? It is impossible to deduce the sample topology of all the polycrystalline work functions that will be used, lacking information about the actual samples. It is possible however, to compare polycrystalline results with anisotropic data thanks to the Kawano review, which sheds light on the topology of a general polycrystallince surface. The elements for which both isotropic and anistropic data are available – there are 14 of them – show very little difference between the lowest anistropic work function and the polycrystalline one, confirming the above reasoning and the review by Helander. The average offset is $0.09eV$ with a standard deviation of $0.2eV$ – the data are presented in Table 2.1. Compare this to the difference between the polycrystalline work functions and the average of the anisotropic data for each element, where the difference is $-0.17eV$ with a standard deviation of $0.15eV$. The lowest anistropic work functions clearly lie significantly closer to the polycrystalline experimental data. Moreover, the deviation is no larger for the offset than it is for a set of experimental data of a polycrystalline surface. It is clear one can safely proceed comparing the lowest calculated work function for a certain element with the polycrystalline experimental work function.

There is now a sound procedure to formulate work functions and their errors. As the effort by the experienced experimental reviewers can not be ignored, their selected values will be used. The error on an element reviewed by Kawano (these elements are highlighted in Figure 2.13) will be determined by the spread on the available data. For all other elements, a good standard error value is $0.32eV$. This was deemed to be a "safe" estimate based on spreads for polycrystalline work functions in the Kawano data set. All experimental data and errors used in this thesis work can be found in Appendix A.

Material	Φ_{poly} (eV)	Φ_{low} (eV)	Δ_{poly}^{low} (eV)	$\Phi_{average}$ (eV)	$\Delta_{poly}^{average}$ (eV)
Ni	4.87	4.64	0.23	5.05	-0.18
Rh	4.9	4.77	0.13	5.19	-0.29
Ir	5.27	5.42	-0.15	5.64	-0.37
Pd	5.24	5.08	0.16	5.41	-0.17
Pt	5.27	5.61	-0.34	5.76	-0.49
Cu	4.51	4.48	0.03	4.65	-0.14
Ag	4.36	4.16	0.20	4.41	-0.05
Au	5.31	5.29	0.02	5.34	-0.03
Al	4.23	4.21	0.02	4.28	-0.05
Nb	4.02	3.86	0.16	4.21	-0.19
W	4.55	4.38	0.17	4.75	-0.20
Ta	4.25	4.0	0.25	4.33	-0.08
Mo	4.6	4.09	0.51	4.48	0.12
Fe-α	4.66	4.59	0.07	4.86	-0.20
Si	4.6	4.71	-0.11	4.78	-0.18
Average Δ			0.09		-0.17
Deviation on Δ			0.20		0.15

Table 2.1: Comparison of the polycrystalline work function Φ_{poly} with the lowest anisotropic work function Φ_{low} and the average of the anisotropic work function $\Phi_{average}$.

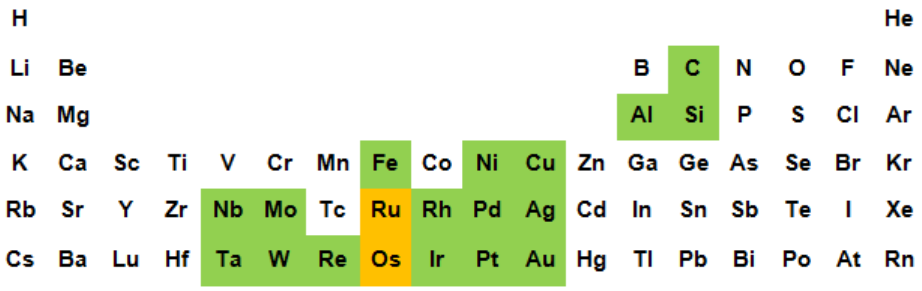

Figure 2.13: Elements for which Kawano reviewed the work function data. Color code: green elements have anisotropic data and yellow is for polycrystalline samples.

Chapter 3

Modeling a surface

In this section the aim is to provide a complete overview of how a surface is modeled and how the work function and surface energy are derived – from theoretical background to practical implementation. It is obviously not the goal of this chapter to present a rigorous background of Density-Functional Theory (DFT). The main purpose is to present a succinct theoretical framework from which the reader can understand the key computational properties that influence a DFT calculation for surfaces. A large part of the structure and concepts in this section are based on the short introduction into DFT by Cottenier[25]. To end this chapter, a short introduction to DFT benchmarking is presented with an emphasis on errors on surface properties.

3.1 Density-Functional Theory

3.1.1 The many-body wave function

The bare nature of a solid is a collection of nuclei and electrons. Within a spin-independent description, all information on this system is contained within the wave function $\Psi(\vec{R}_1, \ldots, \vec{R}_N, \vec{r}_1, \ldots, \vec{r}_n)$ with $\vec{R}_i$ and $\vec{r}_j$ the place coordinates for the N nuclei and n electrons respectively. According to quantum mechanics, the time-independent many-body wave function can be found by solving the stationary Schrödinger equation:

$$\left\{ -\frac{\hbar^2}{2} \sum_i^N \frac{\nabla^2_{\vec{R}_i}}{M_i} - \frac{\hbar^2}{2} \sum_j^n \frac{\nabla^2_{\vec{r}_j}}{m_e} - \frac{1}{4\pi\epsilon_0} \sum_{i,j}^{N,n} \frac{e^2 Z_i}{|\vec{R}_i - \vec{r}_j|} + \frac{1}{8\pi\epsilon_0} \sum_{i\neq j}^{N,N} \frac{e^2 Z_i Z_j}{|\vec{R}_i - \vec{R}_j|} + \frac{1}{8\pi\epsilon_0} \sum_{i\neq j}^{n,n} \frac{e^2}{|\vec{r}_i - \vec{r}_j|} \right\} \Psi = E\Psi \quad (3.1)$$

Solving this differential equation is hampered in large part by the two-body operators of the electrostatic interaction. If there would only be one-body operators present, one could simply decouple equation 3.1 to single-particle differential equations.

A first simplification is performed by applying the Born-Oppenheimer approximation. Because the mass of the nuclei is of the order of 10^3 times heavier than the electron mass, the nuclear positions are considered static in the system. Clamping these nuclei to fixed positions neglects the $\nabla^2_{\vec{R}_i}$ terms and the positions $\vec{R}_i$ become parameters in the differential equation. The two-body operators for the interaction of the nuclei with themselves and the electrons are now simplified and they determine the external potential for the n-electron

many-body system.

$$\hat{V}_{ext}(\vec{r}_1,\ldots,\vec{r}_n) = -\frac{1}{4\pi\epsilon_0}\sum_{i,j}^{N,n}\frac{e^2 Z_i}{|\vec{R}_i-\vec{r}_j|} + \frac{1}{8\pi\epsilon_0}\sum_{i\neq j}^{N,N}\frac{e^2 Z_i Z_j}{|\vec{R}_i-\vec{R}_j|} \tag{3.2}$$

The remaining part of the Hamiltonian only depends on the number of electrons n. One can write formally:

$$\hat{H} = \underbrace{\hat{T}+\hat{V}}_{universal} + \hat{V}_{ext} \tag{3.3}$$

3.1.2 Hohenberg-Kohn theorems

The only term still obstructing a straightforward solution is the electron-electron repulsion. To cope with this particular problem, a different approach to the Schrödinger equation is taken in DFT.

The postulates of quantum mechanics state that every observable quantity can be measured as the eigenvalue of a corresponding operator $\hat{O}$. The expectation value of the observable quantity for the system is thus determined by $\langle\Psi|\hat{O}|\Psi\rangle$. The wave function is not the only fundamental quantum mechanical variable, as the first Hohenberg-Kohn Theorem states[26]:

"There is a one-to-one correspondence between the ground-state density $\rho(\vec{r})$ of a many-electron system (atom, molecule, solid) and the external potential V_{ext}."

As the density is defined as the chance of finding an electron at a location:

$$\rho(\vec{r}) = \langle\Psi(\vec{r}_1,\ldots,\vec{r}_n)\Big|\sum_{i=1}^{n}\delta(\vec{r}_i-\vec{r})\Big|\Psi(\vec{r}_1,\ldots,\vec{r}_n)\rangle \tag{3.4}$$

this theorem entails the existence of a corresponding functional $O[\rho]$ for every operator $\hat{O}$ with:

$$\langle\Psi|\hat{O}|\Psi\rangle \equiv O[\rho] \tag{3.5}$$

which means the ground-state density of an n-electron system contains as much information as its many-body wave function. This is also true for the total ground-state energy of the system $E = \langle\Psi|\hat{H}|\Psi\rangle = E[\rho]$, which also meets the second Hohenberg-Kohn theorem[26]:

The ground-state total energy functional $E[\rho]$ is of the form:

$$\begin{aligned}\langle\Psi|\hat{H}|\Psi\rangle &= \langle\Psi|\hat{T}+\hat{V}|\Psi\rangle + \langle\Psi|\hat{V}_{ext}|\Psi\rangle \\ &= F_{HK}[\rho] + V_{ext}[\rho] = F_{HK}[\rho] + \int\rho(\vec{r})V_{ext}(\vec{r})d\vec{r} \\ &= E_{V_{ext}}[\rho]\end{aligned} \tag{3.6}$$

Where the Hohenberg-Kohn density-functional F_{HK} is universal for any many-electron system with a given number of electrons n, and the energy functional $E_{V_{ext}}[\rho]$ reaches its minimum for the ground-state density.

This last point of the Hohenberg-Kohn theorems – the variational access to $\rho(r)$ via the energy functional – provides us with a formal solution for the many-body equation. Although the Hohenberg-Kohn density-functional F_{HK} is a universal functional applicable to any many-electron system, its real form is not explicitly known. At this point DFT is still not a practical tool to solve the many-body problem.

3.1.3 The Kohn-Sham equations

Kohn and Sham proposed[27] to decouple the differential equation by introducing a single-particle Hamiltonian $\hat{H}_{KS}$. A full anti-symmetrical product (to meet the Pauli-exclusion principle) of the derived single-particle orbitals can subsequently be constructed to obtain the many-electron wave function. The density then becomes:

$$\rho(\vec{r}) = \sum_{i=1}^{n} \phi_i(\vec{r})^* \phi_i(\vec{r}) \tag{3.7}$$

With ϕ_i the n lowest energy solutions of:

$$\hat{H}_{KS}\phi_i = \epsilon_i \phi_i \tag{3.8}$$

One can compose the Kohn-Sham Hamiltonian in a way which is physically quite insightful:

$$\hat{H}_{KS} = \hat{T}_0 + \hat{V}_H + \hat{V}_{xc} + \hat{V}_{ext} \tag{3.9}$$

where $\hat{T}_0$ is the non-interacting single-particle kinetic energy:

$$\hat{T}_0 = -\frac{\hbar^2}{2m_e}\nabla_i^2 \tag{3.10}$$

$\hat{V}_H$ the Hartree potential energy:

$$\hat{V}_H = \frac{e^2}{4\pi\epsilon_0}\int \frac{\rho(\vec{r'})}{|\vec{r} - \vec{r'}|} d\vec{r'} \tag{3.11}$$

and $\hat{V}_{ext}$ the interaction with the nuclei. The remaining contributions to the total energy are incorporated in the exchange-correlation functional V_{xc} which should incorporate all pairwise interactions not included in the mean-field approach – $\rho(\vec{r})$ being this mean field.

The latter functional is of course the Achilles' heel of Kohn-Sham theory, as its exact universal form is not explicitly known. The approximations to V_{xc}[1] utilized in DFT will be the main source of error in the calculations – the Kohn-Sham scheme would be exact if the universal functional V_{xc} was known explicitly. However, DFT calculations with even the simplest of approximations for the exchange-correlation energy

[1] Both E_{xc} and V_{xc} refer to the exchange-correlation contribution to the energy.

perform remarkably well within a lot of physical systems.

The decoupling of the differential equation is thus performed by replacing the electron-electron interaction with an electron-mean field interaction. The fact that this mean field is produced by the results of the decoupled equations themselves is not an obstruction. One can tackle this by starting from an initially guessed density $\rho_0(\vec{r})$ and calculating a new one. This iterative procedure is continued until the newly calculated density matches the old one. At this point the calculation is converged – within a certain precision requirement – and the correct density is found. Most commonly the total ground-state energy is used as a convergence criterion. A flow chart of the self-consistent field cycle can be seen in Figure 3.1.

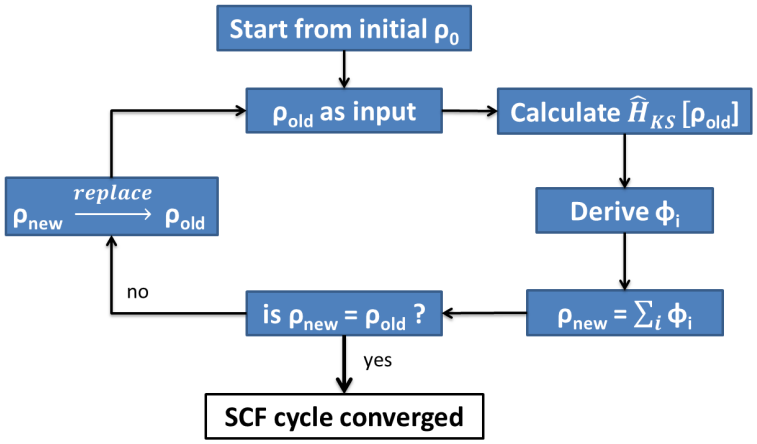

Figure 3.1: Schematic overview of a self-consistent field (scf) cycle. No criterion for comparing ρ_{old} and ρ_{new} is explicitly mentioned here.

It has to be stressed these orbitals ϕ_i have no physical meaning. They are only results of an assisting independent-particle model. In a many-electron problem the electrons are correlated and only the full all-electron wave function should be interpreted as a physical result of the self-consistent field cycle.

3.1.4 Explicit forms for E_{xc}

In a first approximation $E_{xc}[\rho]$ is only dependent on the local density – hence it is called the local density approximation (LDA)[28].

$$E_{xc}^{LDA}[\rho] = \int \rho(\vec{r})\epsilon_{xc}(\rho(\vec{r}))d\vec{r} \tag{3.12}$$

No analytic expression is known for $\epsilon_{xc}(\rho(\vec{r}))$ but the lower and upper bound are known and numerical solutions can be obtained by performing Monte Carlo simulations and meeting the limiting behavior.

The success of this simple form for $E_{xc}[\rho]$ lies in the fact that one is usually interested in some difference of calculated quantities: energies of formation, adsorption energies, surface energies, vacancy energies, work

functions, etc. For all such quantities a large cancellation of the error made by the approximate functional takes place. For this reason LDA calculations have been included in this thesis.

A more accurate approach is to incorporate the gradient of the density $\nabla\rho(\vec{r})$ in the exchange-correlation functional. This family of functionals are called Generalized Gradient Approximation (GGA) functionals:

$$E_{xc}^{GGA}[\rho] = -\int (C_x^{LDA} + f(s(\vec{r})))\rho^{4/3}(\vec{r})d\vec{r} \tag{3.13}$$

Where C_x^{LDA} is the constant to obtain the LDA exchange contribution and $s(\vec{r}) = \frac{|\nabla(\rho(\vec{r}))|}{\rho^{4/3}(\vec{r})}$ a dimensionless gradient. The gradient can be included in a variety of ways, through the choice made for the functional $f(s(\vec{r}))$. Some approaches, like B88[29] for exchange, LYP[30] for correlation or the P86 functional[31] introduce a fitting parameter for the function f. This in fact turns DFT into a semi-empirical method. Others, like PW91[32] or PBE[33,34] try to obey the exact behavior of the correlation functional. Especially PBE has become very popular for condensed matter because of its wide applicability.

Until now, the electron spin has been ignored. For non-magnetic systems this is not a problem, since the spin-up and spin-down populations are equivalent. If one wishes to incorporate magnetism however, the electron density will have to be separated into a spin-up and spin-down density and the respective interactions accounted for in the exchange-correlation potential.

Because the PBE functional incorporates the gradient of the density, one might expect it to outperform the LDA functional for surfaces, as the electron density drops to zero quite rapidly in the vacuum. Although this thesis restricts itself to these two functionals, nowadays it has become computationally viable to perform DFT calculations for surfaces on a higher level of theory. In comparisons with literature for some specific elements, these hybrid GGA's will show up.

3.2 Computational implementation

The Kohn-Sham equations provide us with a set of decoupled eigenvalue problems. However, their solutions are formally continuous functions. Within the finite memory of any electronic device used for computation, these functions need to be represented by a set of finite numbers parametrizing a function of prescribed form.

3.2.1 Basis sets

The most common solution methods represent the Kohn-Sham single-particle orbitals $|\phi_i\rangle$ by a linear combination of a set of basis functions $\{\left|\phi_1^b\right\rangle, \ldots, \left|\phi_B^b\right\rangle\}$:

$$|\phi_i\rangle = \sum_{j=1}^{B} c_j^i \left|\phi_j^b\right\rangle \tag{3.14}$$

Inserting this expansion into the Kohn-Sham equation[25] yields:

$$\hat{H}_{KS} \sum_{j=1}^{B} c_j^i \left|\phi_j^b\right\rangle = \epsilon_i \sum_{j=1}^{B} c_j^i \left|\phi_j^b\right\rangle \tag{3.15}$$

Scalar multiplication with any ϕ_m^b results in B equations:

$$\sum_{j=1}^{B} c_j^i \left\langle\phi_m^b\right| \hat{H}_{KS} \left|\phi_j^b\right\rangle = \epsilon_i \sum_{j=1}^{B} c_j^i \left\langle\phi_m^b\middle|\phi_j^b\right\rangle \tag{3.16}$$

which can be contracted into matrix notation:

$$\begin{bmatrix} \cdots & \cdots & \cdots \\ \vdots & \left\langle\phi_m^b\right| \hat{H}_{KS} \left|\phi_j^b\right\rangle & \vdots \\ \cdots & \cdots & \cdots \end{bmatrix} \begin{bmatrix} c_1 \\ \vdots \\ c_B \end{bmatrix} = \epsilon \begin{bmatrix} \cdots & \cdots & \cdots \\ \vdots & \left\langle\phi_m^b\middle|\phi_j^b\right\rangle & \vdots \\ \cdots & \cdots & \cdots \end{bmatrix} \begin{bmatrix} c_1 \\ \vdots \\ c_B \end{bmatrix} \tag{3.17}$$

this is a general eigenvalue equation, where the index i is dropped, stressing the fact B eigenvalues for the energy and eigenvectors for the single-particle wave functions are obtained via one algebraic eigenvalue problem. If the basis functions ϕ^b are orthonormal, equation 3.17 reduces to a normal eigenvalue problem.

Naturally, the choice of basis set – both the number and type of functions – will greatly influence the accuracy of the expansion and, eventually, the obtained solutions. Including more functions into the basis set will require a higher computational cost, as the matrix diagonalization becomes more demanding. Three principle features of a basis set are its *efficiency*, a possible *bias* and its *flexibility*.

One idea for a basis set comes from quantum chemistry, which uses a linear combination of atomic orbitals (LCAO) to obtain single-particle wave functions. By choosing hydrogen-like wave functions centered around the atomic positions, a basis set of which the functions already approximate the final solutions very well is obtained. In this way, the basis set does not need to be large to represent the solutions accurately – one refers to it as a very *efficient* basis.

The use of atomic orbitals becomes less successful when the electron density deviates strongly from an atom-in-molecule behaviour. This is particularly true for metals, where electrons in high-energy orbitals are delocalized from atomic positions. The orbitals around the Fermi level will however determine most interesting chemical and physical properties (band gap, conductivity, reactivity and angular properties). Incorporating more atomic basis functions does not guarantee an improved description of the higher orbitals, as these are not necessarily well-matched by atomic orbitals – they form a *biased* set . For many solids a more *flexible* basis set is desired, performing equally accurately for a variety of atomic species and configurations.

An approach that is less biased is to describe the Kohn-Sham orbitals as a linear combination of free-particle wave functions:

$$\phi(\vec{r}) = \sum_{\vec{k}} c_{\vec{k}} e^{i\vec{k}\cdot\vec{r}} \tag{3.18}$$

Where the sum is formally taken over all vectors $\vec{k} \in \mathbb{R}$ in reciprocal space. At this point the basis set is impossibly large. The symmetry of the periodic crystalline solid – represented by the crystal lattice – greatly simplifies the problem however. As the Bloch theorem states:

Any eigenfunction $\phi^n_{\vec{k}}(\vec{r})$ of the Hamiltonian in a crystal can be written as a product of a function $u^n_{\vec{k}}(\vec{r})$ that has the periodicity of the lattice, and a plane wave $e^{i\vec{k}\cdot\vec{r}}$ with $\vec{k}$ any vector in the first Brillouin zone:

$$\phi^n_{\vec{k}}(\vec{r}) = u^n_{\vec{k}}(\vec{r}) e^{i\vec{k}\cdot\vec{r}} \tag{3.19}$$

Because of the periodicity of the function $u^n_{\vec{k}}(\vec{r})$ one can rewrite equation 3.18 as:

$$\phi^n_{\vec{k}}(\vec{r}) = \sum_{\vec{K}} c^{n,\vec{k}}_{\vec{K}} e^{i\vec{k}\cdot\vec{r}} \tag{3.20}$$

where the sum is taken over all reciprocal lattice points $\vec{K}$. The crystal impulse $\vec{k}$ is an eigenvalue of the Schrödinger equation of the crystalline sold. If one such eigenvalue $\vec{k}$ is regarder, the expansion (Equation 3.20) is still over an infinite set, but it is countable. Moreover, truncating this set can be done on basis of physical grounds. If one imposes a maximum value K_{max}, a maximum for the free-electron energy is set – and thus the oscillation frequency of the density in space. Therefore it is usually called the cut-off energy:

$$E_{cut} = \frac{\hbar^2 K^2_{max}}{2m_e} \tag{3.21}$$

This means the sharply oscillating behavior of the density near the atomic nuclei is the determining factor for the number of reciprocal points $\vec{K}$ needed in the basis set.

From the matrix representation 3.17 and the fact plane waves are orthogonal, the solution is now obtained via a simple eigenvalue equation. For $2N$ electrons in a unit cell, the N lowest band indexes are the bound solutions. The only choice left to be made is for which vectors $\vec{k}$ in the first Brillouin zone the Kohn-Sham equations should be solved. The discrete number of values $\vec{k}$ should be sufficient to accurately numerically evaluate the total energy integral in equation 3.22, where the sum is taken over all bands and Ω_{BZ} is the volume of the first Brillouin zone.

$$E_{tot} = \sum_{n=1}^{N} \frac{1}{\Omega_{BZ}} \int_{\Omega_{BZ}} \epsilon_n(\vec{k}) d\vec{k} \tag{3.22}$$

3.2.2 Pseudopotentials and augmented methods

In the previous section it was concluded a plane-wave basis can be constructed for every periodic potential, by choosing a cut-off energy E_{cut} and a set of $\vec{k}$-points in the first Brillouin zone. Sadly, this still leaves us with an unmanageable basis set size. Even for the valence electron density, the internodal distance near the nucleus is too small for most elements , requiring a cut-off energy that results in basis sets with more than millions of functions. Diagonalizing such a large matrix is not feasible.

There are several methods to try and reduce the required number of plane waves in the basis set. The first stems from the chemical picture of molecules and solids. The behavior of the elctrons near the nucleus is of little significance for the interatomic behavior. Yet it is near the nucleus that short-range oscillations in the density are encountered, imposing the need for a very large basis set. A simple strategy is to replace the external potential near the atomic positions. Such an adaptation should – if done correctly – leave the properties of the compound largely unaltered. There is however no infallible procedure for generating such a *pseudopotential* (PP). Its validity can only be shown by producing accurate results.

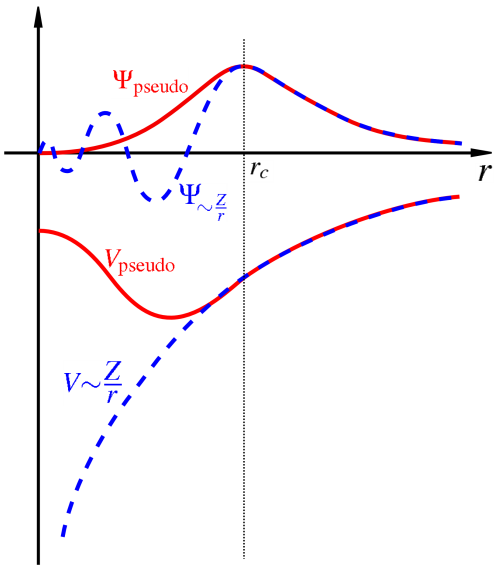

Figure 3.2: A conceptual graphic showing the smoothing of the wave function by adapting the potential near the atomic core.[35]

A more general approach is taken by Blöchl, called the PAW method[36,37]. The ansatz is to construct an operator $\hat{\mathcal{T}}$ which defines a transformation between full wave functions $|\phi\rangle$ and pseudo-wave functions $|\tilde{\phi}\rangle$. The latter are smooth functions in the regions of the atoms Ω_R – augmentation spheres – and hence require only a fraction of the basis functions needed to describe the actual Kohn-Sham orbitals $|\phi\rangle$. They can moreover be expanded in a more efficient basis of so-called partial waves. As the pseudo-wave functions match the original ones outside the augmentation spheres, $\hat{\mathcal{T}}$ may be written as

$$|\phi\rangle = \hat{\mathcal{T}}\,|\tilde{\phi}\rangle = \sum_R \left(1 + \hat{\mathcal{T}}_R\right)|\tilde{\phi}\rangle \tag{3.23}$$

Where $\hat{\mathcal{T}}_R$ is the zero-operator outside the augmentation spheres.

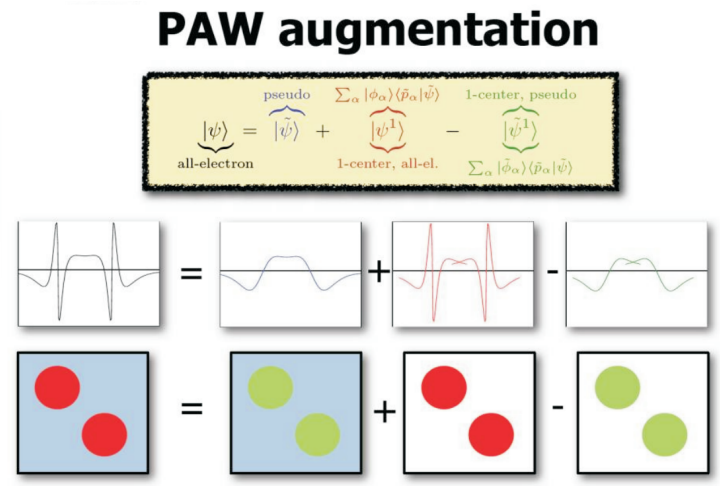

Figure 3.3: A graphic illustrating the point of the operator $\hat{\mathcal{T}}_r$. Slide by P.Blöchl

Again, the entire point of the method is to smooth the wave functions close to the atoms. This is graphically depicted in Figure 3.3. By constructing an operator that defines the transformation between full and pseudized wavefunctions there is now a method to efficiently perform the calculations – saving time and memory – while still having access to the full Kohn-Sham orbitals.

The combination of the PAW method with plane waves and a frozen core ensures a good degree of accuracy while providing the necessary quickness[38], desirable because of the large number of calculations required to obtain precise work functions and surface energies for all low-index surfaces across the entire periodic table. The Vienna ab initio package (VASP) developed by Kresse et al.[39–42] will be used.

3.2.3 Mixing and smearing

During the explanation of the process described in Figure 3.1 the speed of convergence was not discussed. Indeed it is not necessarily guaranteed that the density obtained from solving the Kohn-Sham equations will yield an *improved* density. Because of this, the old and new density will be mixed into a density for the next iteration in the self-consistent field cycle. This mixing process greatly reduces the time needed to convergence the calculation. There are several mixing schemes available[43], but for all calculations with VASP the default Pulay[44,45] scheme will be used.

Another problem greatly hampering convergence occurs in metals. In a metal the highest occupied orbital crosses the Fermi energy at some $\vec{k}$ in the first Brillouin zone. This means equation 3.22 in general becomes:

$$E_{tot} = \sum_{n=1}^{N} \frac{1}{\Omega_{BZ}} \int_{\Omega_{BZ}} \epsilon_n(\vec{k}) \Theta(\epsilon_F - \epsilon_n(\vec{k})) d\vec{k} \tag{3.24}$$

with Θ the temperature-dependent Fermi-Dirac distribution, determining the energetic distribution of the electrons. As no temperature is included in DFT – indeed only the ground state density is meaningful – Θ is a step function. Approximating such a step function in reciprocal space requires a high density of $\vec{k}$-points in the first Brillouin zone, while the exact description of the step is not necessary for accurate energies. For successive steps in the scf cycle, the $\vec{k}$-point where the valence band crosses the Fermi energy might move around in between sampled $\vec{k}$-points. This abrupt change in occupation of $\vec{k}$-points hampers the convergence greatly. To smooth out this process, one can approximate the step function by a smooth function – introducing partial occupations. There are a couple of choices for such a smooth function. A physical finite-temperature approach can be introduced, imposing a – very low – temperature and using the Fermi-Dirac distribution. More successful approximations of the step functions can be obtained with Gaussian functions or Hermite polynomials (Figure 3.5).

Another way to tackle the step function is by performing the integration in equation 3.24 somewhat more intricately. By taking a weighted sum of a number of nearby $\vec{k}$-points, each discrete part of the integral is approximated more accurately. This is called the tetrahedron method.

Two general rules are to be obeyed with respect to the use of different smearing schemes. For all elements, the tetrahedron smearing by Blöchl[46] is considered as the most accurate method for total energies. On the other hand, to obtain accurate forces for metals – important for optimizing the atomic positions for minimal energy – the Methfessel-Paxton[47] scheme is required[43], as the Blöchl scheme is not variational with respect to the partial occupations. The finite temperature parameter σ, which determines the width of the approximating function, should be small enough not to influence the result of the calculation yet large enough to aid the numerical convergence.

3.3 Using DFT for a surface simulation

In section 3.2.1 the use of a plane-wave basis was applied to the specific case of a crystalline solid. The Bloch theorem however, applies to any periodic potential even if this periodicity is entirely manufactured. A single isolated molecule may be equally accurately modeled, provided the size of the – manufactured – unit cell is large enough as to avoid interaction between cells. In such cases, the integral in equation 3.22 may be accurately calculated by using only one $\vec{k}$-point in reciprocal space for a non-periodic direction – thus recovering some of the additional computation time caused by using a larger unit cell.

3.3.1 The unit cell

When using a three-dimensional periodic code, modeling a surface is done by creating slabs. These slabs are created by stacking a number of layers corresponding to the bulk geometry and adding a significant amount of vacuum in between slabs. The way the layers are stacked is determined by the orientation of the surface – most often expressed by the direction perpendicular to the surface – and the bulk unit cell. The construction and simplification of the slab unit cells was performed with aconvasp, a part of the aflow software package[48].

The translation symmetry entails the slabs are periodically repeated (Figure 3.4), but the periodicity along

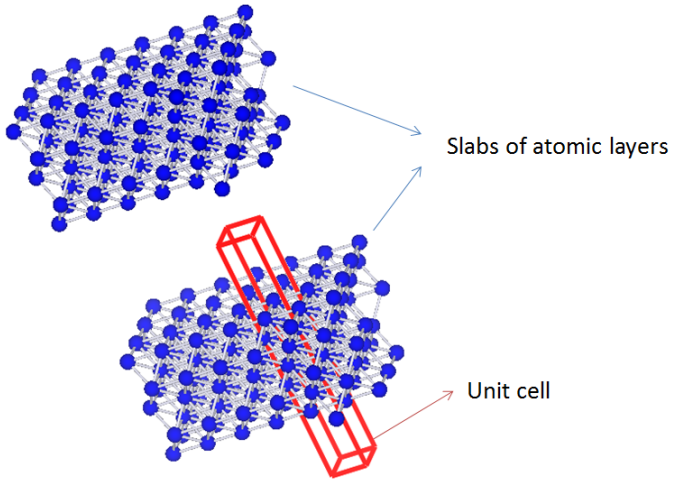

Figure 3.4: Slabs of atomic layers for modeling a <100> surface for a face-centered cubic (fcc) material.

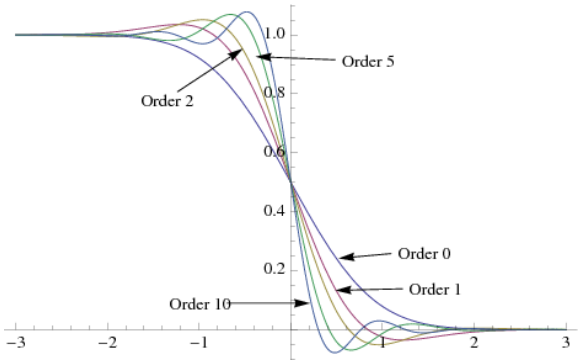

Figure 3.5: Different orders of approximating the step function with the Methfessel-Paxton method (using Hermite polynomials). The width of the distribution depends on the parameter σ[2]. [49]

the direction normal to the slabs is entirely non-physical. This should not matter, as the goal of the inserted vacuum space is to separate the slabs sufficiently to remove all interaction. In this manner one creates two surface layers per unit cell. For many common mono-atomic crystal structures and low-index directions – the unit cell contains one atom per bulk layer. The following sections therefore assumes one atom per layer in the unit cell. Any deviations are quite easily coped with however.

Special care should be taken to make sure one creates the *same* surface at both sides of the slab. In the general case, stoichiometry and equal terminations might even be irreconcilable. Since only the pure elements are simulated, most slabs will be very simple – the {100} surfaces and {111} slabs for the hcp and diamond structures respectively forming notable exceptions (see sections 4.4 and 4.5).

3.3.2 Geometric optimization

In practice, the slabs will be constructed – for most elements – starting from the bulk equilibrium geometries as calculated in the work of Lejaeghere et al.[4]. The simple slab obtained from stacking a number of bulk

[2]In the case of Fermi-Dirac smearing, σ is the finite temperature.

layers and inserting vacuum is of course not a correct representation of a surface. In reality, even for perfectly clean surfaces without, the atoms at the surface will relax into a different configuration. These altered geometries are divided into two classes: *surface relaxations* and *surface reconstructions* and are a consequence of the removal of neighboring atoms – causing *dangling bonds*. A relaxation is simply the alteration of the interlayer distance perpendicular to the slab plane. A reconstruction on the other hand, involves a displacement parallel to the slab surface – leading to the formation of new atomic bonds. significant reconstructions are found predominantly in surfaces of strongly covalent materials, whereas for metals or ionically bonded crystals a simple relaxation is the only adaptation of the geometry.

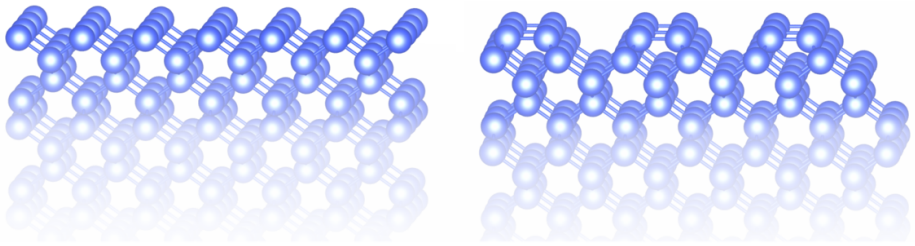

Figure 3.6: The difference between a Si {100} slab allowed to reconstruct (right) or limited to a simple relaxation (left)

Most DFT codes include several geometric optimization schemes, as does VASP. By calculating the Hessian (the partial derivatives of the energy $\frac{\partial^2 E}{\partial x_i \partial x_j}$) the alteration of the ionic positions to minimize the forces is obtained. Through adaptation of the geometry, a configuration is reached where the energy is minimized and the forces are zero – up to a certain precision.

It is not the objective to rigorously evaluate all possible reconstructions in this work, the focus is on adequately simulating surfaces to obtain accurate work functions and surface energies. It is of little interest to pursue a complicated reconstruction – the $(7 \times 7)\{111\}$ superstructure of Si for example[50] – when such an altered geometry makes little energetic difference[3]. As such, only the – fairly simple – 2×1 reconstructions of the diamond lattices (C, Si, Ge and Sn) were taken into account. Relaxations were always accounted for and the number of layers in a slab allowed to relax was always determined by a thorough test. The details of this testing will be discussed in the next chapter.

3.3.3 Surface Energy

The surface energy is the energy required to create a surface – usually expressed in $\frac{J}{m^2}$. This is exactly what has been done in the previous section by inserting vacuum into a supercell. The surface energy per surface atom follows quite simply from the calculations:

$$\sigma = \frac{E_{slab} - E_{bulk}}{2} \tag{3.25}$$

where E_{slab} is normalized to the number of atoms per layer and E_{bulk} normalized to the number of atoms in the bulk unit cell. The factor 2 accounts for there being two surfaces in the slab unit cell. Note the use of the

[3]This manifests itself in the experimental difficulty to even *obtain* this complicated reconstruction for Si.

symbol σ for surface energy pe atom. Throughout this work γ will be used for surface energy expressed in $\frac{J}{m^2}$ and σ when the units are $\frac{eV}{atom}$. This is to discern between the DFT result itself, where σ directly follows from the calculations, and the eventual macroscopic surface energy for comparison between elements and with experiment, where the surface area per atom has to be taken into account. In order to use equation 3.25 it is necessary to perform an additional calculation for the bulk material. This does not impose a significant additional cost, as a calculation of a simple unit cell with only a few atoms is quick work by today's standards.

The main problem with using equation 3.25 is comparing data from two different calculations. The slab and the bulk material have a different unit cell – and thus Brillouin zone – both in shape and number of atoms. Consequently the computational precision will be different – especially with respect to the meshing of the first Brillouin zone. A slab unit cell is so large in one dimension, the corresponding reciprocal direction only requires one point. Meshes in $\vec{k}$-space for surfaces are therefor planar and in this work all $\vec{k}$-meshes were indicated with only two indexes. There is another reason why choosing a planar mesh is beneficial to the slab model. As can be seen in Equation 3.20, this means the only part of the wave functions accounted for has the same periodicity as the slabs. This helps suppressing interaction between slabs.

Boettger highlighted this problem and proposed a solution[51]. The idea is fairly simple: adding a layer of bulk material to the slab will increase the energy E_{slab} by the bulk energy.

$$E_{bulk} = E^{N}_{slab} - E^{N-1}_{slab} \tag{3.26}$$

Where the superscript indicates the number of layers in the slab. The bulk energy is now derived from slab calculations and equation 3.25 should render a more accurate surface energy.

The main question surrounding the method proposed by Boettger – and indeed the entire slab model – is: how many layers should a slab contain? This can only be answered by increasing the slab thickness until the relevant quantities convergence – in this case: work function and surface energy. In the converged limit, one side of a slab should have no effect on the other end of the slab.

A more expansive approach was put forward by Fiorentini and Methfessel[52]. Instead of only relying on the difference in energy between two slabs, it is possible to calculate the energy for a number of slabs of different thickness. The bulk energy is subsequently derived as the slope of the linear fit to these energies. Once more this procedure begs the question: what thickness should the slabs be? Furthermore the method by Fiorentini and Methfessel increases the computational cost substantially. Does the improved accuracy – if there is any – warrant the surplus of calculations to be performed?

The impact of the discrepancy between a bulk and surface calculation was evaluated by orienting the unit cell in different ways. This results in the Brillouin zone being sampled at different grid points. In Figure 3.7 it can be seen how the result becomes gradually independent of the orientation. As an example Al is shown, but the same convergent behavior can be observed for a number of tested materials ; in fact, Al was chosen because those calculations were markedly more dependent on the $\vec{k}$-point meshing (as a worse case scenario). The Boettger and Fiorentini & Methfessel methods for obtaining surface energies were proposed in 1994 and 1996 respectively. Although their concern for comparing computational results is certainly justified, by today's standards of computational capacity, using a high $\vec{k}$-point density for bulk simulations is

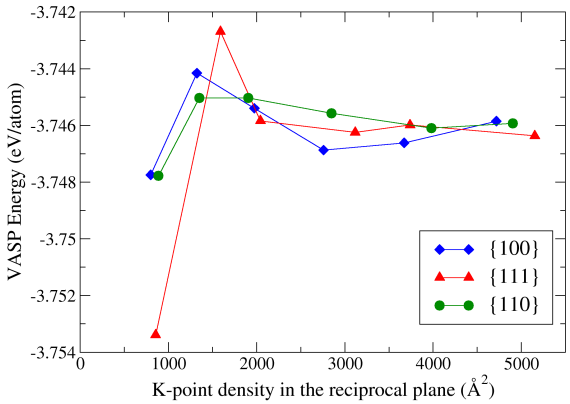

Figure 3.7: Different unit cell orientations – and thus reciprocal grids – for bulk aluminum. Denser meshing removes the dependence of the final result on this orientation.

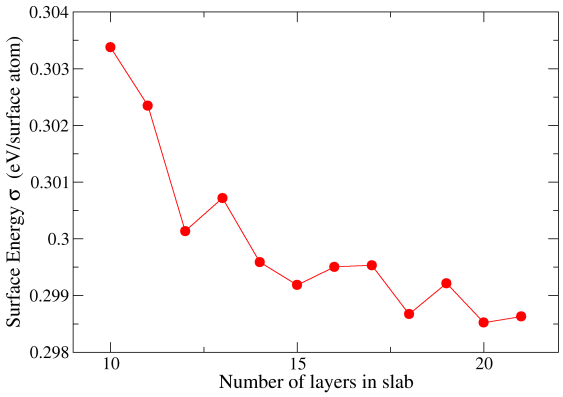

Figure 3.8: Evolution of the surface energy – obtained through a bulk reference energy – with respect to slab thickness for Mg {0001} slabs.

cheap and ensures a high precision.

If Figure 3.7 shows the problem of a "computational mismatch" is somewhat outdated, Figure 3.8 uncovers an inherent problem to the alternative methods. The variation in surface energy when adding a layer to the slab is quite unpredictable. There will, for example, be a discrepancy of $3meV$ between the bulk energy derived from the difference in energy of the 10-and 11-layer slab compared to the bulk energy derived from the difference in energy of the 11-and 12-layer slab. If one were to derive bulk energies in this way (Boettger), these variations will hamper the precision greatly resulting in bulk energies which could never improve upon a separate bulk calculation. If one would wish to apply a linear fit to the slab energies to derive the bulk energy (Fiorentini & Methfessel) one can see the influence of the region over which the fit is made. If in Figure 3.8 the fit is made between 10 and 15 layers, the slope will different from the situation where the fit is taken between 15 and 20 layers. Moreover, across a large range of slab thicknesses, there is no indication of a *constant* mismatch between the bulk and slab calculations. This was to be expected, as adding layers of bulk stabilizes the slab. It is intrinsically impossible to discern whether the evolution of the surface energy with increasing thickness is a convergence of the slab calculation – an improvement of the model – or a mismatch with the bulk energy – a computational imprecision.

In light of these observations, the best method for obtaining precise surface energies is believed to revolve around a bulk calculation with high precision. Today, this can be done with a minimal investment and ensures satisfactory precision. The approach can be summarized as "Make sure *each* calculation is of sufficient precision, converged up to a satisfactory level, and comparisons between calculations pose no problem".

As will be explained in the next chapter, some materials were thoroughly tested – serving as a guide for the entire periodic system. This included testing for slab thickness impact. From the results of these tests the Fiorentini & Methfessel bulk energy can be derived, allowing us to assess the impact of the differing methods. The bulk energy from the linear fit rarely differed more than $0.1\frac{meV}{atom}$ from the dedicated calculation.

3.3.4 Work Function

The work function is the *minimum* thermodynamic work needed to remove an electron from the bulk of a solid to the vacuum

$$\Phi = V_{VAC} - \epsilon_F \tag{3.27}$$

Here V_{VAC} is the local potential – which can derived from the calculated density $\rho(\vec{r})$ – at a point in space far away (on an atomic scale) from the material. An inspection of the local potential $V[\rho](\vec{r})$ is useful for determining where E_{VAC} should be taken. It should be stressed here there is – in the calculations – no actual removal of an electron, as is the case when experimentally measuring a work function. The local electron potential is considered as a fixed scalar field. The validity of this approach hinges on the infinite amount of electrons – due to periodic boundary conditions – such that the position or momentum of one single electron does not influence the electronic layout of the solid.[4]

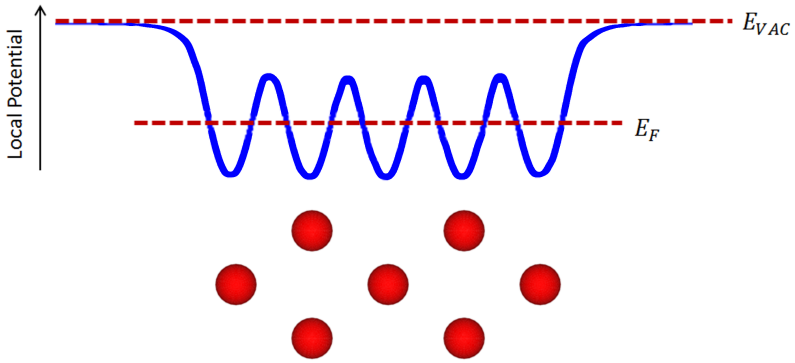

Figure 3.9: Schematic evolution of the local potential for a simple slab. For easy visual analysis, the potential is averaged in space across the planes parallel to the slab.

A simplified example is depicted in Figure 3.9. In the vacuum region the local potential converges to a maximum. The analysis of the local potential obtained from the calculation is also an easy way of reviewing the vacuum size.

Because the work function might suffer from fluctuations in the slab Fermi energy when slab thickness is varied, Fall et al.[54] proposed a method to avoid using this Fermi energy as reference point. Instead, one would use the bulk Fermi energy and switch that to the energies in the slab by comparing the integrated local potential $V[\rho](\vec{r})$. A central part of the slab over which to integrate should be chosen to compare with the bulk. As it turns out, the grid in real space used for the calculations should be quite dense to achieve a good match between the integrated local potential of the bulk and the slab. The computational time and memory required to incorporate this are beyond the scope of this thesis. In this work the Fermi energy was always derived from the slab calculation itself.

[4]This remark is innately linked to the fact that DFT is only relevant for the electronic ground state. If one would wish to model electron excitation in a truly accurate manner – say, for photon absorption – a time-dependent DFT (TDDFT) approach might provide a crucial improvement.[53]

3.4 DFT benchmarking

Since the goal of this work is to benchmark DFT for surface properties, a short review of benchmarking in literature helps to highlight the meaning of the present work and the gaps it attempts to fill. A general picture of DFT benchmarking is needed first.

The most common types of DFT benchmark studies deviate from the present work in that they focus on maximizing the accuracy for a particular materials property through evaluation of different functionals, for example binding energies of H-bonded complexes[55] or non-bonding interactions[56]. The test set on which benchmarking is performed is consequently limited. When a large test set is used, it usually involves benchmarking chemical compounds, evaluating molecular thermochemistry with localized basis sets[57–59]. Sadly, these are of limited use for solid-state physics. There have been benchmark studies for solid-state properties[60–62], but these focused on a specific subset of the elements, most often the fcc metals. Only the recent work by Lejaeghere et al.[4] sought to chart all possible shortcomings of a functional by including the entire periodic table into the test set and by benchmarking a number of properties available from experiment. This work is most notable for its rigorous statistical approach to comparing DFT results with experiment.

In the specific case of benchmarking DFT-predicted surface properties, most studies suffer the problem of having a limited test set as well. Moreover, a lot of comparisons with experiment also focus on a specific property. However, different functionals tend to yield good accuracy for one property yet fail for another[63].For this reason, LDA and PBE are still the most popular functionals for describing a surface in general.

One of the first expansive benchmark study for surface energies was performed by Vitos et al.[64]. The surface energy was compared to experiment for a very large test set of 60 metals [5]. The authors concluded the GGA was a slightly more accurate functional, although the difference with LDA was marginal – PBE underestimated the experimental surface energies with 7% whereas LDA made an overestimation of 8%. Since this is a study from 1998, the number of atomic layers and the size of the vacuum in the slabs were limited, less than 10 atomic layers and less than 10Å vacuum. Moreover, relaxation of the surface atoms was not taken into account. Although this does entail a limited precision, the results are still comparable to the present work.

A more recent study by da Silva et al.[65] also included the evaluation of work functions and relaxation effects, analyzing the contracted interlayer spacing of the surface layers. It is however limited to a select test set – only a few close-packed structures – which is representative for the full periodic table. The general trend of lower work functions and surface energies for PBE compared to LDA is confirmed. A noteworthy observation is the incorrect interlayer spacing – compared to experiment – that was found for the Ti {0001} surface.

A very insightful study which discusses the variety of ways a surface energy or work function can be obtained was recently carried out by Singh-Miller et al.[66]. Relaxations, surface energies and work functions were evaluated and compared with experiment. However, this was limited to a very specific test set – only Al, Pd , Pt, Au and Ti {0001}. The authors concluded neither PBE or LDA was a unanimously better choice, although it is clear in their results LDA does approximate surface energies and work functions better, except

[5]The same experimental data that were used in this work[8], although Vitos et al. made no attempt to reconcile the anisotropic DFT results with the isotropic experimental data.

for Ti.

Very recently – less than a year ago – Wang and Wang [67] presented simulations for 19 metals – both bcc and fcc. Although this study only utilized the PBE functional, it is of interest since it also covered bcc elements and used VASP for the calculations – making their results very interesting for comparison with the ones in this work. However, simulations for hcp elements were not carried out.

It is sometimes claimed, for example by Hugosson et al. [68], that the LDA functional offers more accurate surface energies. This is never explained or substantiated in depth, only a weak explanation along the lines of "LDA has better cancellation of errors" is given. This reasoning is not watertight. A more expansive reasoning is given by Kurth et al. [69], who highlight the difficulty of obtaining correct surface exchange-correlation energies and how more complicated functionals fail to tackle this difficulty compared to LDA. Based on benchmarking to a jellium model, they conclude the LDA functional overestimates the surface exchange energy but strongly underestimates the surface correlation energy, whereas the reverse applies for PBE. The fact that LDA would, as a net result, be a better functional for surfaces would result from a peculiar mixture of the errors on exchange and correlation canceling out.

This short overview of surface benchmarking shows the void this work attempts to fill. A full quantitative study of how well surface properties are estimated by DFT across the entire periodic table, for all crystal structures is still unavailable. Moreover, the discussion concerning the comparison between LDA and GGA might come closer to being settled by considering all elements. Especially the use of a more rigorous statistical method might present a more clear picture of the accuracy.

Chapter 4

Computational details

Being faced with the daunting task of carrying out ab initio simulations for all elements, the choice was made to tackle one crystal structure at a time. The face-centered cubic (fcc) systems were an appropriate starting point, because of their high symmetry and frequent occurrence across the periodic system. Choosing a single crystal structure allowed for the evaluation of different electronic structures corresponding to the different elements without being troubled by different geometries. This chapter is divided according to the different crystal structures that were encountered. The magnetic elements will be discussed separately, as the magnetic moments of the atoms near the surface are an interesting topic in itself, both from a computational and an experimental point of view. Some elements undergo a phase transition between $0K$ and ambient conditions, the latter begin relevant for comparison with experiment. Consequently, for some elements simulations were not performed for the ground-state crystal structure – such as Li and Na for example. There are some interesting cases where there is a phase transition close to ambient conditions. In such instances it is insightful to perform calculations for both crystal structures. Mn has a very complex crystal structure at ambient temperatures – with 58 atoms in a cubic unit cell – and will therefor not be included in the test set. There are experimental data for Ga, In and Hg, but their more complicated crystal structure resulted in them falling outside the scope of this work. There are few experimental data available – either work functions or surface energies – from Group V onwards, except for As, Sb, Bi,Te and Te. They are however not included in this work. All results and relevant details of the surface calculations can be found in Appendix B.

It seems appropriate to present the details of the simulations in an order that mirrors the workflow of the thesis. This will allow for the discussion of the specific problems as they were encountered. Before jumping into the specifics of the atomic configurations, a short talk on the - seemingly - trivial part of a slab is discussed: the vacuum region.

4.1 Determining the vacuum size

The easiest modeling parameter to evaluate is the amount of vacuum needed to prevent interaction between slabs. Typical values in literature range from 5Å to 20Å. Since only one-element materials are considered, it is quite safe to state that the size of the vacuum is almost material independent; the requirement is for the density to tail off sufficiently in between the slabs. As the primary concern is to obtain precise work functions and surface energies, convergence of these quantities with respect to vacuum size is the objective.

For the work function, this means the potential reaches a constant value at a distance far enough away from the surface.

Achieving a constant well-behaved local potential in the vacuum region is not a straightforward matter. There appear unpredictable, half-truncated oscillations in between the slabs(Figure 4.1). Indeed, upon inspection of the electron density, (extremely) small yet apparently crucial oscillations occur inside the vacuum (Figure 4.2 on the left). These are not merely caused by an overly slow dampening of the tail of the electron density away from the surface, they oscillate and become negative as well.

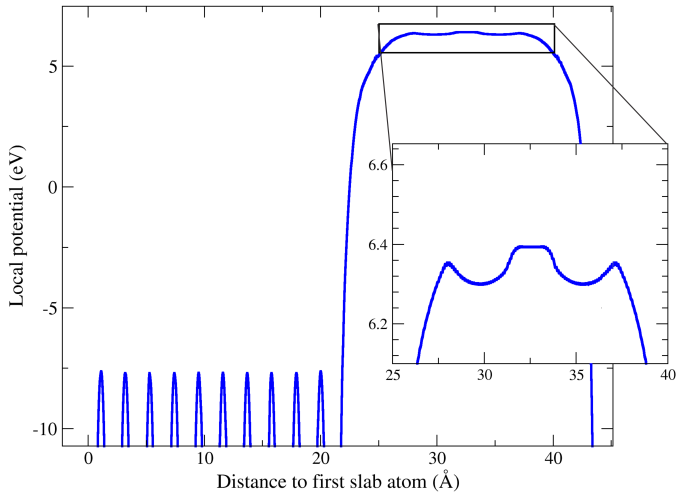

Figure 4.1: A peculiar behavior of the local potential was observed when first performing slab calculations, making the extraction of a precise work function impossible.

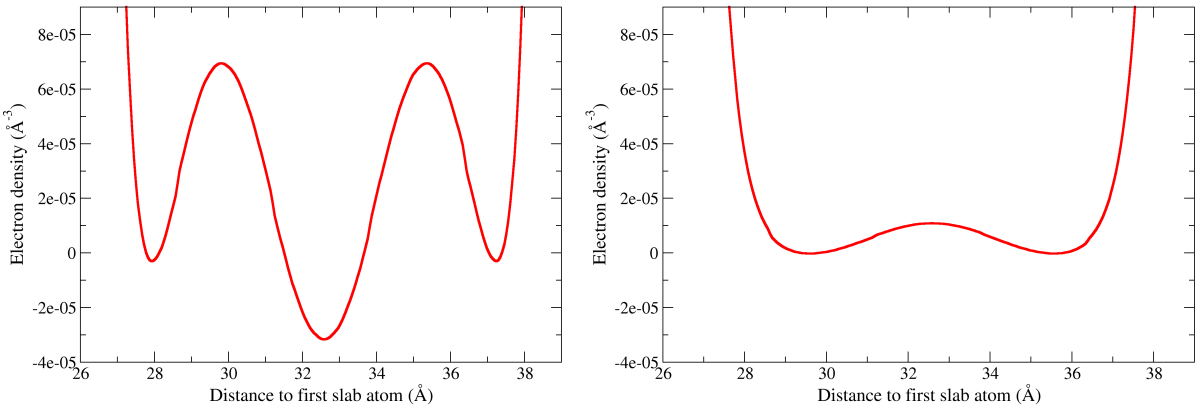

Figure 4.2: The strange local potential (Figure 4.1) is a consequence of the negative charge densities (left) - although these are extremely small. The density in the vacuum could be further damped (right) - and the negative densities resolved - by imposing a more stringent convergence criterion.

As the form of the local potential in Figure 4.1 suggests, these negative densities are clearly non-physical. They are a consequence of utilizing a non-localized basis set (the plane-wave basis set) which has a hard time precisely describing a zero density. The specific origin of the peculiar form of the local potential is a consequence of the exchange-correlation functional not being defined for negative densities. Although in most works discussing DFT work functions only the electrostatic part of the local potential is taken into account - an example which was duly followed after encountering these problems - it is desirable to obtain a realistic non-negative density in the vacuum region. This proved an extremely difficult task, as not a single computational parameter seemed to alter the situation even in the slightest. Eventually an overall high-precision calculation resulted in significantly reduced densities in between the slabs. As it turned out, imposing a more stringent convergence criterion on the self-consistent field cycle made all the difference. To ensure a well-behaving electron density for all subsequent calculations, the convergence criterion was set to $10^{-8}eV$. Note how this is somewhat more demanding than the $10^{-4}eV$ VASP default[43].

With the problem of the oscillating local potential resolved, it can now be discussed how large the vacuum should be to obtain precise work functions and surface energies. In Figure 4.4 the effect of the vacuum size is investigated. As adding empty space to a unit cell does not increase computational demands too dramatically – certainly not in the way an added atomic layer does – the aim was just to find a "safe setting". Cs was selected as test element. Since it is a heavy first-group element, its electron density is expected to tail off relatively slow. One can conclude 10Å vacuum is indeed somewhat of a minimum requirement. To be absolutely safe, all calculations were performed with a vacuum of about 20Å - the limited extra cost well worth the peace of mind.[1]

4.2 Face-centered cubic

4.2.1 Crystallography

As a notation system for crystallographic planes the Miller indices are used, which are determined by the reciprocal of the distances between the origin and the points where the plane intersects the coordinate axes.These axes are defined by the basis vectors of the unit cell which described the crystal. Crystallographic directions are indicated with three indices determined by the expansion in these basis vectors. The symmetry of the crystal systems will always be implicitly accounted for by denoting the families of planes as {*hkl*} and the families of directions as <*hkl*>, whereby any permutation or reflection of the indices *hkl* results in an equivalent plane or direction.

In a cubic crystal system, the {111}, {100} and {110} surfaces are quite simple. This allows for an easy slab construction which doesn't strain the spatial aptitude of the reader too much. Each atom in the face-centered cubic (fcc) system (Figure 4.3) has twelve nearest neighbors and is equivalent, which means the termination of the slabs can only be done in one way.

The {111} slab has an ABC stacking (see top left Figure 4.5) where all planes are equidistant and merely a translation of each other. Three nearest neighbors are removed by creating the {111} surface. The base plane of the primitive slab unit cell has a surface area of $\frac{\sqrt{3}}{4}a^2$, with a the lattice parameter (the side of the cubic

[1] In the case of the Cs test, increasing the vacuum from 12 to 22Å only increased the calculation time by about 20%

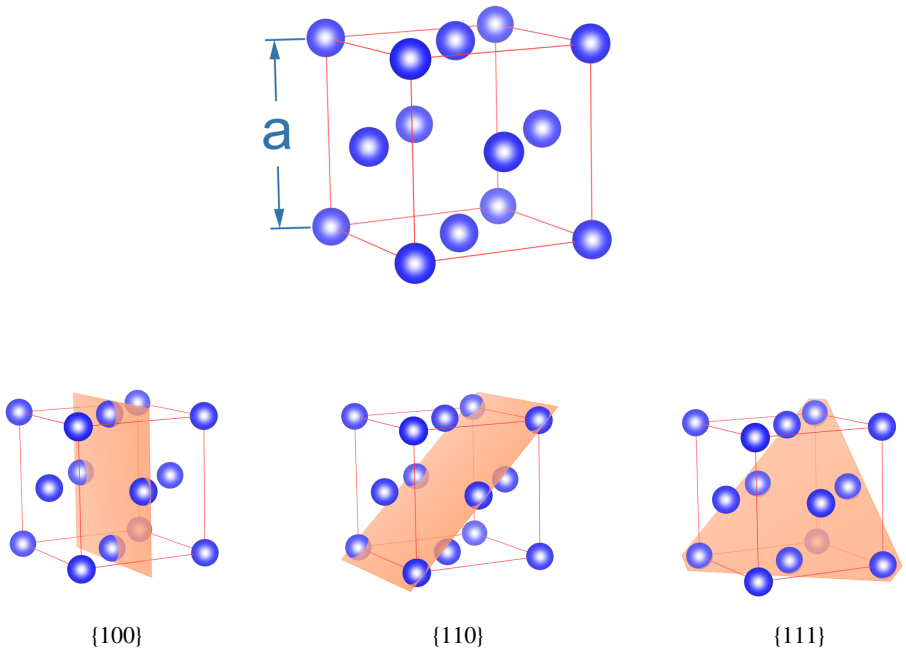

Figure 4.3: The conventional unit cell of the fcc crystal system and the low-index planes.

unit cell) the material dependent characteristic length, and a spacing between the layers of $\sqrt{3}a$.

Both the {100} and {110} slabs have an AB stacking (Figure 4.5). In the former, four nearest neighbors are removed while in the latter, five of them are cut away. The number of nearest neighbors that are removed is mentioned mainly to paint a qualitative picture of how the atomic configuration is changed for a surface atom. It already provides some indication of what the anisotropy of the surface energy might look like. The {100} slab has a base surface of $\frac{a^2}{2}$ and an interlayer spacing of $\frac{a}{2}$, whereas the {110} slab has the least densely packed layers with a base surface of $\frac{a^2}{\sqrt{2}}$ and a spacing of $\frac{a}{2\sqrt{2}}$ between the atomic layers. Naturally, since the slabs for an element are always derived from the same original bulk geometry, the planar density of atoms in a layer is always inversely proportional to the spacing between the layers.

If symmetry is taken into account, the three aforementioned surfaces actually encompass 26 different orientations of the normal of surfaces.[3] By virtue of the highly symmetric cubic crystal structure, three simple surfaces thus already provide a wealth of directional information. Recalling the procedure put forward in Chapter 2 to obtain an "average" surface energy - needed for comparison with experiment - creating the Wulff plot from the simple surfaces. The three slabs for which the surface energies were calculated enable the derivation of the surface energy for any random slab with their normals in the {110} or {100} planes. In total, all directions in 9 planes are covered in this way. Figure 4.6 illustrates the density of "known" surface energies that are obtained in this way. Note how these lines - for which the surface energy is derived - divide the unit sphere in 6 surface triangles in every octant. A good approximation of the average surface energy in such a surface triangle is to take the average across its borders:

[2]These settings are the chosen settings for work function and surface energy convergence - see further on.

[3]"Surfaces with their normal in a direction" or "Surfaces normal to a direction" are both ineloquent ways of describing the orientation of a surface. For brevity, we will talk about "The direction of a surface".

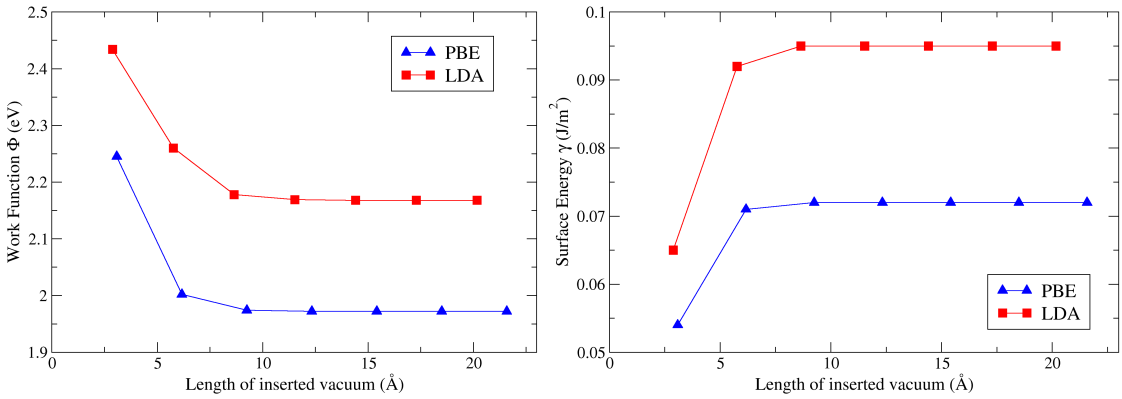

Figure 4.4: A convergence test of the inserted vacuum for a Cs {100} slab consisting of 19 layers. Calculations were performed with a 25×25 $\vec{k}$-point grid and a $500eV$ cut-off energy.[2]

$$\gamma_{average} = \frac{\int_{C_1} \gamma_1(\theta)d\theta}{L_{C_1}} + \frac{\int_{C_2} \gamma_2(\theta)d\theta}{L_{C_2}} + \frac{\int_{C_3} \gamma_3(\theta)d\theta}{L_{C_3}} \tag{4.1}$$

where the knowledge of the functions $\gamma_i(\theta)$ on the curves C_i is used. As all the triangular segments have the same surface area on the sphere and have the same sides, one integration like equation 4.1 is sufficient to obtain the general isotropic surface energy.

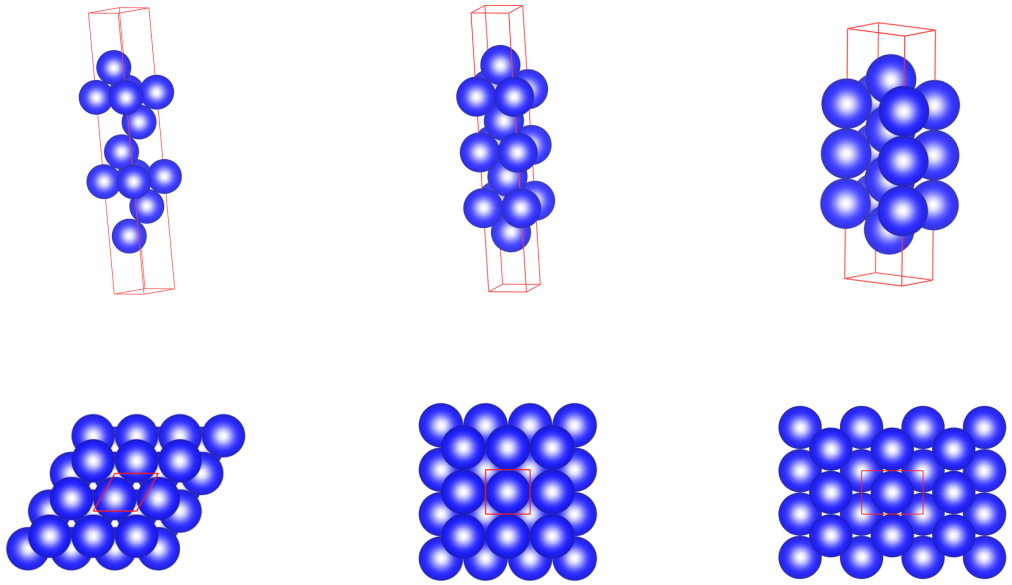

Figure 4.5: Cross-section (top) and top view (bottom) of the slabs modeling the low-index surfaces. From left to right: the {111}, {100} and {110} slabs.

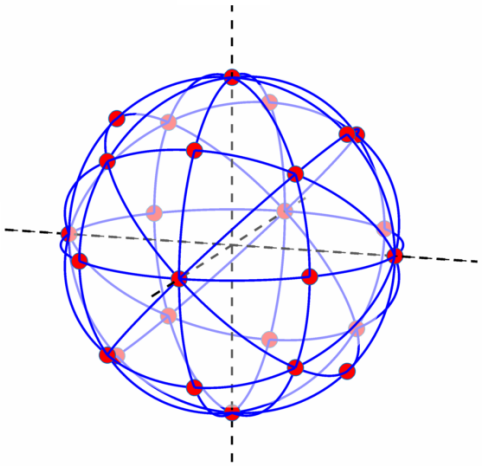

Figure 4.6: To paint a picture of the directions of the plane normals in three-dimensional space: the red dots indicate a calculated direction, while the blue lines indicate the directions for which a surface energy was derived.

4.2.2 Model parameters and precision

The first step to obtaining precise ab initio results is to evaluate the impact of the computational parameters and - in the case of surfaces - the slab model itself. There are three influential computational parameters and two aspects of the slab which must be taken into account. The smearing scheme - and its width - will invoke partial electron occupancies of the bands, which will certainly have an influence on the result. The general rule is that tetrahedron smearing renders the most accurate energies[46] but it is unreliable for geometric optimization, as the forces for metals are inaccurate, Methfessel-Paxton smearing should be used in this case[43]. The other two computational settings impacting the results are the cut-off energy and the $\vec{k}$-point density. The influence of the former is easily evaluated, as it is mostly dependent on the PAW potential being used and the quantity one wishes to predict. For each element, only the valence electron behavior outside the core is important, a consequence of using PAW potentials with a frozen core. This results in the cut-off energy being largely independent of the element at hand[4]. Unless stated otherwise, the cut-off for a calculation will be $500eV$ - with the exception of C and Li, for which cut-off energies of $600eV$ and $800eV$ were chosen respectively. These two elements require a larger cut-off[43].

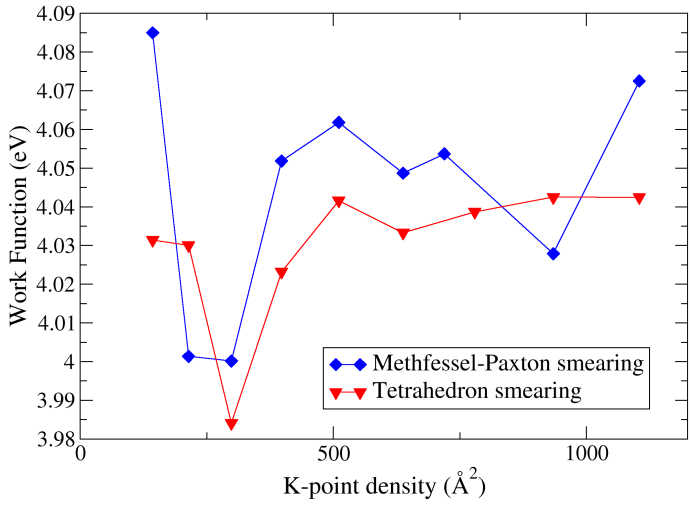

Figure 4.7: The work function of Al {111} slabs with 13 layers as a function of the used $\vec{k}$-point density. Comparison of the work function obtained with different smearing schemes: tetrahedron method with Blöchl corrections and Methfessel-Paxton smearing with $\sigma = 0.01eV$.

Both work function and surface energy are a lot more sensitive to the density of the meshing in reciprocal space[5]. Moreover, using a finite-temperature smearing scheme, such as Methfessel-Paxton or Gaussian, results in huge variations of the work function with respect to a changing $\vec{k}$-point density (Figure 4.7). For this reason, tetrahedron smearing - which offered a lot more stability - was used at all times, except for geometric

[4] A complete overview of the recommended cut-off energies for every PAW potential is presented in the VASP manual[43]. These recommended cut-offs are mostly in the $250eV - 300eV$ region, some way short of the $500eV$ cut-off in this work. This is why the values for C and Li were also scaled up to match this higher precision requirement.

[5] When comparisons have to be made, $\vec{k}$-point density will be expressed in Å^2; the result of multiplying the number of $\vec{k}$-points in the reciprocal plane , as $\vec{k}$-point grids for slabs are two-dimensional, with the base surface of the slab in real space (a factor of $4\pi^2$ is omitted for clarity) than the energy.

optimization. Because of this choice, it was not crucial to test the setting of the σ-parameter with respect to work function or surface energy[6]. It should be chosen small enough to obtain precise forces which in turn determine the relaxation and reconstruction. However, these are not sensitive at all to the σ-parameter. The $\vec{k}$-point meshing does have some notable impact on forces, the force on the top layer of course the most important one. With respect to varying $\vec{k}$-point grids the precision was 10 to 15 $\frac{meV}{\text{Å}}$ in the worst case (Al). Precision demands on forces are less stringent than precision demands on surface energy or work function, as they are only a contributor of second order to work functions or surface energies. To keep the workflow simple and clear, $\sigma = 0.01eV$ is always used as the smearing parameter and the $\vec{k}$-point grid and slab thickness for optimization were the ones obtained from convergence testing for work function and surface energy.

The slab thickness and the number of relaxed layers are structural degrees of freedom which influence the end result. The goal of the structure is to accurately describe a real surface in order to derive both work function and surface energy, indicating the thickness and free layers should have no impact on these quantities.

It is a huge task to test all settings rigorously for all elements. There is however a justifiable shortcut that can be made. By selecting a representative set of elements out of the entire fcc family, one can derive general settings for all fcc elements. The crux of this method consist in selecting a set that sufficiently covers the variation in the fcc family. A standard light transition element was chosen (Cu), along with an s-metal (Sr), a p-metal (Al) and a heavy element (Au).

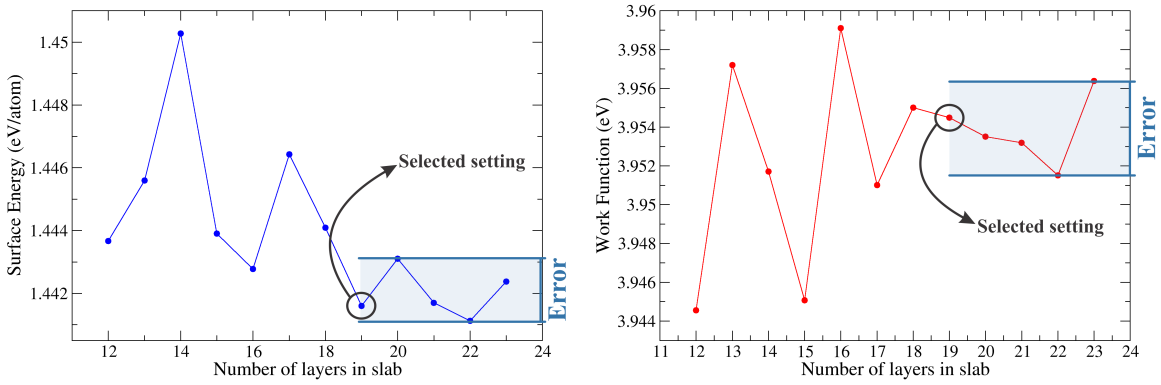

Figure 4.8: Selecting a certain setting results in a residual computational imprecision. This is illustrated here for both the surface energy and the work function of V {100} slabs of different thickness and a 27×27 $\vec{k}$-point grid.

Demanding a certain precision for work functions and surface energies a priori before carrying out any of these convergence tests would be a flawed approach. For each element and setting a separate assessment must be made of the return on investment with respect to the computational cost. When the choice for a particular setting is made, this invariably entails a residual imprecision. Taking a stroll around the periodic table, it is interesting to chart these imprecisions for all tested elements and settings. This is not only of interest to gain insight in how precisely a DFT work function and surface energy can be calculated, but might also be of importance when comparing with experiment. A "safe" estimate for the error associated with a

[6]In fact this was done anyway for Al, Sr, Au and Cu; the region $\sigma = 0.01eV$ to $\sigma = 0.1eV$ turned out to be an optimal range.

particular setting is the distance between the minimum and maximum result when the setting is increased beyond the chosen one. This procedure is illustrated in Figure 4.8.

For the fcc elements[7] a peculiar behavior was observed with respect to varying slab thickness: a - seemingly periodic - oscillatory evolution of the work function and surface energy (Figure 4.9), called a quantum size effect (QSE). Apart from the Cu {110} slabs, the same problem was found for the {110} slabs of Ir, Pd, Pt, Cu, Ag, Au and Pb. For Pb in particular, the {111} slab also showed the oscillations[8].

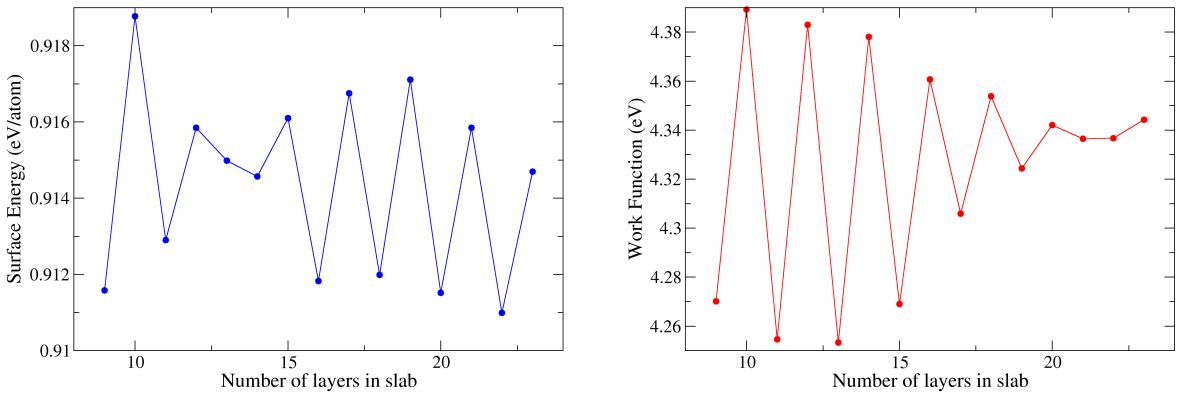

Figure 4.9: Quantum size effects for the Cu {110} slabs with a 27×17 $\vec{k}$-point grid. Especially the size of the oscillations in the work function (right) are remarkable - compare with Figure 4.7 or 4.8.

The variations in work function - apart from the periodicity, the surface energies in Figure 4.9 are actually quite precise - can be damped when thicker slabs are created. Why then, is this computational nuisance highlighted here? It turns out that this behavior can actually be observed experimentally [70,71] - in terms of the surface energy. The "preferential" thickness of Pb films on Si {111} presents an informative case study and especially the explanation formulated by Wei and Chou [72] puts the matter in a new light. They investigated the electronic levels with DFT, specifically the levels at the Γ-point near the Fermi level. They related the work function and surface energy oscillations to the variation in the placement of the additional electronic levels right beneath the Fermi energy, i.e. the highest occupied orbital at the Γ-point.

The most important part to take away from this explanation - in itself, it merely describes what is happening electronically by using DFT - is that there is now an indicator for the occurrence of the QSE: when the lowest occupied band steeply intersects the Fermi level, the levels in the slab will exhibit larger variations when the thickness is varied. To weed out any other QSE, for all slabs of all elements three successive thicknesses were evaluated - to weed out any other QSE.

Now all of the aforementioned difficulties have been solved, the settings and their precisions can be established. In Table 4.1 the final settings for the test set are presented. With respect to $\vec{k}$-point density there is very little to conclude apart from the fact that most meshes resulting in converged quantities lie fairly close

[7] In all other convergence tests with respect to slab thickness, no such large and periodic oscillations were observed.

[8] In fact, the oscillations can also be observed in other slabs, but the cases specifically mentioned here were of note because of the *size* of the oscillations and the increased slab thickness required to absolve them.

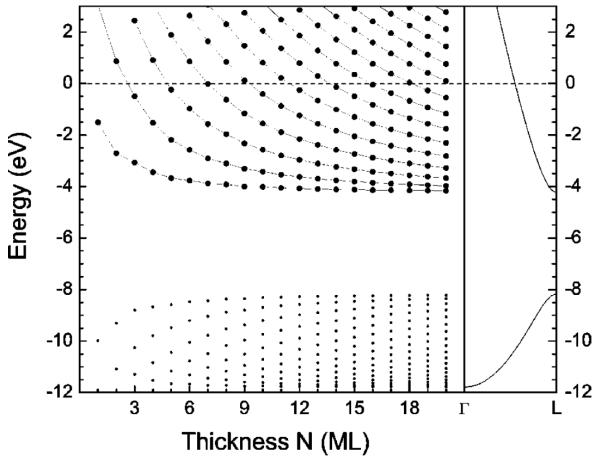

Figure 4.10: When layers are added to the slab, the "original" band of the bulk is folded along the $\Gamma - L$ direction. At the slab thickness where an extra fold (or point, when one only considers the Γ-point) slumps under the Fermi level there is an increase in surface energy - and vice versa. The figure is taken directly from Wei and Chou.[72]

together. Sr does seem to behave somewhat kinder to a coarser $\vec{k}$-mesh. Creating a mesh with a planar density of 6000Å^2 does seem to cover all the bases. As was mentioned before, a number of thicknesses were evaluated for each surface to check for QSE. Based on the converged values for the test set (Table 4.1), the slabs had 14, 15 and 16 layers in them. From the results for these three thicknesses, the optimal one was then selected (meaning: the middle one of the three), unless of course QSE occurred, in which case thicker slabs were needed. Al is somewhat of a more demanding element with respect to slab thickness, which is also shown in its achieved precision with respect to slab thickness (Table 4.2). Relaxations do not entail large imprecisions and using three free layers on each side of the slab is sufficient for all orientations.

As can be seen in Table 4.2, the main source of imprecision are the slab thickness and $\vec{k}$-meshing. Although these computational errors are certainly not negligible - sometimes amounting to $2-3\%$ - they are very small compared to the experimental deviations.

Element	Slab	$\vec{k}$-points (Å^2)	Layers	Cut-off (eV)	Free Layers
Al	{111}	4400	17	500	1
	{100}	5100	15	500	2
	{110}	2600	15	500	3
Au	{111}	3300	11	400	3
	{100}	3100	13	400	3
	{110}	3600	21	400	3
Cu	{111}	3600	13	500	3
	{100}	3500	13	500	1
	{110}	4100	21	500	3
Sr	{111}	2700	13	500	1
	{100}	1500	13	500	3
	{110}	4300	12	500	1

Table 4.1: Settings for which satisfactory convergence of the surface energy and work function was obtain.

		$\vec{k}$-points		Layers		Cut-off		Free Layers		Total	
Element	Slab	$\Delta\Phi$	$\Delta\sigma$	$\Delta\Phi$	$\Delta\sigma$	$\Delta\Phi$	$\Delta\sigma$	$\Delta\Phi$	$\Delta\sigma$	$\Delta\Phi$	$\Delta\sigma$
Al	{111}	10	4	25	4	0.1	2	4	0	27	6
	{100}	18	3	30	4	0.1	2	0	0	35	5
	{110}	10	5	20	20	0.1	2	3	2	23	21
Au	{111}	15	4	1	2	0.3	2	4	1	16	5
	{100}	6	2	6	4	0.3	2	10	1	13	5
	{110}	3	5	10	2	0.3	2	1	0	10	6
Cu	{111}	15	4	1	2	0.5	2	4	0	16	5
	{100}	5	2	15	1	0.5	2	3	0	16	15
	{110}	5	2	10	6	0.5	2	1	0	11	7
Sr	{111}	5	2	10	0	0.1	1	4	1	12	2
	{100}	10	2	5	1	0.1	1	1	0	11	2
	{110}	7	2	20	2	0.1	1	1	0	21	3

Table 4.2: The precision associated with the settings chosen (Table 4.1) for fcc elements. Both $\Delta\Phi$ and $\Delta\sigma$ are in meV - σ being the surface energy per surface atom.

4.3 Body centered cubic

The same procedure will be repeated for the bcc crystal system: four representative elements are selected and these are rigorously tested with respect to $\vec{k}$-meshing, slab thickness and number of free layers; cut-off energy and the σ-parameter are no different compared to fcc, as they are expected to be mainly dependent on the sort of simulation, the quantities of interest and the chemical elements involved. K, V, Nb and W were the elements of choice[9]. The base surface area and spacing between layers is presented in Table 4.3.

[9] V and Nb are in the same group. Consequently, one would expect them to behave in a similar way, both in terms of simulation parameters and results. It is interesting to evaluate whether this is actually true.

4.3.1 Crystallography

The slabs for the low-index surfaces are again quite simple. The slabs have the same stacking periodicity as for fcc - ABC for {111} and AB for {100} and {110} - and always one atom per layer in the slab unit cell, but there are some stark differences between the structures. Instead of a twelve-fold configuration, the bcc structure has eight nearest neighbors, which results in a more anisotropic structural character. The anisotropy of the packing - ratio of the largest base surface area per atom and the smallest - is 2.45 where this was only 1.63 for fcc. All surface areas of the base of the slab unit cells are presented in Table 4.3

Orientation	FCC	BCC
{111}	$\frac{\sqrt{3}}{4}a^2$	$\sqrt{3}a^2$
{100}	$\frac{a^2}{2}$	a^2
{110}	$\frac{a^2}{\sqrt{2}}$	$\frac{a^2}{\sqrt{2}}$

Table 4.3: Comparison between fcc and bcc surface areas per atom of the base of the slab unit cells.

It is also notable how the order of anisotropy has changed. Whereas for fcc the surface area increased - and the packing decreases - from {111} to {110}, the opposite occurs in the bcc structure. One should be careful directly comparing the values in Table 4.3 as the fcc structure has 4 atoms in its conventional unit cell (Figure 4.3), whereas the bcc structure has only two (Figure 4.11) which results in smaller lattice parameters for the bcc structure, which is less densely packed in itself. The main purpose of Table 4.3 is to illustrate the different anisotropy. The manner in which the isotropic surface energy is derived is of course the same as for the fcc case, as the cubic symmetry is unchanged.

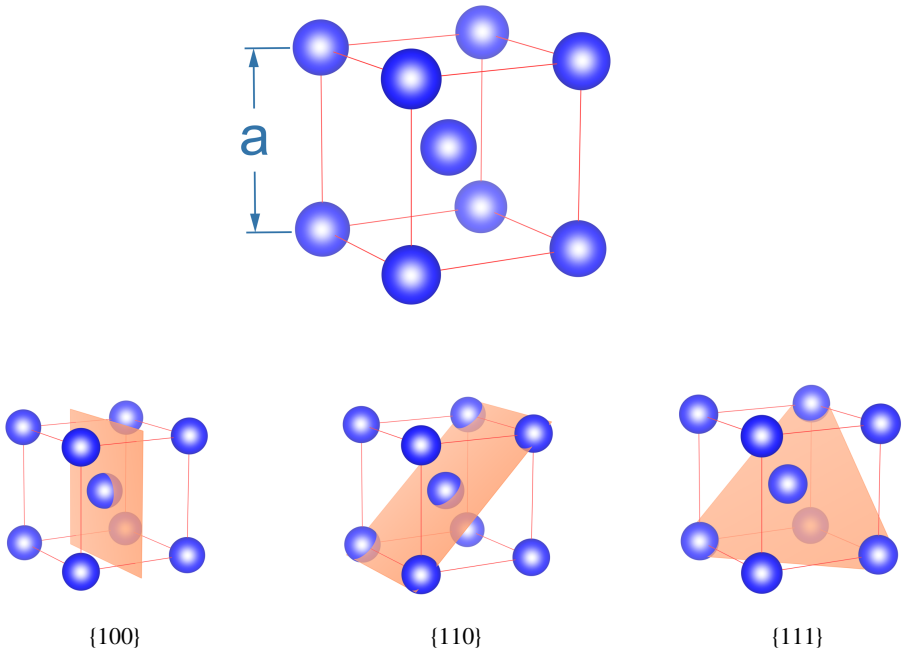

Figure 4.11: The conventional unit cell of the bcc crystal system and the low-index planes.

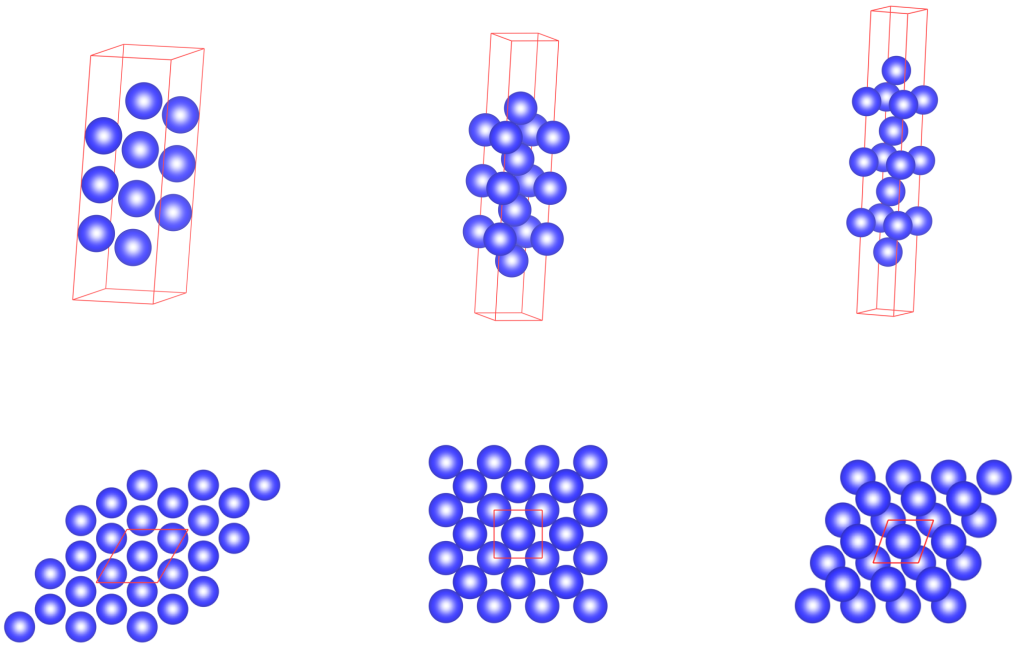

Figure 4.12: Cross-section (top) and top view (bottom) of the slabs modeling the low-index surfaces. From left to right: the {111}, {100} and {110} slabs.

4.3.2 Model parameters and precision

It requires somewhat more computational effort to obtain precise work functions and surface energies for bcc elements compared to fcc elements. Both thicker slabs and a denser $\vec{k}$-mesh were required, yet still the precision (Table 4.5) is not as high as it was for the fcc elements (Table 4.2).

Based on the results presented in Table 4.4, slabs of 22 layers for {111}, 19 layers for {100} and 15 layers for {111} were used for all other bcc elements. In regard to $\vec{k}$-point density, K (potassium) required a notably denser $\vec{k}$-mesh compared to the other elements in the test set. Because of this different behavior to the transition metals, K was chosen as representative for the s-metals and the other three elements for the transition metals. Relaxation demands were also markedly different compared to fcc elements. The {100} and {110} slabs only needed one free layer – or none at all – to obtain a precise work function and surface energy. The {111} slab optimization demanded more freedom and needed 4 free atomic layers.

Element	Slab	$\vec{k}$-points (Å^2)	Layers	Free Layers
Nb	{111}	4300	19	4
	{100}	10500	14	1
	{110}	4100	11	1
K	{111}	17500	22	4
	{100}	12300	16	0
	{110}	10500	15	1
V	{111}	8200	18	4
	{100}	6500	18	1
	{110}	8700	13	1
W	{111}	6400	21	4
	{100}	11000	15	1
	{110}	7000	15	1

Table 4.4: The settings that were selected for the bcc test set.

		$\vec{k}$-points		Layers		Free Layers		Total	
Element	Slab	$\Delta\Phi$	$\Delta\sigma$	$\Delta\Phi$	$\Delta\sigma$	$\Delta\Phi$	$\Delta\sigma$	$\Delta\Phi$	$\Delta\sigma$
Nb	{111}	4	1	25	15	4	4	26	16
	{100}	7	2	10	10	7	13	14	17
	{110}	5	4	5	4	10	5	12	8
K	{111}	10	1	35	5	5	1	37	5
	{100}	4	2	15	2	1	0	16	3
	{110}	5	0	15	0	1	0	16	0
V	{111}	3	1	60	10	10	3	61	10
	{100}	3	1	8	4	10	5	13	6
	{110}	5	1	2	4	3	1	6	4
W	{111}	4	1	35	10	10	8	37	13
	{100}	6	1	20	6	6	9	22	11
	{110}	5	1	3	25	1	1	6	25

Table 4.5: The precision associated with the settings chosen (Table 4.4) for bcc elements. Both $\Delta\Phi$ and $\Delta\sigma$ are in meV - σ being the surface energy per surface atom.

4.4 Diamond lattice

4.4.1 Crystallography

The diamond lattice is a cubic system as well, but the atomic structure is complicated by the two-atom motif. As a consequence the {111} planes can be of two different terminations and the {110} planes have two atoms per layer in the slab unit cell. The latter is just a modeling nuisance, increasing computational cost. but the different interlayer spacings in the <111> direction beg the question: do both terminations occur in reality?

The matter is further complicated by surface reconstructions. C, Si, Ge and Sn are the four elements that form a diamond crystal structure – although it is not the ground-state crystal structure for C. These Group IV elements undergo sp^3 hybridization to allow for a four-fold configuration of strongly covalent bonds, forming a less densely packed structure than metals. Because the bonds in these diamond structures are strongly

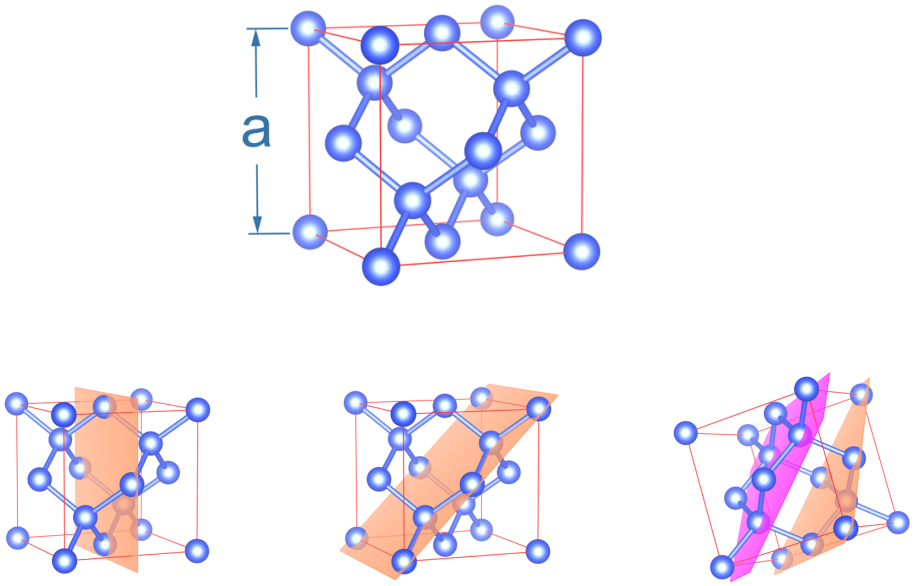

Figure 4.13: The conventional unit cell of the diamond crystal system and the low-index miller planes.

directional and the structure is less dense, severe surface reconstructions will occur. As was mentioned in chapter 3, the aim of this work is not to perform an exhaustive evaluation of all possible reconstructions, such endeavors are quite prevalent in literature already.[50,73]

Based on the work of previous authors[50], it is concluded that the primitive slab unit cell with two atoms per layer is a satisfactory simulation of the {110} surface. Because there are two - non-equivalent - atoms per layer, a reconstruction occurs "naturally"; one could call it a 1×1 reconstruction. The {111} and {100} do have a dramatic reconfiguration of the top layers - both energetically and geometrically - and 2×1 reconstructions willbe taken into account. In practice, the reconstructions are obtained by combining two slab unit cells and slightly breaking the symmetry to initiate the geometrical adaptation. The argument for only taking into account the 2×1 reconstructions is on the basis of the DFT study performed by Stekolnikov[50], which showed more complicated reconstructions to be energetically quite close to the basic 2×1 surface reconstruction.[10] Because the surfaces of the elements in a diamond structure depend heavily on the reconstructions, a discussion on layer packing and spacing - as was done for fcc and bcc - is not very interesting. As the space group of the diamond lattice is the same as for the fcc lattice ($Fm\bar{3}m$), the anisotropy in the packing is also the same in relative terms. Since this is another case of cubic symmetry. Deriving the isotropic surface energy is the performed in the same way as for fcc and bcc.

The surface energies presented in Table 4.6 highlight the importance of including the reconstruction: it lowers the surface energy more than any relaxation. The other significant energetic difference is between the {111} and $\{\bar{1}11\}$ slabs. The latter is the termination which only removes one of the four nearest neighbors, whereas the former removes three. The difference in surface energy[11] means one termination is more stable

[10] This manifests itself in the experimental difficulty of obtaining such a more complex top structure. The notorious 7×7 reconstruction of Si {111} for example, requires specific annealing of the grown layer.[74]

[11] Only for Si was the reconstruction of the {111} slab taken into account. Although it causes a significant lowering of the surface

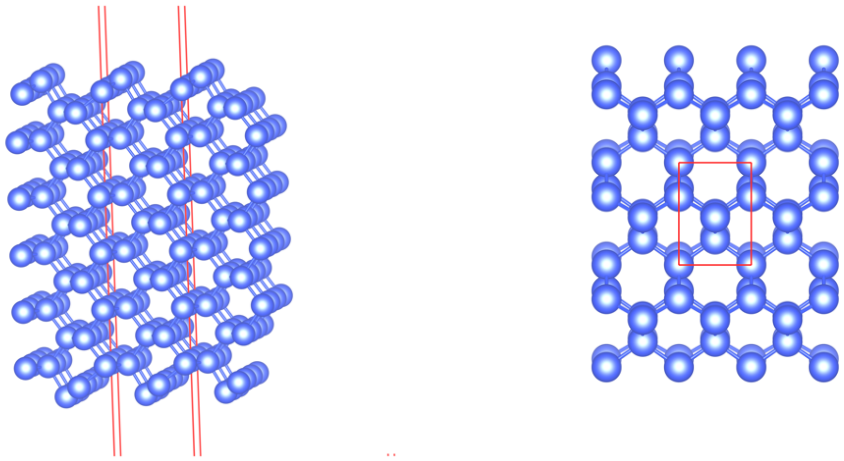

Figure 4.14: The {110} reconstructed surface of Si.

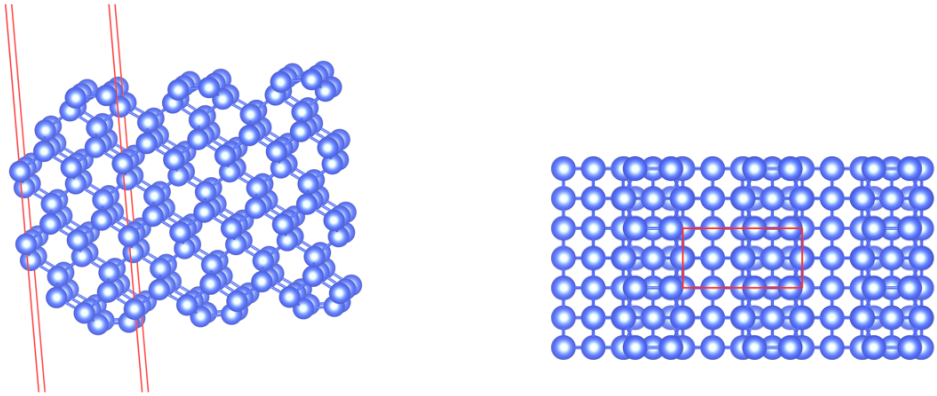

Figure 4.15: The 2×1 {100} reconstructed surface of Si.

than the other. Only the most energetically stable surface is of interest for comparison with experiment. If a layers is grown or a material is cracked[75], the surface that is more stable will be produced.

Although the impact of reconstruction and termination was discussed here by in terms of the surface energy, the work function changes too when reconstructions are taken into account. It drops by about $5 - 20\%$ compared to the work function for unreconstructed slabs.

A detailed account of the convergence tests is omitted here, as all elements with the diamond lattice are of the same valence electron configuration, the settings used can be found in Appendix C. It was also computationally quite cheap to obtain very good precision on both work function and surface energy: the residual imprecision is smaller than $15meV$ and $10\frac{meV}{\text{atom}}$.

energy, the geometry of the reconstructed surface still differs from the $\{\bar{1}11\}$

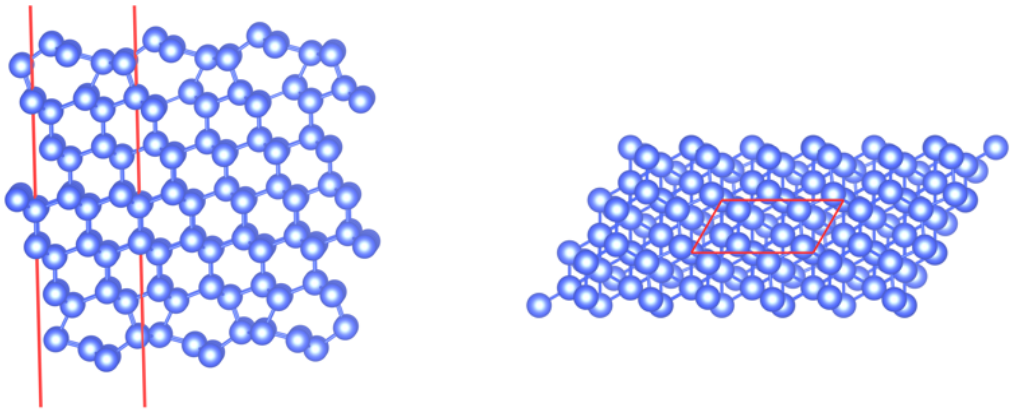

Figure 4.16: The 2×1 {110} reconstructed surface of Si.

		Relaxed $\gamma(\frac{J}{m^2})$	2×1 Reconstructed $\gamma(\frac{J}{m^2})$
C	{111}	12.548	n/a
	$\{\bar{1}11\}$	6.277	4.05
	{100}	8.737	5.198
Si	{111}	2.807	1.569
	$\{\bar{1}11\}$	1.574	1.361
	{100}	2.16	1.406
Ge	{111}	1.815	n/a
	$\{\bar{1}11\}$	1.073	0.89
	{100}	1.389	1.003
Sn	{111}	1.244	n/a
	$\{\bar{1}11\}$	0.676	0.54
	{100}	0.894	0.628

Table 4.6: Effect of reconstruction on the surface energy and the difference in surface energy between two different terminations for the diamond-type {111} slabs with PBE.

4.4.2 Alternative crystal structures for C and Sn

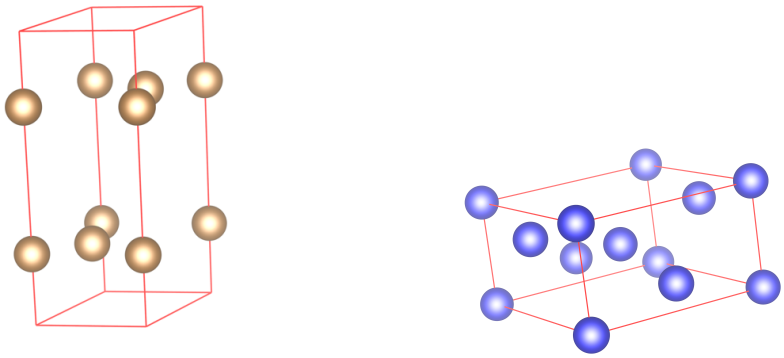

Graphite Sn-α

Figure 4.17: The unit cells of C (graphite) and Sn-β

For C and Sn, the diamond structure is not the only crystallographic phase of interest. The most stable configuration for C is graphite, a hexagonal structure. Indeed, it is only because of the interesting properties and coveted luxury C (Diamond) is well-known - its rarity is undisputed. The ground-state structure of Sn, on the other hand, is a diamond configuration (Sn-α or gray tin) but at room temperature the most stable structure is a tetragonal one (Sn-β or white tin) - with an atom in the center and two on the faces (Figure 4.17). This is important for comparison with work function data, although there is only one polycrystalline experimental value.

In Chapter 2 it was stressed how there is no structural information in the experimental surface energies for the solids as they were derived by Tyson and Miller. In light of this it is interesting to compare the surface energy of the same elements, but in different (realistic) configurations. The comparisons between bcc and fcc Fe and between antiferromagnetic (AF) and non-magnetic (NM) Cr are also included.

	Ground structure at $0K$ $\gamma(\frac{J}{m^2})$	Alternative structure $\gamma(\frac{J}{m^2})$
Sn	0.688	0.457
C	0.119	5.173
Fe	2.713	2.388
Cr	3.31	3.748

Table 4.7: A comparison of the surface energy for the same element in a different crystallographic structures. More information on the ground-state structures and alternative structures is provided in the text.

The differences from left to right in Table 4.7 show how cyrstal structure certainly has an influence on the surface energy - as one would logically expect. For Fe and Cr one could argue these differences are still within range of the error on experiment ($0.26\frac{J}{m^2}$ for Fe and $0.27\frac{J}{m^2}$ for Cr), but for Sn it is very significant.

The huge difference between graphite and diamond is because of the unique graphite structure, which is essentially made up out of weakly interacting graphene layers. Because these layers interact very little, vvan der Waals forces play a significant role. Including dispersion interaction in an empirical way, by adding it

after the electronic scf cycle, described graphite a lot better. This was done for PBE – the DFT-D method by Grimme is not applicable to LDA – and the surface energy increased from $0.119\frac{J}{m^2}$ to $0.163\frac{J}{m^2}$.

4.5 Hexagonal closed packed system

4.5.1 Crystallography

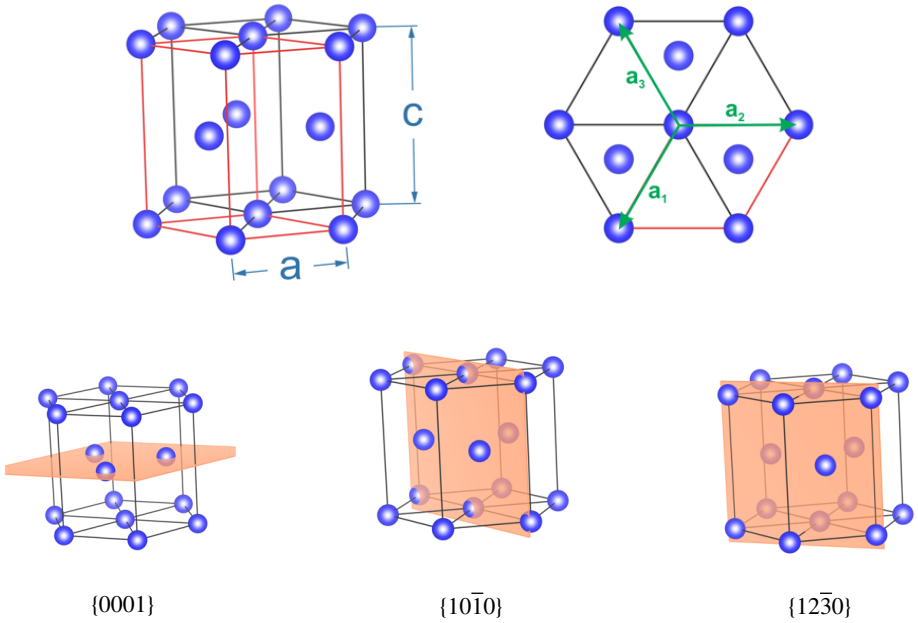

Figure 4.18: The hcp crystal structure and the low-index planes that were modeled.

The fcc system is not the only crystal system which exhibits a maximal packing. The hexagonal close packed (hcp) structure is another atomic configuration which fills space optimally. Both systems will therefore show similarities. Each atom again has twelve nearest neighbors and the {001} slabs are equivalent to the fcc {111} slabs, but for an AB stacking periodicity instead of an ABC. The most important difference - and what really discerns the hcp structure from bcc and fcc - is the presence of two atoms in the motif. Just as was the case for the diamond lattice, this will entail a number of complications for the slab unit cell.

As the hexagonal lattice is not cubic, two of the conventional lattice vectors are not orthogonal. These are called $\vec{a}_1$ and $\vec{a}_2$ – as shown in the top right of Figure 4.18 – to highlight their equal length. Both of them are orthogonal to the $\vec{c}$-vector, which is longer. Clearly, this crystal system is geometrically somewhat more complicated than the cubic systems. The Miller indices illustrate this nicely: in a cubic system a plane with Miller indices (hkl) has the neat property the direction $[hkl]$ is perpendicular to it. The symmetrically equivalent planes and directions are also readily available through a simple permutation of the indexes. This simplicity is not present in the hexagonal system. An indexing method which does offer a better understanding is the Miller-Bravais system. The Miller-Bravais indices are in fact the same as the Miller indices but add a fourth index, determined by the additional lattice vector $\vec{a}_3$, drawn in the top right of Figure 4.18. This fourth index (named i) is equal to $-(h + k)$ and is thus not independent of the first two, but symmetrically

equivalent planes can now be found by permutation of the three first indices of a plane (*hkil*). The Miller-Bravais indices will be used to indicate all hcp planes.

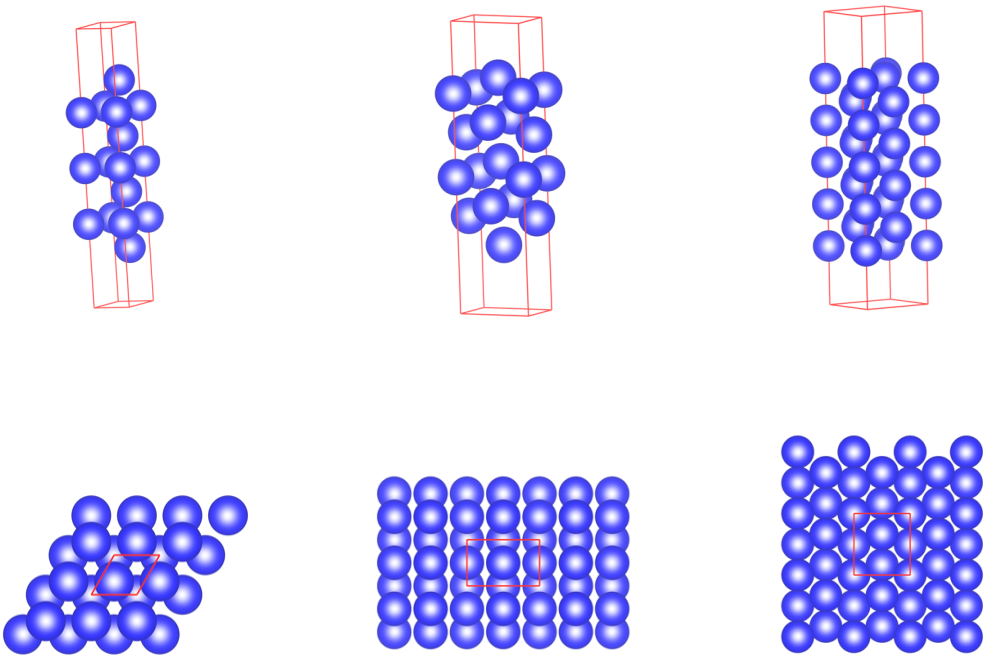

Figure 4.19: Cross-section (top) and top view (bottom) of the slabs modeling the low-index surfaces. From left to right: the {0001}, {10$\bar{1}$0} and {12$\bar{3}$0} slabs.

The {0001}, {10$\bar{1}$0} and {12$\bar{3}$0} slabs were simulated for all hcp elements, they are depicted in Figure 4.19. As mentioned above, the {0001} surface is similar to the {111} surface of fcc. Both are the most densely packed planes and each surface atom for these slabs retains nine of its twelve nearest neighbors. The other two slabs are somewhat more complicated as the {10$\bar{1}$0} slab has two different terminations and the {12$\bar{3}$0} slab has two atoms in every layer. This is similar to what was observed for the {111} and {110} diamond lattice slabs respectively. Just as was the case for the {111} slab of the diamond lattice, the termination of the {10$\bar{1}$0} slab with the smallest spacing between the top two layers is energetically favored – typically by about 10% – since more nearest neighbors are removed. Consequently this is the termination that was simulated.

The other slabs in the hcp structure, where $\vec{c}$ and $\vec{a}$ directions are mixed, are somewhat more of a nuisance. This is particularly caused by the deviation of the $\frac{c}{a}$ ratio from the theoretical one - i.e. $\frac{\sqrt{8}}{3} \approx 1.633$ for the close-packed condition. Most elements will exhibit a slightly altered ratio, of which the deviation from the ideal value is strongly dependent on electronic configuration.[12]. This breaking of the symmetry for the actual hcp elements causes the slabs to exhibit no short-range stacking periodicity. In the beginning, some of the more complicated slabs of Ti were included during convergence testing, but poor convergence with respect to $\vec{k}$-meshing and slab thickness combined with difficult convergence of the scf cycles forced us to conclude they were beyond the scope of this thesis.

[12] Zn and Cd are stretched along the $\vec{c}$ axis to ratios of 1.88 and 1.89 respectively, whereas Sc and Y are compressed to 1.55 in PBE bulk calculations.[4]

The omission of slabs with normals lying in between the [001] direction and the {0001} plane, means one must now construct the general surface energy across an angle of 90 degrees. Equation 2.5 was never derived for such large intervals and as a result it generates surface energies which are too large. As shown in Table 4.8 for Ti, there are many planes with similar surface energies. If 2.5 were to be used, these would be overestimated by as much as 25%.

Surface	$\gamma(\frac{J}{m^2})$	Surface	$\gamma(\frac{J}{m^2})$
{0001}	1.952	$\{10\bar{1}0\}$	2.016
$\{12\bar{3}0\}$	1.88	$\{10\bar{1}1\}$	2.141
$\{12\bar{3}1\}$	2.031	$\{10\bar{1}2\}$	2.064
$\{12\bar{3}2\}$	2.088	$\{10\bar{1}3\}$	2.156

Table 4.8: A high number of different slabs for Ti has a similar surface energy, limiting the angular range for which equation 2.5 can be applied

An alternative scheme was devised to cope with this problem. The calculations for the $\{12\bar{3}1\}$ slabs were feasible for the lighter elements. As is shown in Table 4.9, the anisotropy of the surface energy is strongly dependent on the valence electron configuration. This is a justification for extrapolating the surface energy for the $\{12\bar{3}1\}$ slabs of all hcp elements via their $\{12\bar{3}0\}$ surface energy and the anisotropy of an electronically similar element for which the $\{12\bar{3}1\}$ surface energy was calculated. In a next step, the surface energies can be derived for the directions inclined 17 degrees above the $\{10\bar{1}1\}$ slab direction (indicated by green dots in Figure 4.20) can be derived by assuming them to have the same anistropy with respect to the $\{10\bar{1}0\}$ surface energies as the $\{12\bar{3}1\}$ have with respect to the $\{12\bar{3}0\}$ surface energies.

Element	$\frac{\gamma_{10\bar{1}0}}{\gamma_{0001}}$	$\frac{\gamma_{12\bar{3}0}}{\gamma_{0001}}$
Be	1.07	1.18
Mg	1.30	1.54
Y	0.97	1.01
Sc	0.95	0.99
Ti	1.03	0.96
Zr	1.05	1.05
Hf	1.08	1.07
Tc	1.14	1.20
Re	1.10	1.18
Ru	1.12	1.27
Os	1.14	1.37
Co	1.07	1.16
Zn	2.43	3.13
Cd	2.14	2.71
Tl	0.89	1.05

Table 4.9: The anisotropic character of the three slabs for which surface energies were calculated for all hcp elements, ordered by group.

At this point there are five anisotropic surface energies for each hcp element, of which the spatial distribution

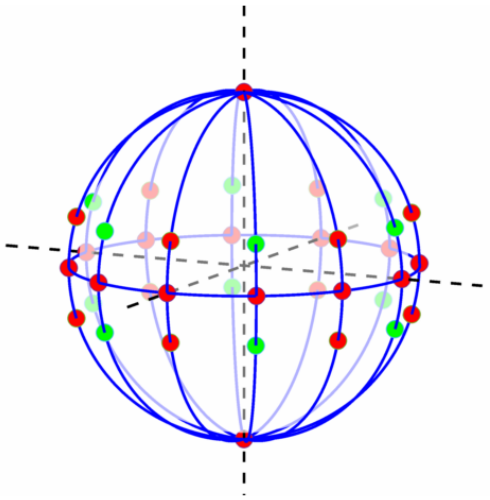

Figure 4.20: As was done for the cubic case (Figure 4.6), this figure shows the direction of normals of planes for which surface energies were calculated (red points), along with extrapolated data points - either on anisotropic grounds (green dots), using equation 2.5 (blue line in the {0001} plane) or via linear interpolation (other blue lines).

is shown in Figure 4.20. The surface energy in a general $\{10\bar{1}l\}$ or $\{12\bar{3}l\}$ direction is obtained with a linear interpolation between the three surface energies that are known in each of these planes.[13] Eventually two averages which have an azimuth distance of 30 degrees are obtained, which can be bridged with equation 2.5.

Admittedly, the derivation of the isotropic surface energy is on of the greatest difficulties in this work. It hinges on an assumed anisotropic behavior - though not without grounds - and, more importantly, uses a simple linear interpolation to obtain the average surface energy. Although this approximative method was sufficient within the limited framework of this thesis, there is definitely room for improvement when one is able to invest more time and computational resources. The determination of a polycrystalline work function was not influences by the procedure described above. The more difficult slabs never had a lower – sometimes equal to the lowest – calculated work function than any of the three simple slabs. The lowest work functions are generally found for the $\{12\bar{3}0\}$ slabs which are perpendicular to nearest neighbor lines.

4.5.2 Computational parameters and precision

As mentioned previously, the hcp is another closed packed structure like fcc. This leads to similar requirements on $\vec{k}$-point density (Table 4.10 and Table 4.1). Apart from the specific case of Mg $\{10\bar{1}0\}$, two or three free layers were always sufficient. Slab thicknesses are somewhat higher compared to the ones for fcc elements.

The precision that was attained (Table 4.11) is again somewhat better than for the bcc elements, which really

[13] One could ask the question: why all the effort for the extra data point? The surface energy does not increase enough to warrant the use of equation 2.5, but it still increases nevertheless and a simple interpolation between, say, the $\{12\bar{3}1\}$ and {0001} slab surface energy is insufficient.

Element	Slab	$\vec{k}$-points (Å^2)	Layers	Free Layers
Ti	{0001}	3300	13	2
	{10$\bar{1}$0}	6700	20	2
	{12$\bar{3}$0}	2900	15	2
Tl	{0001}	4000	16	2
	{10$\bar{1}$0}	6100	20	1
	{12$\bar{3}$0}	5900	16	3
Re	{0001}	1900	15	3
	{10$\bar{1}$0}	6100	12	2
	{12$\bar{3}$0}	1700	11	2
Mg	{0001}	3900	18	3
	{10$\bar{1}$0}	6200	16	5
	{12$\bar{3}$0}	4800	15	2

Table 4.10: Settings for the hcp test set for which work function and surface energy were deemed to be sufficiently converged.

pose the highest demands on computational settings.

		$\vec{k}$-points		Layers		Free Layers		Total	
Element	Slab	$\Delta\Phi$	$\Delta\sigma$	$\Delta\Phi$	$\Delta\sigma$	$\Delta\Phi$	$\Delta\sigma$	$\Delta\Phi$	$\Delta\sigma$
Ti	{0001}	6	0.5	6	2	3	0	9	2
	{10$\bar{1}$0}	5	2	9	4	8	1	13	5
	{110}	4	0	14	3	6	5	16	6
Tl	{0001}	6	2	30	1	3	1	31	2
	{10$\bar{1}$0}	5	3	40	8	3	0	40	9
	{110}	3	3	20	5	5	1	21	6
Re	{0001}	8	3	5	3	2	10	10	11
	{10$\bar{1}$0}	10	1	9	10	5	2	14	10
	{110}	4	6	25	8	15	10	29	14
Mg	{0001}	3	5	4	1	0	0	5	5
	{10$\bar{1}$0}	6	3	30	3	6	5	31	7
	{110}	9	0	50	5	3	4	51	6

Table 4.11: The precision associated with the settings chosen (Table 4.10) for hcp elements. Both $\Delta\Phi$ and $\Delta\sigma$ are in meV, σ being the surface energy per surface atom.

4.6 Magnetic elements

To incorporate magnetism into DFT, one must split the electron density into an "up density" and a "down density". The exchange-correlation functional must then account for the different interactions between the densities. Although magnetism is one of the success stories for GGA's[76], there are still cases where there are inconsistencies. For example the possibility of a ferromagnetic {100} surface for V caused some de-

bate[38,77], which was settled only through recent high-accuracy experiment[78][14]. In general, PBE is said to overestimate magnetism whereas LDA underestimates it. The aim of these separate discussions of the magnetic elements Ni, Fe, Cr and Co is to gain insight into the possible relation between magnetism and surface properties. The magnetism at the surface can deviate substantially from the bulk magnetism and as such might be a determining factor of the nature of the surface.

4.6.1 Nickel

Of all ground-state magnetic elements, ferromagnetic Ni has the smallest bulk magnetic moment. When the surface is created, there is a slight increase ($5-20\%$) of the magnetic moment at the surface itself. There is a quite intuitive reasoning to support this increase[79]. When neighboring atoms are removed from a top layer, translational symmetry is broken and the coordination number of the top atoms is reduced. This causes the *d* bands to narrow which enhance the paramagnetic state density.

Figure 4.21 shows that LDA results in a lower magnetic moment compared to PBE. Relative to the bulk magnetic moment however, the surface magnetism behaves very similar.

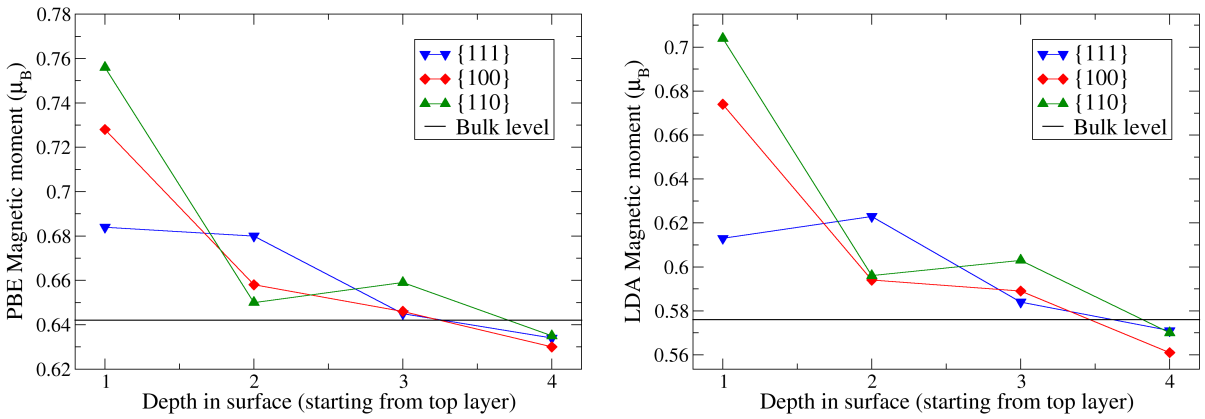

Figure 4.21: The change in the magnetic moment of Ni as a result of creating a surface.

4.6.2 Iron and Chrome

Fe has a much stronger magnetism than Ni. As it is also a less densely packed structure, the size of the magnetic moments will be interesting to chart.

Figure 4.22 shows that the increase in magnetic moment near the surface is a lot more pronounced for Fe compared to Ni. There are some discrepancies between LDA and PBE. Using the latter functional, the three different surfaces behave quite similar with respect to the bulk level. However, using LDA, the {110} and

[14]For this work, additional spin-polarized calculations were performed for V to check for surface magnetism. Only a very small insignificant magnetic moment was found ($0.007\mu_B$).

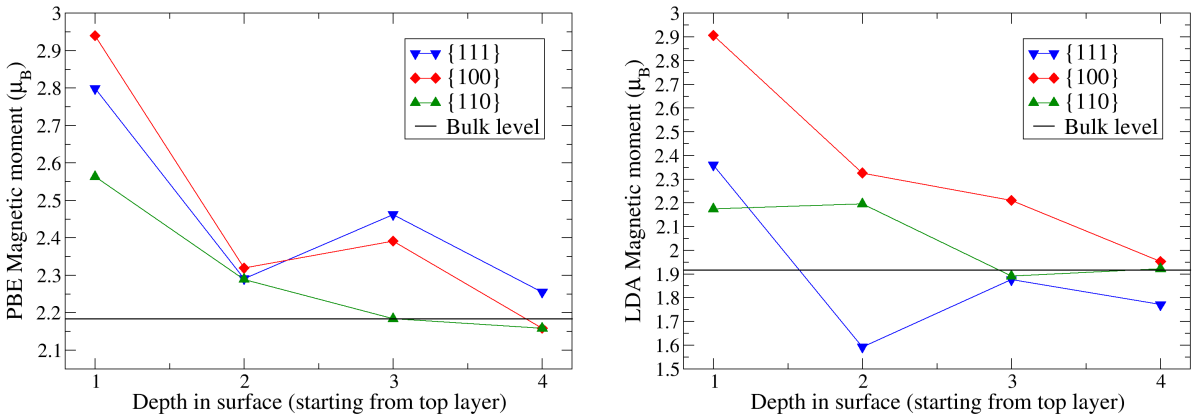

Figure 4.22: The change in the magnetic moment of Fe as a result of creating a surface.

{111} surfaces do seem to have a weaker surface magnetism compared to PBE.

Cr is quite a special case, as it is antiferromagnetic [80]. The nearest neighbors have a negative coupling with respect to magnetic moments, as they prefer to line up in opposite directions. This results in a spin-density wave (SDW) - the spatial variation of the magnetic moments - along a <100> direction. The anti-coupling is not fully opposite however, as the SDW has a period of about $21a$ (with a the lattice parameter). Because describing the exact SDW would require a unit cell 21 times as large - and an adapted code - the common choice was made to apply an SDW of one conventional unit cell.

To illustrate the surface magnetism more clearly, the *absolute values* of the magnetic moments are depicted in Figure 4.23. In the one-cell approximation of the SDW, the {100} and {111} surfaces are coupled antiferromagnetically, whereas there is in-plane antiferromagnetism in the {110} surfaces (see Figure 4.23). There is only a result for PBE, as antiferromagnetic Cr is not stable in the LDA approximation. Of all magnetic elements, Cr shows by far the largest surface magnetism, although just as for the other magnetic elements it tails off to the bulk level within a few layers of the surface.

Above $311K$ the magnetic order of Cr is lost. It might therefore be interesting to evaluate the difference in work function and surface energy with a non-magnetic DFT calculation for Cr. Both the work function and the surface energy increase for the non-magnetic case - although the {110} work function remains unaltered (see Table 4.12). From this it is clear that the absence of antiferromagnetism does not only result in a less stable bulk, but also in a less stable surface.

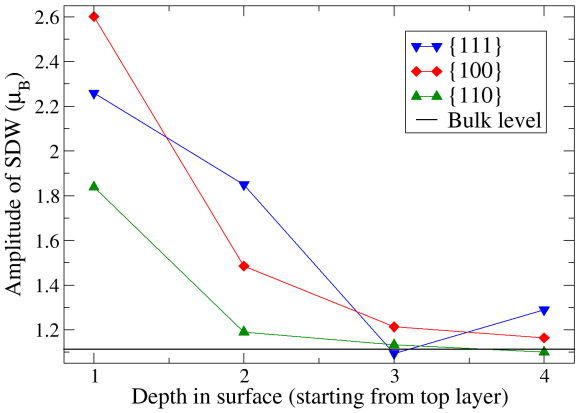

Figure 4.23: The change in the magnitude of the magnetic moment of Cr as a result of creating a surface.

	$\Phi_{AF}(eV)$	$\Phi_{NM}(eV)$	$\gamma_{AF}(\frac{J}{m^2})$	$\gamma_{NM}(\frac{J}{m^2})$
{111}	3.74	4.09	3.41	3.57
{100}	3.86	4.017	3.13	3.748
{110}	4.8	4.824	2.85	3.313

Table 4.12: Difference between the work functions and surface energies of non-magnetic and antiferromagnetic Cr.

4.6.3 Cobalt

Co has a higher bulk magnetic moment than Ni: with PBE one finds $1.632\mu_B$ compared to $0.642\mu_B$ for Ni. The impact of creating a surface is however very similar. There is a slight elevation in the magnetic moment for the top layer, which quickly drops off to the bulk level deeper into the slab (Figure 4.24).

Identically to the behavior seen in Cr and Ni, LDA and PBE show clearly different surface magnetic moments which however show similar convergence behavior towards their respective bulk values.

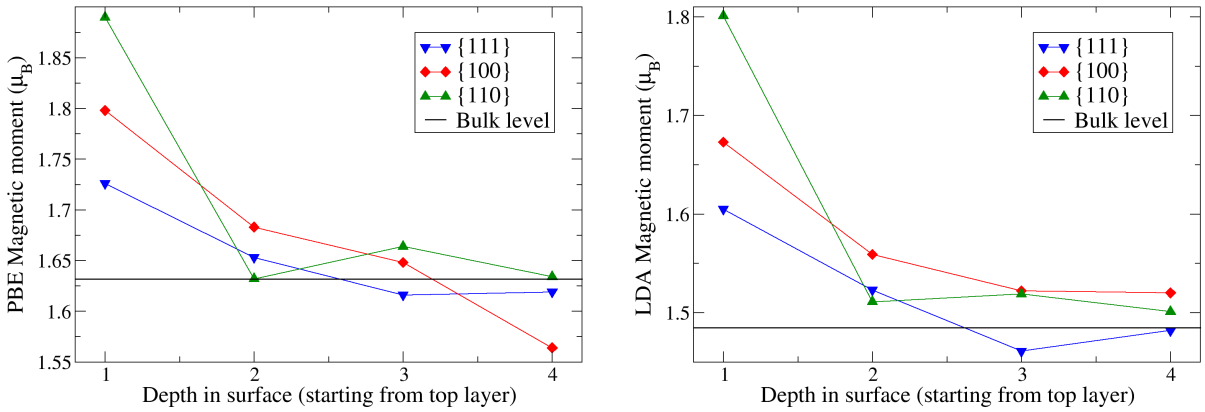

Figure 4.24: The change in the magnetic moment of Co as a result of creating a surface.

Chapter 5

Results and discussion

In this chapter the work functions and surface energies calculated with DFT – with both the LDA and PBE functional – are compared to experimental data. The goal is to evaluate how well the ab initio results *predict* the measured work functions and surface energies. The term *ideal predictor* is not limited to the case where all DFT results perfectly match the experimental data. If there is only a constant offset and a constant relative error between theory and experiment, it can be stated the theory properly describes the physics of the actual problem. The error analysis in this chapter will therefore accept a relative error and constant error and focus rather on deviations of the tested elements with respect to the general trend. This alternative approach to assessing the accuracy of DFT was put forward by Lejaeghere et al.[4] Because the statistical nuances of such an analysis are somewhat more intricate than a simple error analysis, there is a short introduction to the employed methods in the first section of this chapter. Theoretical background information for these methods can be found in *All of Nonparametric Statistics* by Wasserman[81].

5.1 Linear regression and heteroscedasticity

One could simply calculate the mean difference between ab initio and experimental result and its standard deviation, but this does not provide a lot of information about the nature of the errors. By only considering the absolute error, the inaccuracy of DFT is supposedly independent of the size of the quantity. If one puts forward the additional possibility of a relative error, the relation between the predicted value X and the experiment Y is characterized by a relative error β_1 and an absolute error β_2:

$$Y = \beta_1 X + \beta_2 \tag{5.1}$$

Performing a least-squares fit to the data set $\{X_i, Y_i\}$ is done by finding the parameters β_1 and β_2 for which the penalty function P is minimal:

$$P = \sum_i (\beta_1 X_i + \beta_2 - Y_i)^2 \tag{5.2}$$

If X' is the $N \times 2$ matrix (N being the number of data points) with one column a constant – incorporating the intercept – and the other column containing the X data, the solution to the problem is:

$$\hat{\beta} = (X'^T X')^{-1} X'^T Y \tag{5.3}$$

where the resulting 2×1 matrix $\hat{\beta}$ is the maximum-likelihood estimator for the intercept and slope.

When one has established the linear regression between experimental and theoretical values, the standard error of the regression (SER) is a measure of how well the data are approximated by the linear behavior:

$$SER = \sqrt{\frac{\sum_i^N (\beta_1 X_i + \beta_2 - Y_i)^2}{N - 2}} \tag{5.4}$$

In particular for an experiment versus DFT fit, this residual error is the size of material-dependent oscillations of the DFT values compared to the use of an ideal predictor. If there is no error on the experiment or any imprecision on the DFT calculation, a zero SER would indicate DFT accurately describes all researched materials except for a general constant and relative correction. A conceptual illustration of the SER on a regression is depicted in Figure 5.1

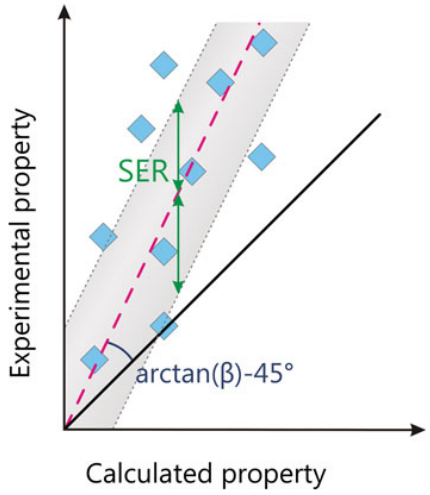

Figure 5.1: An illustration of the meaning of the SER. It is a variable, residual error on top of a systematic deviation. Image by Lejaeghere et al.[82]

The experimental errors will determine a lower boundary for the SER. Since the variance due to experiment will always be present, the expectation value for the SER is minimally one. The fitting problem becomes somewhat more involved – though the procedure remains largely equivalent – when the error is different for every X_i; this is called heteroscedasticity in statistics. This is exactly the problem for experimental surface energy and work function data. Luckily, these errors can be determined in both instances (see chapter 2 for discussion). With the knowledge of these errors $\sigma_{exp,i}$ the following penalty function determines the maximum-likelihood estimate of the regression parameters.[1]

[1]This is only true when the errors follow a Gaussian distribution. As the fluctuations on both surface energies and work functions are a caused by a multitude of non-correlated factors, one may assume this to be the case.

$$P_{weight} = \sum_i \frac{1}{\sigma^2_{exp,i}} (\beta_1 T_i + \beta_2 - X_i)^2 \tag{5.5}$$

This penalty function gives rise to a *weighted* linear regression. It does not punish an absolute deviation from experiment but rather a relative one with respect to the experimental precision. The experimental precision can even be systematically over-or underestimated. Because the weighted penalty function needs to be minimized, the absolute size of the deviations does not influence the weighted regression, as long as their ratios are well-determined. To recall the derivation of the errors: for work functions the spread in experimental data is evaluated, whereas for surface energies the uncertainties in the method – conversion from γ_{LV} to γ_{SV} and temperature extrapolation – are taken into account. Especially for the surface energies, the validity of the used standard deviation is uncertain. However, the most important aspect is they are derived in a consistent manner.

The SER is defined in the same way as for a normal linear regression but with a different penalty function. By weighting the squared residuals, the SER should be interpreted relative to the experimental error. As such, the expectation value of the SER is always equal to or larger than one, in case of equality the residual errors would only originate from the experimental errors. At this point the absolute value of the experimental deviations does become important. If it is overestimated, the SER will be too small, possibly even smaller than one. If two predictors are compared to the same set of experimental values, the SERs are of course still a viable method of comparing the predictors. Comparing the residual spread for two different samples of dependent variables is however influenced by the respective experimental data set.

5.2 Comparison between DFT and experiment

The experimental data sets have been selected to correctly incorporate their errors and to be self-consistent. As such, the analysis should be approached from a statistical perspective, focusing on the entire data set. Isolating certain elements and assessing how they stack up to experiment should be done with with careful apprehension, never ignoring the statistical relevance of the comparison.

Cr and Be are two elements which behave quite erratically. Be is overall the worst element of the entire data set. It misses the experimental mark by two to five standard deviations for both work function and surface energy, for both LDA and PBE. It is hard to pinpoint an exact reason why the DFT results should be bad. All other alkali and earth alkaline metals tend to perform really well. The result for the surface energy of Be is comparable to the surface energy found by Vitos et al.[64]. Even an all-electron FLAPW[2] calculation deviates less than $0.1 \frac{J}{m^2}$ from the presently obtained value[83]. There are strong arguments for suspecting both the experimental work function and surface energy to be wrong. According to Tyson and Miller the surface energy of Be is $1.628 \frac{J}{m^2}$, but another source claims it to be $2.7 \frac{J}{m^2}$ [84]. This latter value is significantly larger than the DFT results: $2.2 \frac{J}{m^2}$ for PBE and $2.5 \frac{J}{m^2}$ for LDA. The large difference between both experimental values raises the question whether they are accurate[3]. Concerning the large error on the work function, it originates from comparing a polycrystalline experimental work function with the lowest work

[2]FLAPW: full potential linearized augmented plane-wave. For a given exchange-correlation functional, this computational method is often regarded as a benchmark for DFT calculations using pseudopotentials or PAW potentials.

[3]The experimental surface energies of de Boer et al.[84] have not been used because the values are very similar to Tyson and Miller – except for one case: Be.

function found for Be in the DFT calculations, which is the work function for the $\{12\bar{3}0\}$ surface. There is however also an anisotropic experimental work function available for the {0001} surface[85]. For this surface, the experimental work function ($5.1eV$) is lower than the DFT work function ($5.321eV$ for PBE and $5.556eV$ for LDA), whereas the roles were reversed when comparing with the polycrystalline experimental work function. Moreover, there is also a different polycrystalline work function[86], which is almost equal to the PBE-predicted work function. As was the case for the surface energy, the large spread in the experimental data does suggest inherent difficulties in the experiments for Be, which were also reported by Green et al.[85]. Because of the large experimental deviation, it is advisable to remove the outlier.

In the case of Cr, the DFT-predicted work functions do not show extreme deviations with experiment, but the predicted surface energy does. Its value is higher than the experimental one by more than four standard deviations for both functionals – LDA performing the worst of both functionals. As Cr is the only antiferromagnetic material in the present data set, this aberration in the surface energy is most likely linked to a poor description of this magnetism, either from a DFT perspective or in the experimental derivation of the surface energy according to the Tyson and Miller protocol. In both cases, it is advisable to drop Cr from the statistical evaluation as well. The impact of not including Cr and Be in the weighted linear regression is quite big for surface energies[4]. For LDA it yields an overestimating trend of 15.5% instead of 19.9% and for PBE an underestimation of 4.4% instead of 0%.

All data for comparison with experiment are summarized in Figures 5.2, 5.3, 5.4 and 5.5. The intercepts and slopes – with resulting relative errors – are presented in Table 5.1. Whether experimental data or ab initio data should be assigned to the y-axis is an important choice. With the experimental data on the y-axis, the penalty of the fit (Equation 5.5) is the distance along the experimental axis, as it should be since DFT is the predictor for the actual experimental value, which one wishes to characterize.All regressions depicted in this chapter are performed without Cr or Be taken into account, although the data itself is still presented for both elements.

[4]Although the difference for the Cr and Be work functions is large too, the weight of this difference in the weighted linear regression is low and it has little impact on the result of the regression.

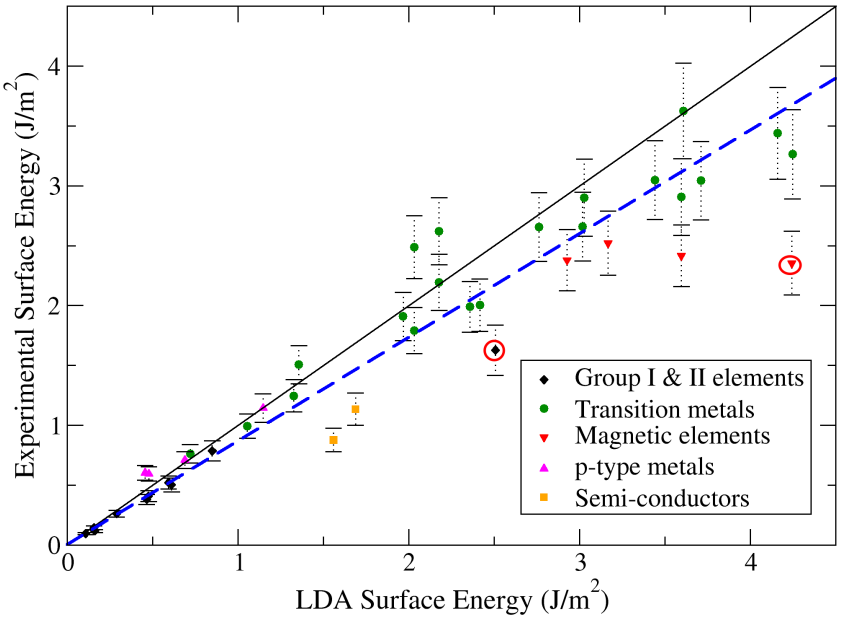

Figure 5.2: Comparison of experimental to LDA surface energies. The weighted linear regression (blue line) is compared to the bisector(black line). Be and Cr are marked with a red circle.

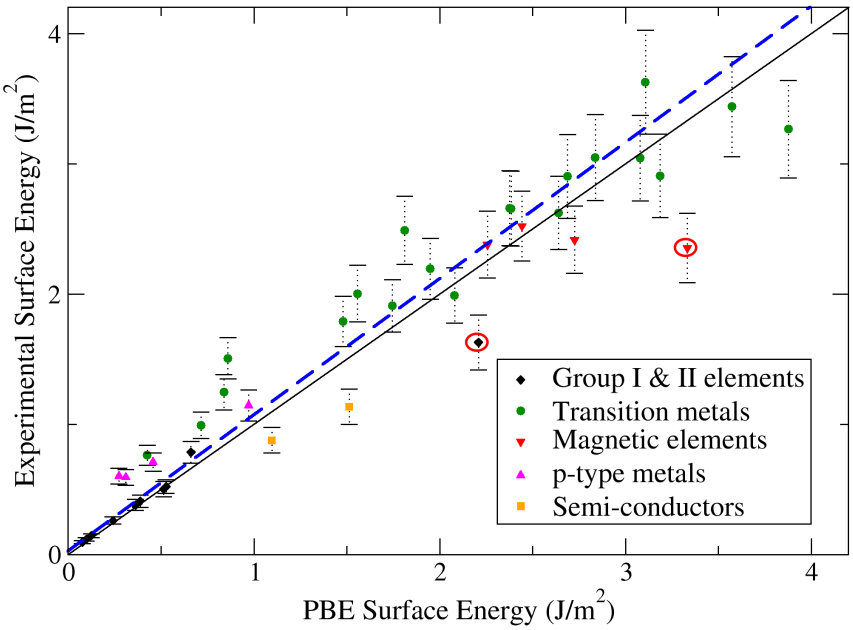

Figure 5.3: Comparison of experimental to PBE surface energies. The weighted linear regression (blue line) is compared to the bisector(black line). Be and Cr are marked with a red circle.

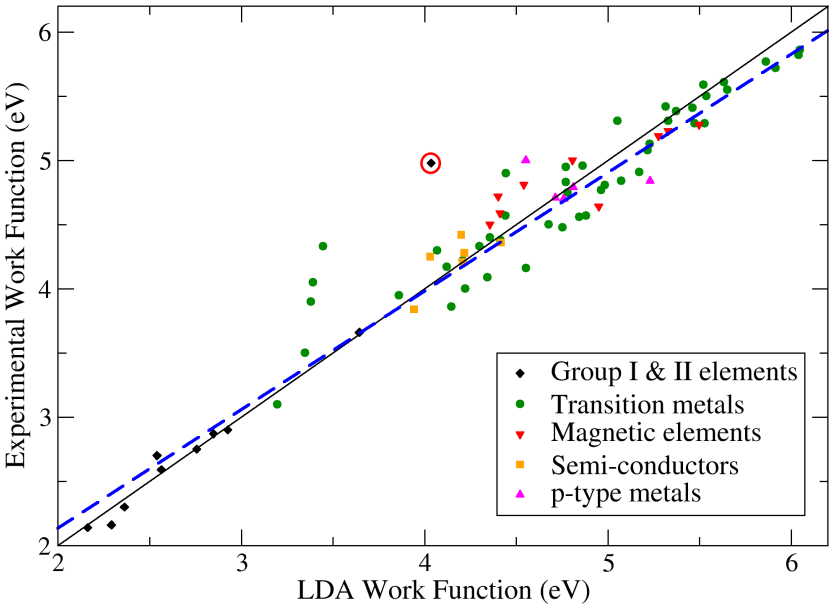

Figure 5.4: Comparison of experimental to LDA work functions. The weighted linear regression (blue line) is compared to the bisector (black line). Be is marked with a red circle.

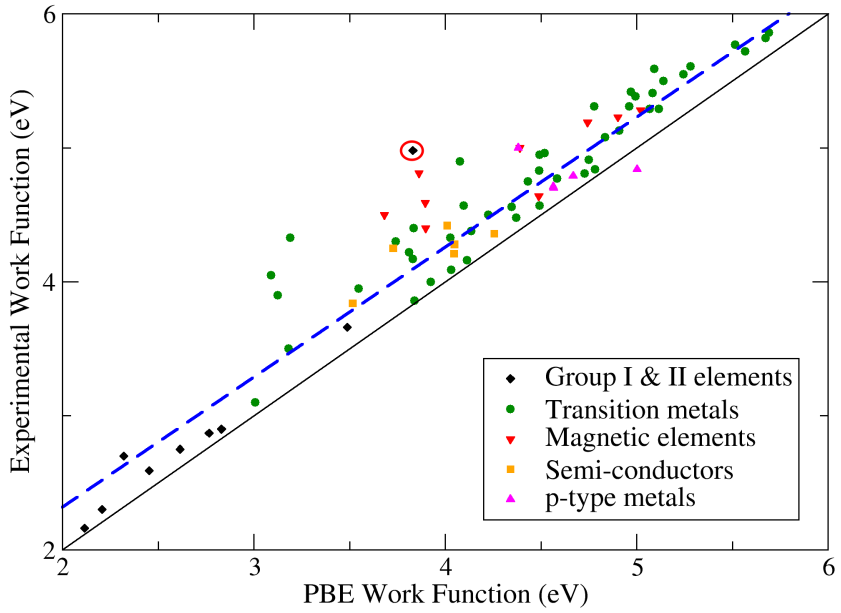

Figure 5.5: Comparison of experimental to PBE work functions. The weighted linear regression (blue line) is compared to the first bisector (black line). Be is marked with a red circle.

The error of the surface energy with regard to experiment is almost entirely of a relative nature. For both LDA and PBE the intercepts are almost zero. The LDA functional overestimates surface energies by 15% in contrast to an underestimation of 4% by PBE. However, the SER for LDA is markedly smaller compared to PBE. This suggests LDA is a better predictor for surface energy if one takes the relative error into account. The implementation of the experimental error into a weighted regression is extremely important for both LDA and PBE. Performing a regular regression yields SER values two to three times larger compared to the weighted regression.[5]

Work Function	Slope	Relative error	Offset (eV)	SER
LDA	0.924	8%	0.284	1.406
PBE	0.97	3%	0.378	1.536
Surface Energy	Slope	Relative error	Offset (J/m^2)	SER
LDA	0.866	15 %	0.003	1.651
PBE	1.046	-4%	0.024	1.95

Table 5.1: The parameters of the weighted linear fits for work function and surface energy for LDA and PBE without Cr and Be. The relative error is derived from the inverse of the slope.

The regression on the work function data renders a more complicated error image. Both LDA and PBE show a comparable offset which highlights a continuous underestimation. For LDA, this constant underestimation is mixed with a relative overestimation, visible in the linear fit in Figure 5.4, whereas PBE is largely dominated by the continuous offset. Performing a normal regression on the work function data does not result in a strongly different linear fit. Offsets increase by about $0.05eV$ while the slopes and SER values hardly change. This is some reassurance with regard to the possibility that some of the highly accurate experimental work function data – with consequently large weights – might impact the fitting too severely.

Whether the errors for work function and surface energy are correlated is an interesting question. If they were, it might point to a common cause for why modeled surfaces yield inadequate predictions. All correlation coefficients in this work are Pearson's coefficients applied to a sample, which for a data set $\{(x, y)\}$ is defined as:

$$r = r_{xy} = \frac{\sum_i (x_i - \overline{x})(y_i - \overline{y})}{\sqrt{\sum_i (x_i - \overline{x})^2}\sqrt{\sum_i (y_i - \overline{y})^2}} \tag{5.6}$$

Experimental work functions and surface energies are moderately correlated (r=0.53), which is reproduced by the DFT results (r=0.57). The errors between DFT and experiment however – both absolute and relative – are only weakly correlated ($r = -0.27$ and $r = -0.31$ respectively).

With the general trend of the LDA and PBE functionals with respect to experiment established, these results can be used to transform a work function or surface energy obtained with DFT to its expected result. As en example consider the surface energy for Be from the LDA calculation. It was argued that earlier the experimental value for Be might be wrong. By multiplying the calculated value for Be ($\gamma = 2.506\frac{J}{m^2}$) with the slope of the general trend for LDA surface energies (0.866), the expected value for the Be surface energy

[5]For comparison, the SER of the normal regression is still determined with the weights.

is obtained: $2.17 \frac{J}{m^2}$.

One might raise the question whether the relation between experimental and ab initio results is actually linear. There are two ways to evaluate this – besides a qualitative visual check. The first is the correlation coefficient between both variables, which gives a measure for linearity. A second one is to add an additional degree of freedom to the fit – a quadratic one for example – which might indicate a different relation. The latter check was carried out for all fits but it never resulted in a significantly improved SER and the quadratic term was always small. This suggest there is no higher-order term present in the behavior. The correlation coefficients between experimental and ab initio data are always higher than 0.9, also strongly suggesting a linear behavior.

To uncover possible periodic trends in the residual errors, one can simply display them for each element within a periodic table (Figures 5.6, 5.7, 5.8 and 5.9). The elements that deviate significantly from the weighted linear regression are highlighted in a darker shade. The shade is determined relative to the standard deviation of the experiment. Although Cr and Be are not taken into account for the linear regression, the residual errors for these elements are shown as well. There are some elements for which no reliable work function is available according to Michaelson[21]. These unreliable data are marked with an asterisk $^{(*)}$.

H																	He
Li	Be											B	C	N	O	F	Ne
0.09	-0.97												-0.02				
Na	Mg											Al	Si	P	S	Cl	Ar
0.08	-0.01(*)											-0.05	0.05				
K	Ca	Sc	Ti	V	Cr	Mn	Fe	Co	Ni	Cu	Zn	Ga	Ge	As	Se	Br	Kr
0.17	0.05	-0.12	-0.86	-0.26	-0.19		-0.2	-0.28	0.09	0.19	-0.3(*)		-0.5				
Rb	Sr	Y	Zr	Nb	Mo	Tc	Ru	Rh	Pd	Ag	Cd	In	Sn	Sb	Te	I	Xe
0.24	0.06	0.14	-0.63(*)	0.01	-0.02		-0.09	0.02	-0.08	0.21	-0.05(*)		-0.26(*)				
Cs	Ba	Lu	Hf	Ta	W	Re	Os	Ir	Pt	Au	Hg	Tl	Pb	Bi	Po	At	Rn
0.14	-0.07		-0.50	0.06	-0.19	-0.14	0.13	-0.1	-0.02	-0.03		0.09(*)	-0.24				

Figure 5.6: The residual error in eV for the LDA work function. A darker shade highlights badly performing elements, relative to the experimental deviation.

H																	He
Li	Be											B	C	N	O	F	Ne
0.22	-0.89												0.11				
Na	Mg											Al	Si	P	S	Cl	Ar
0.16	0.10(*)											0.09	0.2				
K	Ca	Sc	Ti	V	Cr	Mn	Fe	Co	Ni	Cu	Zn	Ga	Ge	As	Se	Br	Kr
0.22	0.19	-0.04	-0.86	-0.29	-0.55		-0.44	-0.365	0.01	0.13	-0.3(*)		-0.37				
Rb	Sr	Y	Zr	Nb	Mo	Tc	Ru	Rh	Pd	Ag	Cd	In	Sn	Sb	Te	I	Xe
0.27	0.17	0.19	-0.68(*)	0	-0.10		-0.12	-0.03	-0.12	0.07	-0.15(*)		-0.15(*)				
Cs	Ba	Lu	Hf	Ta	W	Re	Os	Ir	Pt	Au	Hg	Tl	Pb	Bi	Po	At	Rn
0.15	-0.07		-0.49	0.09	-0.17	-0.1	0.17	-0.07	0	-0.06		-0.05(*)	-0.26				

Figure 5.7: The residual error in eV for the PBE work function. A darker shade highlights badly performing elements, relative to the experimental deviation.

H																	He
Li	Be											B	C	N	O	F	Ne
-0.01	0.55																
Na	Mg											Al	Si	P	S	Cl	Ar
-0.01	-0.05											-0.15	0.33				
K	Ca	Sc	Ti	V	Cr	Mn	Fe	Co	Ni	Cu	Zn	Ga	Ge	As	Se	Br	Kr
-0.01	0.03		0.06	-0.73	1.32		0.7	0.22	0.16	-0.03	-0.08		0.48				
Rb	Sr	Y	Zr	Nb	Mo	Tc	Ru	Rh	Pd	Ag	Cd	In	Sn	Sb	Te	I	Xe
0.02	0.01		-0.2	-0.26	0.21		0.17	-0.04	0.09	-0.09	-0.14		-0.11				
Cs	Ba	Lu	Hf	Ta	W	Re	Os	Ir	Pt	Au	Hg	Tl	Pb	Bi	Po	At	Rn
0	0.02		-0.31	-0.28	0.42	-0.5	0.17	-0.07	-0.73	-2.07		-0.2	-0.18				

Figure 5.8: The residual error in $\frac{J}{m^2}$ for the LDA surface energy. A darker shade highlights badly performing elements, relative to the experimental deviation.

H																	He
Li	Be											B	C	N	O	F	Ne
0.05	0.71																
Na	Mg											Al	Si	P	S	Cl	Ar
0.02	-0.07											-0.1	0.47				
K	Ca	Sc	Ti	V	Cr	Mn	Fe	Co	Ni	Cu	Zn	Ga	Ge	As	Se	Br	Kr
0.01	0.06		0.21	0.16	1.16		0.46	0.06	0	-0.22	-0.22		0.29				
Rb	Sr	Y	Zr	Nb	Mo	Tc	Ru	Rh	Pd	Ag	Cd	In	Sn	Sb	Te	I	Xe
0.01	0.02		-0.06	-0.14	0.45		0.2	-0.15	-0.35	-0.35	-0.29		-0.21				
Cs	Ba	Lu	Hf	Ta	W	Re	Os	Ir	Pt	Au	Hg	Tl	Pb	Bi	Po	At	Rn
0.01	0.02		-0.13	-0.07	0.81	-0.35	0.32	-0.06	-0.57	-0.58		-0.29	-0.24				

Figure 5.9: The residual error in $\frac{J}{m^2}$ for the PBE surface energy. A darker shade highlights badly performing elements, relative to the experimental deviation.

Although singling out deviating elements must be done with a certain amount of apprehension because of the experimental error, there are some trends that can be observed:

- The Ti group has work functions that are too low for both LDA and PBE, although it should be noted the work function for Zr is deemed to be unreliable.
- The surface energy for Fe and Cr is significantly overestimated for both LDA and PBE and their work function is underestimated for PBE.
- Elements with almost-full or full d-shells have a surface energy below the regression line, especially the heavier elements. The underestimation is worse for PBE than for LDA.
- The p-type metals show surface energies well below the general trend.
- Ge and Si display elevated surface energies, with Ge also showing a work function significantly below the regression line.
- The heavy elements (bottom row) tend to have less accurate property predictions, especially for LDA. However these deviations are not dramatic, as they are always contained within two standard deviations.

The errors for the magnetic elements, especially large for Cr, are not surprising. Recalling the discussion on surface magnetism in the previous chapter, the error appears to be more severe for those elements with the largest surface magnetism: Cr and Fe. One of the success stories of GGA functionals is the improved description of magnetism over LDA[76], which is reflected in smaller errors for surface energy. The fact that PBE underestimates the work function and LDA produces better values is a remarkable observation.

It has already been discussed how da Silva et al.[65] found surface layer relaxations for Ti that were too large compared to LEED experiment. Their results were more recently confirmed by Singh-Miller et al.[66].[6] Although da Silva proposed hydrogen contamination to be a possible source of skewing the experimental result, this discrepancy with experiment might point to specific deficiencies of DFT simulations for the Ti group.

The problematic description of Zn and Cd within DFT is no surprise either, as electron correlation is crucial for these elements with a full d-shell[87]. The fact that LDA produces better surface energies than PBE is possibly because the overbinding of LDA compensates for the absence of dispersion interactions within DFT. In general, this bad performance of the elements in the right-hand side of the d-block and the heavier p-type metals is also reflected in a poor description of the bulk cohesive energy found by Lejaeghere et al.[4].

Both Si and Ge have reconstructed surfaces and the overestimation of the surface energy might be a consequence of DFT falling short of describing these accurately. Additionally Ge suffers from a work function that is too low.

[6] This work does not compare with experiment for surface relaxations, because results from LEED experiments often suffer from large inaccuracies; this is apparent in the research by Singh-Miller et al.

The question which functional yields better surface properties does not have a straightforward answer, as was to be expected. The SER for work functions is comparable. The fact that the systematic error on work functions for PBE is only dominated by a continuous offset might be preferable, although LDA does yield more accurate work functions. Concerning surface energies, both functionals display a purely relative systematic deviation. Although this error is larger for LDA, the SER is considerably smaller – 1.651 compared to 1.95 for PBE. This makes LDA a more suitable functional for surface energies, except for magnetic materials.

Although the VASP calculations in this work already consider scalar relativistic contributions, this might not suffice for the heavier elements. A comparison with a calculation including spin-orbit effects might indicate whether the deviations for these heavier elements are the result of this limited incorporation of relativistic effects.

When the LDA and PBE results are compared among themselves (Figures 5.10 and 5.11), a very strong linear relation is found, with a correlation coefficient of 0.99 for both surface energy and work function. A linear regression shows PBE work functions are in general 7% smaller than LDA work functions with no offset. The SER is only $0.11eV$. PBE surface energies are 15% smaller compared to LDA, with a small offset of $-0.074\frac{J}{m^2}$. The SER is somewhat larger[7] for surface energy comparison: $0.195\frac{J}{m^2}$. The largest discrepancies between LDA and PBE are – no surprises here – to be found for the magnetic elements.

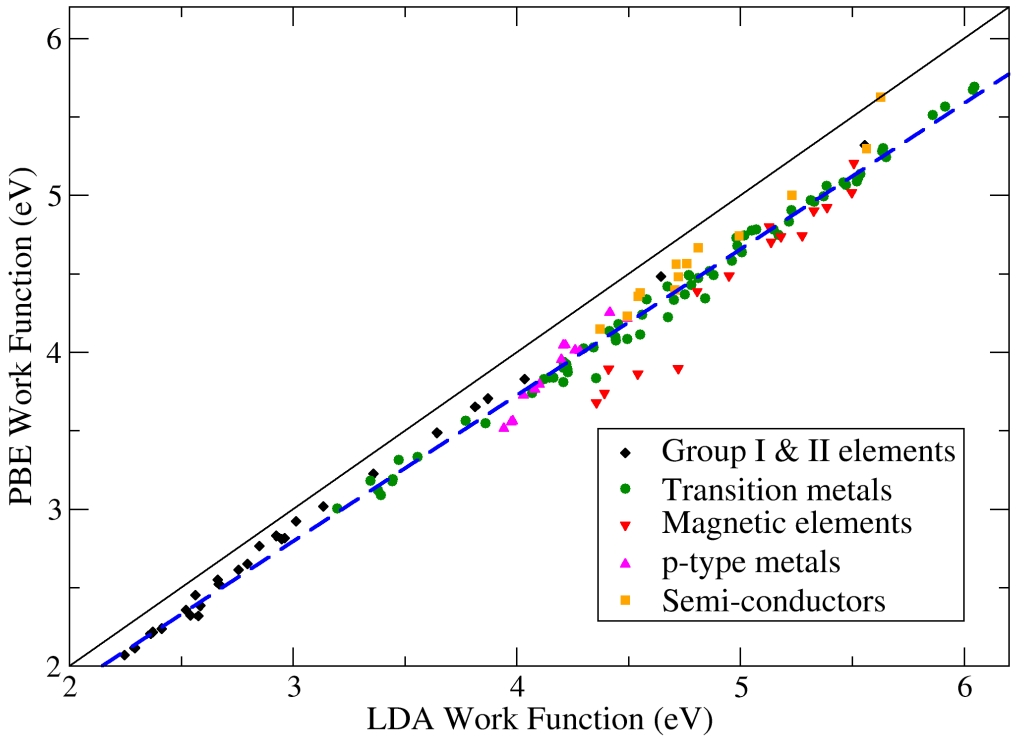

Figure 5.10: A comparison of the work function for LDA and PBE with the linear fit represented by the blue line and the bisector by a black line.

[7]This quantitative comparison is made by considering the typical size of work functions and surface energies. The former range from $2-6eV$ whereas the latter range from $0.1-4\frac{J}{m^2}$.

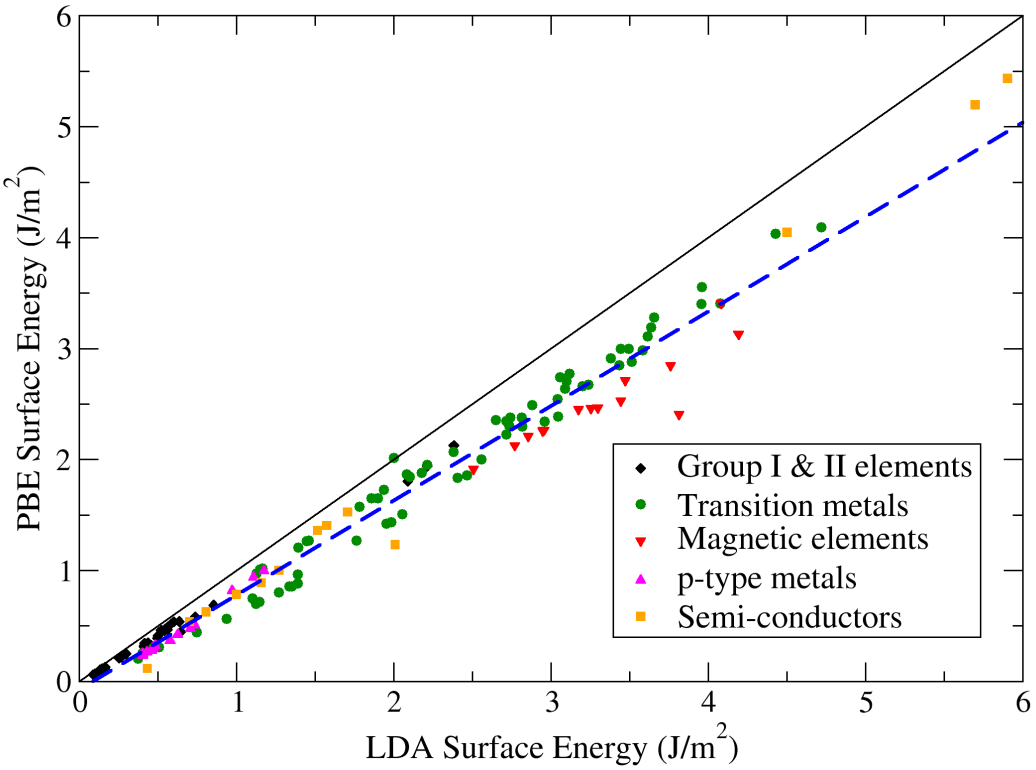

Figure 5.11: A comparison of the surface energy for LDA and PBE with the linear fit represented by the and the bisector by a black line blue line.

5.3 Correlation with bulk properties

Apart from the comparison with experiment, it is insightful to search for correlations between surface energy or work function with bulk properties. Cohesive energy, bulk modulus and atomic density are three basic properties that might reveal some insight into how the surface properties depend on the bulk properties. The bulk properties were calculated by Lejaeghere et al.[4] for the elemental crystals using PBE, where the error with respect to experiment was also evaluated. These errors themselves are interesting to compare with the errors on the surface properties as well, as it might be possible to trace back the errors on the latter to the ones on the former. As LDA and PBE results for surface properties are strongly correlated, only the PBE results will be used henceforth.

To directly compare surface properties to bulk properties, the anisotropic data from the former must be reduced to a single value; this is a problem that has been encountered before. For the present purpose this can be done in a variety of ways, provided it is done consistently so as to not skew the correlation result. To maintain uniformity in this work the same values will be used as for the comparison with experimental data: the lowest anisotropic work functions and the “isotropic” surface energies.

The most important property of a crystal is its cohesive energy. Indeed, the bonding strength of a material has an impact on almost all of its properties. For experimental results, a strong correlation between cohesive energy and surface energy is found with a correlation coefficient of 0.93. This is reproduced quite accurately

by DFT with a 0.92 correlation coefficient (Figure 5.12). This strong correlation can be understood from a simple broken bond model. When a surface is created, the atoms at the surface lose a number of neighboring atoms – and the interaction with them. If these initial bonds were strong, it will be unfavorable to generate the surface and the resulting surface energy will be high. Although both properties are strongly correlated, the – relative – inaccuracies of DFT for surface energy and cohesive energy are only moderately correlated ($r = 0.59$). This shows the cohesive energy is already a good predictor for the surface energy, but obtaining accurate surface energies is dependent on more factors than merely getting the cohesive energy right.

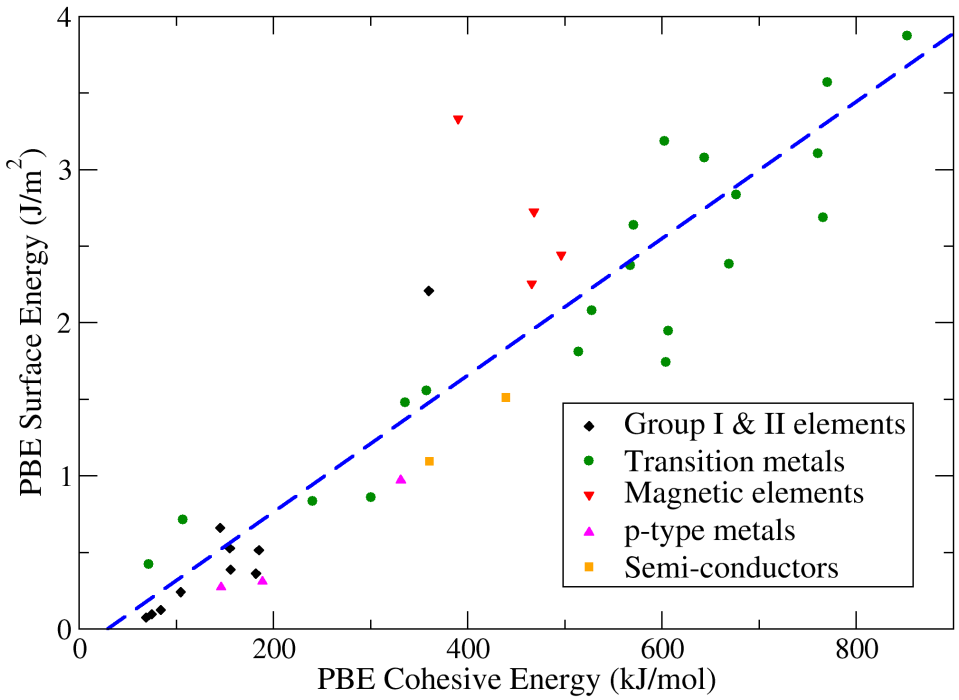

Figure 5.12: The surface energy and cohesive energy are strongly correlated. The regression line is shown in blue.

Experimental work functions only correlate weakly with cohesive energies, but the correlation becomes moderate within DFT results ($r = 0.55$). The absolute error on work function compared to experiment is also moderately correlated with the absolute error on cohesive energy ($r = 0.48$). Just as was the case for surface energy, it is not a strong indicator.

Since the bulk modulus B_0 is proportional to the cohesive energy divided by molar volume[88], the correlations with B_0 are very similar to those for cohesive energy. Moreover, it was found that Young's modulus Y_0 is proportional to the sixth power of the work function.[89] As the bulk modulus is related to Young's modulus via Poisson's ratio ν through $Y_0 = 3B_0(1 - 2\nu)$, one might expect the sixth power of the work function to be proportional to the bulk modulus as well.[8]. For experimental work functions, indeed a slightly stronger correlation ($r = 0.67$) was found between B_0 and the sixth power of the work function than for the work function itself ($r = 0.63$). Within DFT however, these roles are reversed with B_0 showing a larger correlation ($r = 0.72$) with DFT work functions than with the sixth power of the work function ($r = 0.64$). Neither the relative nor the absolute errors on the bulk modulus correlate with errors on the work function. The errors

[8]This would of course ignore a relation between the work function and Poisson's ratio.

are therefore not connected, despite the bulk modulus being a better indicator for the work function.

Both experimentally and within DFT, the negative correlation between the volume per atom and the work function is quite strong (Figure 5.13), with $r = -0.83$ and $r = -0.76$ respectively. This negative correlation explains the periodicity of the work function, as first discussed by Michaelson[21]. For elements in the same period, filling subshells leads to smaller volumes in conjunction with higher work functions. For elements in the same group, additional electrons also lead to increased volumes, once more coinciding with lower work functions. For volume *errors* however, there was no correlation with errors on the work function. The correlation between volume and surface energy is not as large ($r = -0.65$ and $r = -0.61$) as it is for work functions. The relative error on volume is however moderately correlated ($r = -0.59$) to the relative error on surface energy. This is understandable, since he surface energy is in $\frac{J}{m^2}$. If DFT predicts a volume that is too large, the surface energy will be too low.

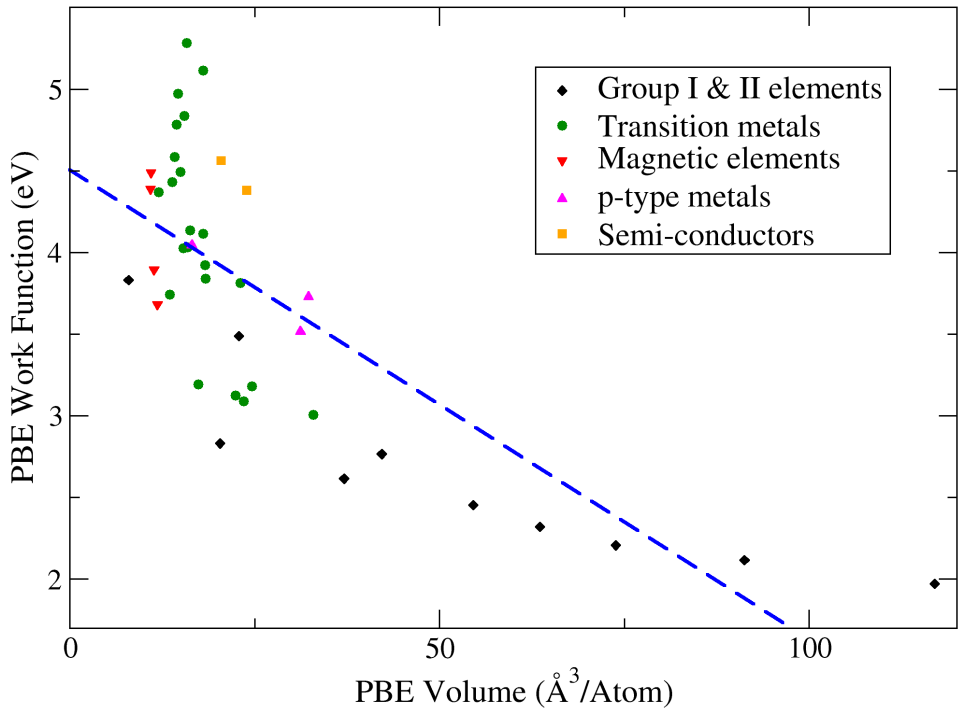

Figure 5.13: The work function and volume per atom are negatively correlated. The regression line is shown in blue.

To conclude this section which bombards the reader with correlation coefficients, there are good predictors for both surface energy and work function, i.e. cohesive energy and atomic density respectively. Robust predictors for the errors are absent however, especially for work functions; the error on the volume or cohesive energy is a moderate indicator of the error on the surface energy. This absence of a smoking gun for errors, especially for the work function, shows there are significant errors contained in DFT surface calculations, specifically associated with the electronic density found at the surface itself.

5.4 Analysis of the anisotropy

Little has been said thus far about the anisotropy of the surface energy or work function within a specific element. Indeed, comparison with experiment is troublesome as anisotropic work function data are only available for a limited number of elements. Concerning the surface energy, anisotropic information exists from the equilibrium shape of crystallites, but this is at finite temperatures making a quantitative comparison hard[90]. The goal of this section is rather to discuss the results themselves, and only for work functions will a comparison be made with experiment. Since the anisotropy of PBE and LDA is very similar, only PBE results will be discussed.

It was already explained how surface energy can be regarded as the energy required to break bonds. Within this picture, cleaving along a plane with a high planar density of atoms should be easier, since the atoms at the resulting surface have more neighbors left compared to a plane with a lower density. Following this reasoning, the expected anisotropy for the fcc elements is $\gamma_{111}<\gamma_{100}<\gamma_{110}$ whereas for the bcc elements the opposite should be true. The order for the hcp elements should be $\gamma_{0001}<\gamma_{10\bar{1}0}<\gamma_{12\bar{3}0}$. In Figure 5.14 (left), where the averages of the surface energies relative to the minimum are presented, this ranking is confirmed. There are some exceptions however. The bcc elements Li, Mo and W have the lowest energy for the {100} surfaces instead of the expected {110} surfaces. Ca and Sr slightly deviate from the trend of the fcc elements, but they have a low anisotropy. The hcp transition metals show a clearly different behavior depending on the number of electrons in the d-shell. Sc, Y and Ti break the expected anisotropy with the $\{10\bar{1}0\}$ surface having the lowest energy for Sc and Y and with Ti having the lowest surface energy for the $\{12\bar{3}0\}$ surface. Zn and Cd on the other hand do follow the normal hcp anisotropy, but with very large differences between the orientations – up to a factor 3.

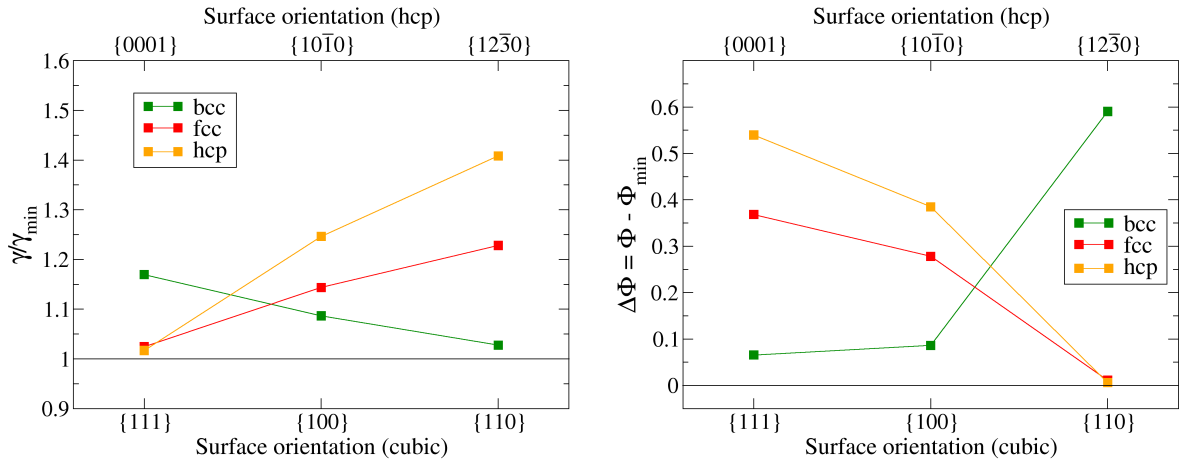

Figure 5.14: The average anisotropy of the work function and surface energy for all fcc, bcc and hcp elements. Surface energies are presented relative to the minimum, work functions by the absolute difference to the minimum.

When atoms are more closely packed at the surface, the work function is expected to be higher. This follows from the same reasoning that was made for the anisotropy of the surface energy: breaking bonds destabilizes the surface. A surface that is more densely packed, which means its atoms maintain more of their bonds, will have electrons that are more strongly bound. This idea is supported by the negative correlation between

molar volume and work function found in the previous section. Consequently, one expects the opposite order for work function anisotropy compared to the order for surface energy. In Figure 5.14 (right) this is indeed the conclusion from the average work function anisotropy for bcc, fcc and hcp. V, Nb and Mo are exceptions for the bcc trend, showing the lowest work function for the {100} surface. Cd is remarkable in that the {0001} surface has the lowest work function, as well as having the lowest surface energy. Al deviates from the fcc trend as the {110} surface has the lowest work function.

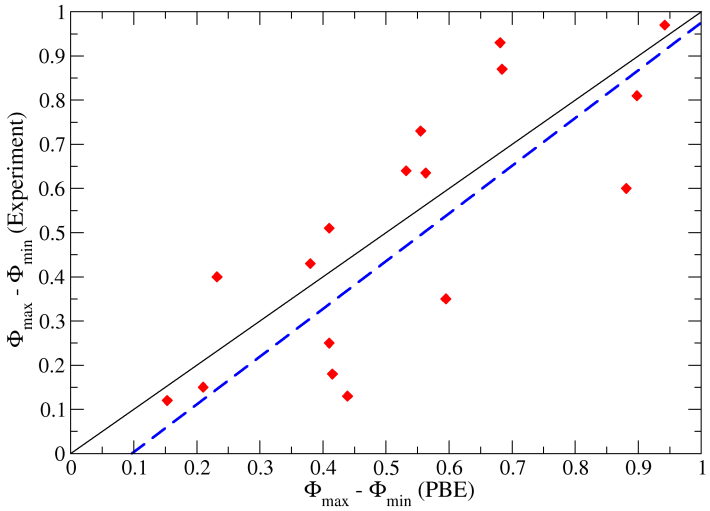

Figure 5.15: Comparison of the PBE anistropy with experiment. The linear fit is shown in blue and the bisector in black.

Figure 5.15 shows the comparison between PBE and experiment for the anisotropy of the work function, for those elements for which anisotropic data is available. Although the spread might seem large, the SER is lower than one[9], indicating PBE describes the anisotropy very well.

[9]This is either a statistical anomaly – quite possible since the sample size is not that large – or it is because the errors on experiment are correlated for the different surface orientations. To obtain the weight for the fit, the variances were summed. which would overestimate the error if the covariance were not zero.

Chapter 6

Conclusions and outlook

The goal of this thesis was to calculate work functions and surface energies for the entire periodic table with DFT-PBE and DFT-LDA and compare them to experiment. Such a large and representative test set enables a rigorous statistical approach to assess the general accuracy of DFT-predicted surface properties. This general trend serves as a guideline for how these ab initio results should be quantitatively interpreted.

A problem with previous benchmark studies on the accuracy of DFT-predicted surface energies was the comparison with experiment. By using the TLK model to deduce surface energies of random orientation, it is believed the present work makes a better comparison with the available experimental data. Moreover, the errors in the experimental methods were incorporated in the statistical comparison with DFT predictions. Concerning work functions, other DFT studies usually limited the experimental data set to the review by Michaelson.[21] By also including the recent review by Kawano[22], is not only the experimental data set enlarged, but is also a thorough quantitative understanding of the error on work function measurements established. Moreover, the protocol to compare a polycrystalline work function with the *lowest* anisotropic DFT-predicted work function is crucial to construct the test set in a statistically consistent manner.

By performing surface calculations for such a large and varied test set, a rich database was compiled, containing model parameters for surface simulations yielding converged work functions and surface energies. This can serve as a guideline for future work, providing optimal settings and a measure of precision for the three most common crystal structures: fcc, bcc and hcp. By virtue of the present computational capabilities, surfaces that showed problematic convergence with respect to model parameters, for example those with quantum size effects, were identified and rigorously tested to ensure sufficiently converged work functions and surface energies.

By using a weighted linear regression to compare DFT to experiment, a more nuanced picture is obtained with respect to the accuracy of the ab initio predictions. The surface energy is overestimated by 15% for LDA, whereas PBE underestimates it by 4%. The work functions were underestimated with a constant error of $0.38eV$ by PBE, with an additional relative overestimation of 3%. The constant error dominates this behavior. LDA work functions have a mixed error character. As is the case for PBE, there is an absolute error of – $0.28eV$ – but the relative overestimation of 8% is more significant. These systematic deviations are useful for extrapolating a specific DFT result to its expected experimental value. The material-dependent deviations with respect to the general trend are a more interesting measure for a functional's accuracy. This is quantified by the standard error on the regression (SER). From this SER, it was concluded that both LDA

and PBE predict work functions very well for most elements. Indeed, DFT-predicted work functions rival the accuracy of the experimental methods. The most notable excpetions were Ti, Zr, Hf and Ge. Predicting accurate surface energies proved a more difficult matter. These were too low for Pt, Ag, Au,Tl, Sn and Pb. The magnetic elements Fe and Cr performed very badly for the surface energy and the work function. Although LDA yields a larger systematic error for surface energy than PBE, the SER was smaller. This shows LDA is a better functional for surface energy than PBE, provided corrections are made for the systematic error.

Some clear electronic trends were observed in the residual errors. The surface energies of transition metals with full or almost-full d-shells were underestimated by both PBE and LDA. The same observation was made for the p-type metals. The work functions of the Ti group were underestimated by both functionals. The magnetic elements suffered from above-average inaccuracies as well, with their LDA-predicted work functions and PBE-predicted surface energies deviating most strongly from the general trend.

In an attempt to identify bulk properties which could predict surface properties, the Pearson correlation coefficient was evaluated between the bulk modulus, cohesive energy and the volume per atom on the one hand and the work function and surface energy on the other hand. A very strong correlation was found between cohesive energy and surface energy. In addition, work functions clearly correlated negatively with the volume per atom. The correlation between the errors with of the DFT-predicted properties with respect also evaluated. The error on the volume and the error on the cohesive energy are good predictors for the error on surface energy. No such clear markers were found for work function errors however. This indicates there is a significant inaccuracy in DFT which ins inherent to the surface calculation itself.

A first step to improving the current study would be to include those elements for which experimental data are available, as the elements with a tetragonal, rhombohedral or more exotic crystal structure are not included in the test set of this study. Calculations for Mn, Hg, B, Ga, In, As, Sb, Bi, Se and Te would greatly enrich the test set. Simulating a greater variety of surface orientations for the hexagonally close-packed elements would provide a better surface energy for these elements to compare with experimental data, as the method for deriving surface energies for general surface orientations in this work is not optimal.

Only scalar-relativistic effects were included in the present calculations. Incorporating spin-orbit effects into the calculations could improve the results for the heavier elements. This study limited itself to the use of VASP for performing the calculations. Comparing with a different software package could provide a good estimate of the numerical precision of the employed PAW method. Especially utilizing the LAPW method would be an interesting benchmark study for the surface properties obtained with VASP. It could improve the results for the heavier elements, for which both the calculated work functions and surface energies showed above-average deviations.

PBE and LDA are two functionals that have been around for some time, and as such presented an ideal starting point for this benchmark study. The inclusion of other functionals is a logical next step. A classification of which of the more advanced functionals show superior performance for which property would be of tremendous value for future ab initio surface research. In this context, work function and surface energy are of course only two properties of a surface. Especially the energetics and topology of adsorbates on a surface are very interesting properties to benchmark as well, being very relevant for surface catalysis. Such a study would require a different approach however, as adsorption on surfaces invariably focuses on a limited

number of substrates and adsorbates.

Despite the large scope for improvement of the test set and further benchmarking, a comprehensive picture is obtained for the general behavior of both work functions and surface energies with PBE and LDA. The characterization of the general trend with respect to experiment already enables a more accurate quantitative interpretation of DFT-predicted surface properties.

Bibliography

[1] N. D. Lang and W. Kohn, "Theory of Metal Surfaces: Charge Density and Surface Energy," *Physical Review B*, vol. 1, pp. 4555–4568, June 1970.

[2] N. D. Lang and W. Kohn, "Theory of Metal Surfaces: Work Function," *Physical Review B*, vol. 3, pp. 1215–1223, Feb. 1971.

[3] H. Z. G. Pilania, "Applications of modern density functional theory to surfaces and interfaces," *BOOK: A Matter of Density: Exploring the Electron Density Concept in the Chemical, Biological, and Materials Sciences*, 2011.

[4] K. Lejaeghere, V. Van Speybroeck, G. Van Oost, and S. Cottenier, "Error Estimates for Solid-State Density-Functional Theory Predictions: An Overview by Means of the Ground-State Elemental Crystals," *Critical Reviews in Solid State and Materials Sciences*, vol. 39, pp. 1–24, Oct. 2013.

[5] P. Roura and J. Fort, "Local thermodynamic derivation of Young's equation," *Journal of Colloid and Interface Science*, vol. 272, pp. 420–429, Apr. 2004.

[6] Rame-Hart, "Information on contact angle http://www.ramehart.com/contactangle.htm."

[7] C. Ozcan and N. Hasirci, "Evaluation of surface free energy for PMMA films," *Journal of Applied Polymer Science*, vol. 108, pp. 438–446, Apr. 2008.

[8] W. R. Tyson and W. A. Miller, "Surface free energies of solid metals: Estimation from liquid surface tension measurements," *Surface Science*, vol. 62, pp. 267–276, Jan. 1977.

[9] W. A. Miller and G. A. Chadwick, "On the magnitude of the solid/liquid interfacial energy of pure metals and its relation to grain boundary melting," *Acta Metallurgica*, vol. 15, pp. 607–614, Apr. 1967.

[10] L. Makkonen, "Misconceptions of the Relation between Surface Energy and Surface Tension on a Solid," *Langmuir*, vol. 30, pp. 2580–2581, Mar. 2014.

[11] J. Park, "Solid State Sintering Fundamentals http://www.slideshare.net/support.xhht/solid-state-sintering-fundamentals-242041."

[12] M. Borkin, "Surface grooving. http://soft-matter.seas.harvard.edu/index.php/Grooving_of_a_grain_boundary_b condensation_processes:_surface_evolution_below_the_roughening_transition.."

[13] W. Tyson, "Surface energies of solid metals," *Canadian Metallurgical Quarterly*, vol. 14, pp. 307–314, Oct. 1975.

[14] J. F. Nicholas, "2.1.1.5.1 The terrace-ledge-kink (TLK) model," in *Structure* (G. Chiarotti, ed.), vol. 24a, pp. 37–39, Berlin/Heidelberg: Springer-Verlag, 1993.

[15] C. Bombis, A. Emundts, M. Nowicki, and H. P. Bonzel, "Absolute surface free energies of Pb," *Surface Science*, vol. 511, pp. 83–96, June 2002.

[16] H. P. Bonzel and M. Nowicki, "Absolute surface free energies of perfect low-index orientations of metals and semiconductors," *Physical Review B*, vol. 70, p. 245430, Dec. 2004.

[17] B. E. Sundquist, "A direct determination of the anisotropy of the surface free energy of solid gold, silver, copper, nickel, and alpha and gamma iron," *Acta Metallurgica*, vol. 12, pp. 67–86, Jan. 1964.

[18] J. C. Heyraud and J. J. Metois, "Equilibrium shape of gold crystallites on a graphite cleavage surface: Surface energies and interfacial energy," *Acta Metallurgica*, vol. 28, pp. 1789–1797, Dec. 1980.

[19] J. C. Heyraud and J. J. Mtois, "Equilibrium shape and temperature; Lead on graphite," *Surface Science*, vol. 128, no. 23, pp. 334–342, 1983.

[20] J. C. Heyraud and J. J. Mtois, "Surface free energy anisotropy measurement of indium," *Surface Science*, vol. 177, pp. 213–220, Nov. 1986.

[21] H. B. Michaelson, "The work function of the elements and its periodicity," *Journal of Applied Physics*, vol. 48, pp. 4729–4733, Nov. 1977.

[22] H. Kawano, "Effective work functions for ionic and electronic emissions from mono- and polycrystalline surfaces," *Progress in Surface Science*, vol. 83, pp. 1–165, Feb. 2008.

[23] M. G. Helander, M. T. Greiner, Z. B. Wang, and Z. H. Lu, "Pitfalls in measuring work function using photoelectron spectroscopy," *Applied Surface Science*, vol. 256, pp. 2602–2605, Feb. 2010.

[24] "http://what-when-how.com/remote-sensing-from-air-and-space/energy-in-electromagnetic-waves-remote-sensing/,"

[25] S. Cottenier, "Density Functional Theory and the Family of (L)APW-methods: a step-by-step introduction.," Aug. 2013.

[26] P. Hohenberg and W. Kohn, "Inhomogeneous Electron Gas," *Physical Review*, vol. 136, pp. B864–B871, Nov. 1964.

[27] W. Kohn and L. Sham, "Self-Consistent Equations Including Exchange and Correlation Effects," *Physical Review*, vol. 140, no. 4A, pp. 1133–&, 1965. WOS:A19657000000015.

[28] J. P. Perdew and A. Zunger, "Self-interaction correction to density-functional approximations for many-electron systems," *Physical Review B*, vol. 23, pp. 5048–5079, May 1981.

[29] A. D. Becke, "Density-functional exchange-energy approximation with correct asymptotic behavior," *Physical Review A*, vol. 38, pp. 3098–3100, Sept. 1988.

[30] C. Lee, W. Yang, and R. G. Parr, "Development of the Colle-Salvetti correlation-energy formula into a functional of the electron density," *Physical Review B*, vol. 37, pp. 785–789, Jan. 1988.

[31] J. P. Perdew, "Density-functional approximation for the correlation energy of the inhomogeneous electron gas," *Physical Review B*, vol. 33, pp. 8822–8824, June 1986.

[32] J. P. Perdew, J. A. Chevary, S. H. Vosko, K. A. Jackson, M. R. Pederson, D. J. Singh, and C. Fiolhais, "Atoms, molecules, solids, and surfaces: Applications of the generalized gradient approximation for exchange and correlation," *Physical Review B*, vol. 46, pp. 6671–6687, Sept. 1992.

[33] J. P. Perdew, K. Burke, and M. Ernzerhof, "Generalized Gradient Approximation Made Simple," *Physical Review Letters*, vol. 77, pp. 3865–3868, Oct. 1996.

[34] J. P. Perdew, K. Burke, and M. Ernzerhof, "Generalized Gradient Approximation Made Simple [Phys. Rev. Lett. 77, 3865 (1996)]," *Physical Review Letters*, vol. 78, pp. 1396–1396, Feb. 1997.

[35] Wikimedia, "Wikipedia content http://commons.wikimedia.org/wiki/File:Sketch_pseudopotentials.png."

[36] P. E. Blöchl, "Projector augmented-wave method," *Physical Review B*, vol. 50, pp. 17953–17979, Dec. 1994.

[37] G. Kresse and D. Joubert, "From ultrasoft pseudopotentials to the projector augmented-wave method," *Physical Review B*, vol. 59, pp. 1758–1775, Jan. 1999.

[38] G. Kresse, W. Bergermayer, and R. Podloucky, "Comment on "Magnetism of the V(001) surface: Contradictory results from pseudopotential and linearized augmented plane-wave calculations"," *Physical Review B*, vol. 66, p. 146401, Oct. 2002.

[39] G. Kresse and J. Hafner, "Ab initio molecular dynamics for liquid metals," *Physical Review B*, vol. 47, pp. 558–561, Jan. 1993.

[40] G. Kresse and J. Hafner, "Ab initio molecular-dynamics simulation of the liquid-metal/amorphous-semiconductor transition in germanium," *Physical Review B*, vol. 49, pp. 14251–14269, May 1994.

[41] G. Kresse and J. Furthmüller, "Efficiency of ab-initio total energy calculations for metals and semiconductors using a plane-wave basis set," *Computational Materials Science*, vol. 6, pp. 15–50, July 1996.

[42] G. Kresse and J. Furthmüller, "Efficient iterative schemes for *ab initio* total-energy calculations using a plane-wave basis set," *Physical Review B*, vol. 54, pp. 11169–11186, Oct. 1996.

[43] G. Kresse, M. Marsman, and J. Furthmüller, "VASP the GUIDE," Mar. 2015.

[44] P. Pulay, "Convergence acceleration of iterative sequences. the case of scf iteration," *Chemical Physics Letters*, vol. 73, pp. 393–398, July 1980.

[45] G. P. Kerker, "Efficient iteration scheme for self-consistent pseudopotential calculations," *Physical Review B*, vol. 23, pp. 3082–3084, Mar. 1981.

[46] P. E. Blöchl, O. Jepsen, and O. K. Andersen, "Improved tetrahedron method for Brillouin-zone integrations," *Physical Review B*, vol. 49, pp. 16223–16233, June 1994.

[47] M. Methfessel, D. Hennig, and M. Scheffler, "Trends of the surface relaxations, surface energies, and work functions of the 4d transition metals," *Physical Review B*, vol. 46, pp. 4816–4829, Aug. 1992.

[48] S. Curtarolo, W. Setyawan, G. L. W. Hart, M. Jahnatek, R. V. Chepulskii, R. H. Taylor, S. Wang, J. Xue, K. Yang, O. Levy, M. J. Mehl, H. T. Stokes, D. O. Demchenko, and D. Morgan, "AFLOW: An automatic framework for high-throughput materials discovery," *Computational Materials Science*, vol. 58, pp. 218–226, June 2012.

[49] T. Lianheng, "http://www.hector.ac.uk/cse/distributedcse/reports/conquest/conquest/node6.html."

[50] A. A. Stekolnikov, J. Furthmüller, and F. Bechstedt, "Absolute surface energies of group-IV semiconductors: Dependence on orientation and reconstruction," *Physical Review B*, vol. 65, p. 115318, Feb. 2002.

[51] J. C. Boettger, "Nonconvergence of surface energies obtained from thin-film calculations," *Physical Review B*, vol. 49, pp. 16798–16800, June 1994.

[52] V. Fiorentini and M. Methfessel, "Extracting convergent surface energies from slab calculations," *Journal of Physics: Condensed Matter*, vol. 8, p. 6525, Sept. 1996.

[53] A. D. Laurent and D. Jacquemin, "TD-DFT benchmarks: A review," *International Journal of Quantum Chemistry*, vol. 113, pp. 2019–2039, Sept. 2013.

[54] C. J. Fall, N. Binggeli, and A. Baldereschi, "Deriving accurate work functions from thin-slab calculations," *Journal of Physics: Condensed Matter*, vol. 11, p. 2689, Apr. 1999.

[55] C. Tuma, A. D. Boese, and N. C. Handy, "Predicting the binding energies of H-bonded complexes: A comparative DFT study," *Physical Chemistry Chemical Physics*, vol. 1, pp. 3939–3947, Jan. 1999.

[56] Y. Zhao and D. G. Truhlar, "Benchmark Databases for Nonbonded Interactions and Their Use To Test Density Functional Theory," *Journal of Chemical Theory and Computation*, vol. 1, pp. 415–432, May 2005.

[57] S. F. Sousa, P. A. Fernandes, and M. J. Ramos, "General Performance of Density Functionals," *The Journal of Physical Chemistry A*, vol. 111, pp. 10439–10452, Oct. 2007.

[58] L. Goerigk and S. Grimme, "A thorough benchmark of density functional methods for general main group thermochemistry, kinetics, and noncovalent interactions," *Physical Chemistry Chemical Physics*, vol. 13, pp. 6670–6688, Apr. 2011.

[59] M. Korth and S. Grimme, "Mindless DFT Benchmarking," *Journal of Chemical Theory and Computation*, vol. 5, pp. 993–1003, Apr. 2009.

[60] B. Grabowski, T. Hickel, and J. Neugebauer, "Ab initio study of the thermodynamic properties of nonmagnetic elementary fcc metals: Exchange-correlation-related error bars and chemical trends," *Physical Review B*, vol. 76, p. 024309, July 2007.

[61] M. Ropo, K. Kokko, and L. Vitos, "Assessing the Perdew-Burke-Ernzerhof exchange-correlation density functional revised for metallic bulk and surface systems," *Physical Review B*, vol. 77, p. 195445, May 2008.

[62] P. Haas, F. Tran, and P. Blaha, "Calculation of the lattice constant of solids with semilocal functionals," *Physical Review B*, vol. 79, p. 085104, Feb. 2009.

[63] A. Stroppa and G. Kresse, "The shortcomings of semi-local and hybrid functionals: what we can learn from surface science studies," *New Journal of Physics*, vol. 10, p. 063020, June 2008.

[64] L. Vitos, A. V. Ruban, H. L. Skriver, and J. Kollr, "The surface energy of metals," *Surface Science*, vol. 411, pp. 186–202, Aug. 1998.

[65] J. L. F. Da Silva, C. Stampfl, and M. Scheffler, "Converged properties of clean metal surfaces by all-electron first-principles calculations," *Surface Science*, vol. 600, pp. 703–715, Feb. 2006.

[66] N. E. Singh-Miller and N. Marzari, "Surface energies, work functions, and surface relaxations of low-index metallic surfaces from first principles," *Physical Review B*, vol. 80, p. 235407, Dec. 2009.

[67] J. Wang and S.-Q. Wang, "Surface energy and work function of fcc and bcc crystals: Density functional study," *Surface Science*, vol. 630, pp. 216–224, Dec. 2014.

[68] H. W. Hugosson, O. Eriksson, U. Jansson, and I. A. Abrikosov, "Surface segregation of transition metal impurities on the TiC(1 0 0) surface," *Surface Science*, vol. 585, pp. 101–107, July 2005.

[69] S. Kurth, J. P. Perdew, and P. Blaha, "Molecular and solid-state tests of density functional approximations: LSD, GGAs, and meta-GGAs," *International Journal of Quantum Chemistry*, vol. 75, pp. 889–909, Jan. 1999.

[70] M. Hupalo, S. Kremmer, V. Yeh, L. Berbil-Bautista, E. Abram, and M. C. Tringides, "Uniform island height selection in the low temperature growth of Pb/Si(1 1 1)-(77)," *Surface Science*, vol. 493, pp. 526–538, Nov. 2001.

[71] M. Hupalo, V. Yeh, L. Berbil-Bautista, S. Kremmer, E. Abram, and M. C. Tringides, "Uniform-height island growth of Pb on Si(111)-Pb ($\sqrt{3} \times \sqrt{3}$) at low temperatures," *Physical Review B*, vol. 64, p. 155307, Sept. 2001.

[72] C. M. Wei and M. Y. Chou, "Theory of quantum size effects in thin Pb(111) films," *Physical Review B*, vol. 66, p. 233408, Dec. 2002.

[73] J. Furthmüller, J. Hafner, and G. Kresse, "Structural and Electronic Properties of Clean and Hydrogenated Diamond (100) Surfaces," *EPL (Europhysics Letters)*, vol. 28, p. 659, Dec. 1994.

[74] H. E. Farnsworth, R. E. Schlier, and J. A. Dillon Jr., "Surface-structure and work-function determinations for Silicon crystals," *Journal of Physics and Chemistry of Solids*, vol. 8, pp. 116–118, Jan. 1959.

[75] D. Sherman, "Energy considerations in crack deflection phenomenon in single crystal silicon," *International Journal of Fracture*, vol. 140, pp. 125–140, July 2006.

[76] T. C. Leung, C. T. Chan, and B. N. Harmon, "Ground-state properties of Fe, Co, Ni, and their monoxides: Results of the generalized gradient approximation," *Physical Review B*, vol. 44, pp. 2923–2927, Aug. 1991.

[77] I. G. Batyrev, J.-H. Cho, and L. Kleinman, "Magnetism of the V(001) surface: Contradictory results from pseudopotential and linearized augmented plane-wave calculations," *Physical Review B*, vol. 63, p. 172420, Apr. 2001.

[78] D. Lacina, J. Yang, and J. L. Erskine, "Multilayer relaxation and search for ferromagnetic order at the (100) surface of bulk paramagnetic vanadium," *Physical Review B*, vol. 75, p. 195423, May 2007.

[79] M. Alde´n, S. Mirbt, H. L. Skriver, N. M. Rosengaard, and B. Johansson, "Surface magnetism in iron, cobalt, and nickel," *Physical Review B*, vol. 46, pp. 6303–6312, Sept. 1992.

[80] R. Soulairol, C.-C. Fu, and C. Barreteau, "Magnetic and energetic properties of low-index Cr surfaces and Fe/Cr interfaces: A first-principles study," *Physical Review B*, vol. 84, p. 155402, Oct. 2011.

[81] L. Wasserman, *All of Nonparametric Statistics*. New York: Springer, May 2007.

[82] K. Lejaeghere, J. Jaeken, V. Van Speybroeck, and S. Cottenier, "*Ab initio* based thermal property predictions at a low cost: An error analysis," *Physical Review B*, vol. 89, p. 014304, Jan. 2014.

[83] P. J. Feibelman, "First-principles calculation of the geometric and electronic structure of the Be(0001) surface," *Physical Review B*, vol. 46, pp. 2532–2539, July 1992.

[84] F. R. d. Boer, R. Boom, W. C. M. Mattens, A. R. Miedema, and A. K. Niessen, *Cohesion in Metals: Transition Metal Alloys*. Amsterdam: North Holland, May 1989.

[85] A. K. Green and E. Bauer, "Work function and purity of the Beryllium (0001) surface," *Surface Science*, vol. 74, pp. 676–681, June 1978.

[86] V. S. Fomenko and G. V. Samsonov, "Chemical Elements," in *Handbook of Thermionic Properties* (V. S. Fomenko and G. V. Samsonov, eds.), pp. 5–68, Springer US, 1974.

[87] N. Gaston, D. Andrae, B. Paulus, U. Wedig, and M. Jansen, "Understanding the hcp anisotropy in Cd and Zn: the role of electron correlation in determining the potential energy surface," *Physical Chemistry Chemical Physics*, vol. 12, pp. 681–687, Dec. 2009.

[88] S. Wacke, T. Górecki, C. Górecki, and K. Ksiażek, "Relations between the cohesive energy, atomic volume, bulk modulus and sound velocity in metals," *Journal of Physics: Conference Series*, vol. 289, p. 012020, Apr. 2011.

[89] G. Hua and D. Li, "Generic relation between the electron work function and Young's modulus of metals," *Applied Physics Letters*, vol. 99, p. 041907, July 2011.

[90] D. Yu, H. Bonzel, and M. Scheffler, "Orientation-dependent surface and step energies of Pb from first principles," *Physical Review B*, vol. 74, p. 115408, Sept. 2006.

Appendix A

Experimental data

All experimental data that were used in this work are bundled in this appendix. Work functions for which only one experimental value was found were assigned an error of $0.32eV$. Those that were deemed unreliable by Michaelson[21] have been indicated with an asterisk $^{(*)}$.

	$\Phi(eV)$	$\gamma(\frac{J}{m^2})$		$\Phi(eV)$	$\gamma(\frac{J}{m^2})$
Li	2.9 ± 0.32	0.522 ± 0.05	Ir	5.27 ± 0.32	3.048 ± 0.33
Na	2.75 ± 0.32	0.261 ± 0.03	Ir {111}	5.77 ± 0.03	
K	2.3 ± 0.32	0.145 ± 0.02	Ir {100}	5.72 ± 0.25	
Rb	2.16 ± 0.32	0.117 ± 0.01	Ir {110}	5.42 ± 0.32	
Cs	2.14 ± 0.32	0.095 ± 0.01	Ni	4.87 ± 0.25	2.38 ± 0.26
Be	4.98 ± 0.32	1.628 ± 0.21	Ni {111}	5.28 ± 0.14	
Mg	3.66 $^{(*)}$	0.785 ± 0.08	Ni {100}	5.23 ± 0.2	
Ca	2.87 ± 0.32	0.502 ± 0.06	Ni {110}	4.64 ± 0.17	
Sr	2.59 ± 0.32	0.409 ± 0.05	Pd	5.24 ± 0.31	2.003 ± 0.22
Ba	2.7 ± 0.32	0.38 ± 0.04	Pd {111}	5.55 ± 0.2	
Sc	3.500 ± 0.32		Pd {100}	5.59 ± 0.26	
Y	3.100 ± 0.32		Pd {110}	5.08 ± 0.23	
Ti	4.330 ± 0.32	1.989 ± 0.21	Pt	5.27 ± 0.26	2.489 ± 0.26
Zr	4.050 $^{(*)}$	1.909 ± 0.2	Pt {111}	5.86 ± 0.18	
Hf	3.900 ± 0.32	2.193 ± 0.23	Pt {100}	5.82 ± 0.13	
V	4.3 ± 0.32	2.622 ± 0.28	Pt{110}	5.61 ± 0.2	
Nb	4.02 ± 0.18	2.655 ± 0.29	Cu	4.51 ± 0.14	1.79 ± 0.19
Nb {111}	3.86 ± 0.33		Cu {111}	4.91 ± 0.05	
Nb {100}	3.95 ± 0.12		Cu {100}	4.57 ± 0.09	
Nb {110}	4.83 ± 0.14		Cu {110}	4.48 ± 0.2	
Ta	4.25 ± 0.06	2.902 ± 0.32	Ag	4.36 ± 0.26	1.246 ± 0.13
Ta {111}	4 ± 0.07		Ag {111}	4.56 ± 0.11	
Ta {100}	4.17 ± 0.32		Ag {100}	4.5 ± 0.32	
Ta {110}	4.81 ± 0.16		Ag {110}	4.16 ± 0.26	
Cr	4.5 ± 0.32	2.354 ± 0.27	Au	5.31 ± 0.24	1.506 ± 0.16
Mo	4.6 ± 0.16	2.907 ± 0.32	Au {111}	5.29 ± 0.11	
Mo {111}	4.09 ± 0.23		Au {100}	5.41 ± 0.32	
Mo {100}	4.4 ± 0.13		Au {110}	5.31 ± 0.32	

	$\Phi(eV)$	$\gamma(\frac{J}{m^2})$		$\Phi(eV)$	$\gamma(\frac{J}{m^2})$
Mo {110}	4.96 ± 0.11		Zn	$4.33^{(*)}$	0.993 ± 0.1
W	4.55 ± 0.05	3.265 ± 0.37	Zn {0001}	4.9 ± 0.32 ±	
W {111}	4.38 ± 0.12		Cd	$4.22^{(*)}$	0.762 ± 0.08
W {100}	4.57 ± 0.13		Al	4.23 ± 0.44	1.143 ± 0.12
W {110}	5.31 ± 0.32		Al {111}	4.28 ± 0.11	
Re	4.95 ± 0.13	3.626 ± 0.40	Al {100}	4.36 ± 0.32	
Re {0001}	5.13 ± 0.12		Al {110}	4.21 ± 0.15	
Fe	4.66 ± 0.21	2.417 ± 0.26	Tl	$3.84^{(*)}$	0.602 ± 0.06
Fe {111}	4.81 ± 0.32		C {0001}	4.7 ± 0.1	
Fe {100}	4.59 ± 0.26		Si	4.6 ± 0.28	1.135 ± 0.14
Fe {110}	5.19 ± 0.06		Si {111}	4.79 ± 0.15	
Fe-γ	4.72 ± 0.25		Si {100}	4.71 ± 0.08	
Ru	4.75 ± 0.19	3.043 ± 0.33	Si {110}	4.84 ± 0.1	
Ru {0001}	5.385 ± 0.15		Ge	5.00 ± 0.32	0.877 ± 0.1
Os	4.84 ± 0.07	3.439 ± 0.38	Sn	$4.42^{(*)}$	0.709 ± 0.07
Co	5 ± 0.32	2.522 ± 0.27	Pb	4.25 ± 0.32	0.593 ± 0.06
Rh	4.9 ± 0.32	2.659 ± 0.29			
Rh {111}	5.5 ± 0.14				
Rh {100}	5.29 ± 0.14				
Rh {110}	4.77 ± 0.08				

Appendix B

Results from the calculations

		$\vec{k}$-mesh	Layers in slab	Free layers	$\Phi_{PBE}(eV)$	$\Phi_{LDA}(eV)$	$\gamma_{PBE}(\frac{J}{m^2})$	$\gamma_{LDA}(\frac{J}{m^2})$
Li	{111}	31x31	22	4	2.83	2.925	0.537	0.599
	{100}	39x39	19	1	3.018	3.135	0.463	0.52
	{110}	47x47	15	1	3.225	3.359	0.493	0.561
Na	{111}	25x25	22	4	2.614	2.756	0.249	0.295
	{100}	33x33	19	1	2.651	2.796	0.221	0.264
	{110}	39x39	15	1	2.815	2.962	0.21	0.253
K	{111}	27x27	22	4	2.206	2.362	0.13	0.162
	{100}	21x21	16	1	2.217	2.372	0.116	0.145
	{110}	33x33	15	1	2.358	2.52	0.106	0.133
Rb	{111}	19x19	22	4	2.118	2.291	0.101	0.166
	{100}	25x25	19	1	2.115	2.291	0.091	0.151
	{110}	29x29	15	1	2.239	2.412	0.081	0.134
Cs	{111}	19x19	22	4	1.978	2.168	0.08	0.113
	{100}	25x25	19	1	1.97	2.161	0.072	0.101
	{110}	21x21	15	1	2.07	2.245	0.061	0.087
Be	{0001}	21x21	18	3	5.321	5.556	1.803	2.089
	$\{10\bar{1}0\}$	29x17	20	2	4.484	4.644	1.938	2.211
	$\{12\bar{3}0\}$	17x17	15	2	3.83	4.035	2.128	2.381
	$\{12\bar{3}1\}$	21x21	20	5	4.482	4.679	2.461	2.751
Mg	{0001}	21x21	18	3	3.705	3.871	0.448	0.644
	$\{10\bar{1}0\}$	25x25	16	5	3.652	3.814	0.581	0.736
	$\{12\bar{3}0\}$	13x13	15	2	3.487	3.643	0.688	0.853
Ca	{111}	19x19	15	3	2.923	3.012	0.465	0.56
	{100}	19x19	17	3	2.765	2.848	0.458	0.539
	{110}	21x13	15	3	2.81	2.949	0.54	0.634
Sr	{111}	15x15	13	3	2.522	2.668	0.35	0.437
	{100}	15x15	13	4	2.452	2.563	0.346	0.414
	{110}	21x13	13	3	2.55	2.663	0.41	0.498
Ba	{111}	21x21	22	4	2.319	2.575	0.39	0.495
	{100}	27x27	19	1	2.323	2.54	0.321	0.412

		$\vec{k}$-mesh	Layers in slab	Free layers	$\Phi_{PBE}(eV)$	$\Phi_{LDA}(eV)$	$\gamma_{PBE}(\frac{J}{m^2})$	$\gamma_{LDA}(\frac{J}{m^2})$
	{110}	33x33	15	1	2.385	2.584	0.313	0.41
Sc	{0001}	21x21	18	3	3.334	3.556	1.271	1.458
	$\{10\bar{1}0\}$	29x17	20	2	3.563	3.772	1.207	1.391
	$\{12\bar{3}0\}$	13x13	15	2	3.18	3.346	1.264	1.445
	$\{12\bar{3}1\}$	21x21	20	5	3.416	3.389	1.385	1.584
Y	{0001}	21x21	18	3	3.178	3.443	1.007	1.148
	$\{10\bar{1}0\}$	29x17	20	2	3.315	3.471	0.974	1.126
	$\{12\bar{3}0\}$	13x13	15	2	3.005	3.196	1.017	1.164
Ti	{0001}	21x21	13	2	4.42	4.674	1.952	2.211
	$\{10\bar{1}0\}$	29x17	20	2	3.896	4.226	2.016	2
	$\{12\bar{3}0\}$	11x11	15	3	3.19	3.446	1.88	2.176
	$\{12\bar{3}1\}$	19x19	12	3	3.512	3.797	2.031	2.32
Zr	{0001}	21x21	18	3	4.179	4.455	1.576	1.782
	$\{10\bar{1}0\}$	29x17	20	2	3.837	4.164	1.65	1.856
	$\{12\bar{3}0\}$	13x13	15	2	3.089	3.391	1.651	1.898
Hf	{0001}	21x21	14	3	4.339	4.581	1.726	1.937
	$\{10\bar{1}0\}$	29x17	20	2	3.939	4.207	1.867	2.081
	$\{12\bar{3}0\}$	13x13	15	2	3.123	3.378	1.845	2.101
V	{111}	23x23	22	3	3.872	4.227	2.705	3.098
	{100}	27x27	18	1	3.741	4.068	2.38	2.815
	{110}	35x35	13	1	4.744	5.017	2.379	2.74
Nb	{111}	25x25	25	4	3.838	4.146	2.345	2.715
	{100}	33x33	16	1	3.547	3.859	2.302	2.736
	{110}	21x21	11	1	4.489	4.77	2.068	2.381
Ta	{111}	25x25	22	4	3.923	4.221	2.742	3.058
	{100}	39x39	15	1	3.83	4.121	2.49	2.881
	{110}	33x33	19	1	4.728	4.982	2.354	2.648
Cr (AF)	{111}	31x31	22	2	3.741		3.411	
	{100}	41x41	19	1	3.681		3.13	
	{110}	25x25	15	1	4.803		2.849	
Cr (NM)	{111}	31x31	22	2	4.09	4.392	3.57	4.082
	{100}	41x41	19	1	4.017	4.355	3.748	4.192
	{110}	25x25	15	1	4.824	5.127	3.313	3.76
Mo	{111}	27x27	22	4	4.03	4.343	2.998	3.443
	{100}	35x35	19	1	3.835	4.355	3.19	3.637
	{110}	41x41	15	1	4.519	4.862	2.772	3.117
W	{111}	21x21	21	4	4.134	4.414	3.555	3.958
	{100}	33x33	19	1	4.096	4.44	4.034	4.427
	{110}	31x31	15	1	4.777	5.05	3.282	3.655
Tc	{0001}	21x21	18	3	4.636	5.005	2.226	2.7143
	$\{10\bar{1}0\}$	29x17	20	2	4.472	4.81	2.543	3.041
	$\{12\bar{3}0\}$	13x13	15	2	4.239	4.56	2.662	3.199
	$\{12\bar{3}1\}$	21x21	20	5	4.082	4.42	2.852	3.419
Re	{0001}	17x17	15	3	4.907	5.227	2.639	3.089

		$\vec{k}$-mesh	Layers in slab	Free layers	$\Phi_{PBE}(eV)$	$\Phi_{LDA}(eV)$	$\gamma_{PBE}(\frac{J}{m^2})$	$\gamma_{LDA}(\frac{J}{m^2})$
	$\{10\bar{1}0\}$	29x17	12	2	4.68	4.986	2.913	3.381
	$\{12\bar{3}0\}$	9x9	11	2	4.492	4.769	3.111	3.613
Fe-α	{111}	31x31	22	3	3.862	4.541	2.712	3.472
	{100}	41x41	19	2	3.894	4.41	2.53	3.442
	{110}	47x47	12	0	4.743	5.275	2.455	3.173
Fe-γ	{111}	27x27	15	3	5.205	5.507	2.467	3.296
	{100}	25x25	13	3	4.739	5.18	1.906	3.84
	{110}	33x21	18	3	3.897	4.721	2.41	3.814
Ru	{0001}	21x21	18	3	4.993	5.372	2.675	3.239
	$\{10\bar{1}0\}$	29x17	20	2	4.784	5.148	2.986	3.584
	$\{12\bar{3}0\}$	13x13	15	2	4.43	4.78	3.405	4.076
	$\{12\bar{3}1\}$	21x21	20	5	4.383	4.739	3.328	4.003
Os	{0001}	21x21	18	3	5.302	5.638	2.997	3.494
	$\{10\bar{1}0\}$	29x17	20	2	5.062	5.386	3.403	3.956
	$\{12\bar{3}0\}$	13x13	15	2	4.782	5.071	4.091	4.719
Co	{0001}	21x21	18	3	4.925	5.386	2.128	2.768
	$\{10\bar{1}0\}$	29x17	20	2	4.703	5.136	2.267	2.954
	$\{12\bar{3}0\}$	13x13	15	2	4.389	4.806	2.461	3.253
	$\{12\bar{3}1\}$	21x21	20	5	4.328	4.764	2.622	3.408
Rh	{111}	25x25	14	3	5.138	5.536	2	2.558
	{100}	23x23	14	3	5.068	5.472	2.34	2.96
	{110}	27x17	14	3	4.583	4.961	2.388	3.045
Ir	{111}	25x25	15	3	5.514	5.86	2.297	2.817
	{100}	23x23	14	3	5.565	5.914	2.85	3.435
	{110}	27x17	19	3	4.97	5.314	2.881	3.512
Ni	{111}	29x29	11	3	5.02	5.497	1.916	2.506
	{100}	27x27	13	3	4.901	5.328	2.209	2.855
	{110}	33x21	15	3	4.488	4.949	2.262	2.945
Pd	{111}	25x25	14	3	5.244	5.651	0.253	0.402
	{100}	23x23	14	3	5.09	5.521	0.305	0.47
	{110}	27x17	16	3	4.834	5.216	0.322	0.483
Pt	{111}	25x25	15	3	5.691	6.046	1.434	1.984
	{100}	23x23	15	3	5.673	6.04	1.834	2.405
	{110}	27x17	20	3	5.281	5.633	1.858	2.465
Cu	{111}	25x25	13	3	4.749	5.17	1.271	1.761
	{100}	23x23	13	3	4.492	4.88	1.42	1.951
	{110}	27x17	22	3	4.369	4.751	1.508	2.054
Ag	{111}	25x25	14	3	4.345	4.843	0.717	1.145
	{100}	23x23	15	3	4.223	4.676	0.802	1.268
	{110}	27x17	19	3	4.113	4.552	0.858	1.352
Au	{111}	21x21	13	3	5.114	5.528	0.699	1.123
	{100}	19x19	13	3	5.082	5.46	0.857	1.334
	{110}	27x17	22	3	4.961	5.329	0.882	1.389
Zn	{0001}	21x21	18	3	4.075	4.442	0.308	0.506

		$\vec{k}$-mesh	Layers in slab	Free layers	$\Phi_{PBE}(eV)$	$\Phi_{LDA}(eV)$	$\gamma_{PBE}(\frac{J}{m^2})$	$\gamma_{LDA}(\frac{J}{m^2})$
	$\{10\bar{1}0\}$	29x17	20	2	4.334	4.702	0.747	1.102
	$\{12\bar{3}0\}$	13x13	15	2	4.026	4.299	0.965	1.389
	$\{12\bar{3}1\}$	21x21	20	5	4.126	4.432	0.943	1.356
Cd	{0001}	21x21	18	3	3.811	4.208	0.207	0.373
	$\{10\bar{1}0\}$	29x17	20	2	4.085	4.493	0.442	0.746
	$\{12\bar{3}0\}$	13x13	15	2	3.902	4.209	0.562	0.935
Al	{111}	35x35	19	3	4.047	4.216	0.816	0.972
	{100}	33x33	19	3	4.255	4.415	0.94	1.106
	{110}	39x25	21	3	4.045	4.207	0.998	1.173
Tl	{0001}	19x19	16	2	3.561	3.981	0.264	0.428
	$\{10\bar{1}0\}$	23x13	20	1	3.556	3.975	0.234	0.403
	$\{12\bar{3}0\}$	13x13	16	3	3.516	3.941	0.277	0.459
	$\{12\bar{3}1\}$	21x21	20	5	3.517	3.948	0.296	0.488
Graphite	{0001}	23x23	17	1	4.565	4.759	0.119	0.431
+D3	{0001}	23x24	17	1	4.459		0.163	
Diamond	{111}	9x17	14	3	4.357	4.541	4.05	4.501
	{100}	7x13	14	3	5.626	5.626	5.198	5.697
	{110}	11x11	12	3	5.299	5.563	5.437	5.903
Si	{111}	9x17	14	3	4.667	4.811	1.361	1.513
	{100}	7x13	14	3	4.563	4.712	1.406	1.572
	{110}	7x7	12	2	5.002	5.229	1.528	1.705
Ge	{111}	9x17	14	3	4.381	4.551	0.89	1.156
	{100}	7x13	14	3	4.482	4.722	1.003	1.269
	{110}	11x11	12	3	4.743	4.993	1.235	2.007
Sn-α	{111}	9x17	14	3	4.148	4.372	0.54	0.7
	{100}	7x13	14	3	4.231	4.494	0.628	0.804
	{110}	9x9	12	2	4.398	4.706	0.786	0.998
Sn-β	{001}	11x11	19	3	4.015	4.26	0.507	0.732
	{100}	7x13	16	1	3.954	4.199	0.369	0.576
	{101}	15x15	14	4	4.009	4.28	0.421	0.624
	{110}	11x15	16	2	4.217	4.493	0.478	0.705
Pb	{111}	21x21	22	3	3.763	4.08	0.253	0.402
	{100}	19x19	15	3	3.796	4.101	0.305	0.47
	{110}	25x25	15	3	3.727	4.029	0.322	0.483